UAS MULTISPECTRAL IMAGING FOR DETECTING PLANT STRESS DUE TO IRON CHLOROSIS IN GRAIN SORGHUM

A Thesis

by

ISABEL ANTOINETTE GARCIA

BS, New Mexico State University, 2015

Submitted in Partial Fulfillment of the Requirements for the Degree of

MASTER of SCIENCE

in

GEOSPATIAL SURVEYING ENGINEERING

Texas A&M University-Corpus Christi
Corpus Christi, Texas

August 2018

UAS MULTISPECTRAL IMAGING FOR DETECTING PLANT STRESS DUE TO IRON CHLOROSIS IN GRAIN SORGHUM

A Thesis

by

ISABEL ANTOINETTE GARCIA

This thesis meets the standards for scope and quality of

Texas A&M University-Corpus Christi and is hereby approved.

“Michael J. Starek, PhD”
Chair

“Michael J. Brewer, PhD”
Committee Member

“Gary Jeffres, PhD”
Committee Member

August 2018

ABSTRACT

This study uses a small Unmanned Aircraft System (sUAS) equipped with a multispectral sensor to assess various Vegetation Indices (VIs) for their potential to monitor iron chlorosis levels in a grain sorghum crop. Iron chlorosis is a nutritional disorder that affects numerous varieties of crops and plants that are grown on high-pH, calcareous soils and greatly affects crop yield. The objective of this project is to find the best Vegetation Index (VI) to detect and monitor iron chlorosis.

A series of flights were completed over the course of the growing season and processed using Structure-from-Motion (SfM) photogrammetry to create orthorectified, multispectral reflectance maps in the red, green, red-edge, and near-infrared wavelengths. A series of ground data collection methods were used to analyze stress and chlorophyll levels and grain yield, correlating them to sUAS-acquired four-band multispectral imagery covering the area of interest for ground control and precise crop examination.

25 Vegetation Indices (VIs) were calculated using the collected reflectance maps and soil-removed reflectance maps (a supervised classification was used to remove soil via a binary classification). The separability for each VI was then calculated using a two-class distance measure, determining which contained the largest separation between the pixels representing iron chlorosis and healthy vegetation. The field-acquired levels of iron chlorosis were used to conclude which VIs achieved the best results for the dataset as a whole and at each level of chlorosis (low, moderate and severe). It was concluded that the MERIS Terrestrial Chlorophyll (MTCI), Normalized Difference Red Edge (NDRE), and Normalized Green (NG) indices achieved the highest amount of separation between the iron chlorotic and healthy plant populations, with the

NG being the most popular for both soil-included and soil-removed VIs, with soil-removed VIs reaching higher levels of separability.

DEDICATION

“Learning is the only thing the mind never exhausts, never fears, and never regrets”

-Albert Einstein

ACKNOWLEDGEMENTS

First, I would like to thank my advisor, Dr. Starek for being patient and having confidence in me throughout this journey. This has been a learning process and I have learned everything from researching efficiently, giving professional presentations, to writing, working with data, and how to independently teach myself. I would also like to thank my committee members for their willingness to serve me and help complete this study. Also, to Dr. Brewer, specifically who helped me invent a replacement thesis topic when the first didn’t pull through.

I would also like to thank the hard workers at AgriLife who welcomed me to their community. You all taught me about grain sorghum, helped me collect data in the field, and gave me a pleasant experience in the agricultural fields.

Thirdly, I would like to thank the students in MANTIS. Many of you taught me how to use ArcMap, its tools, and gave me helpful tips and general encouragement throughout the entirety of earning this degree.

To my family and friends, thank you for giving me an endless amount of support. It is because of your love and encouragement that I am here. Thank you for listening to my frustrations, and for patiently sitting through hours of FaceTime when I needed someone to be my practice audience before presentations.

I would like to give a big thank you to the USDA/NIFA HSI (Award Number: 2016-38422-25543, Project Name “Experimental training of use of Unmanned Aerial Systems (UAS) technology for agricultural applications”) for funding this project and encouraging minorities to pursue higher education. Without you, this study would not have taken place and I would not have discovered my appreciation for precision agriculture.

TABLE OF CONTENTS

CONTENTS PAGE

LIST OF FIGURES

FIGURES PAGE

LIST OF TABLES

CHAPTER I

1.1 Introduction

There are over 7 billion people in this world, and with a global population projected only to increase, cultivated lands are shrinking while urban areas are rapidly expanding. As a result, it is vital for food producers to maximize their crop yields. In order for this to happen, a system must be constructed to manage each of these fields according to their individual needs (Seelan, et al. 2003). Consequentially, farming has become a form of science, utilizing technology to its advantage to increase both productivity and profitability by improving growth (Mulla 2013), decreasing wastefulness concerning pesticides and plant nutritional sprays, and therefore improving the environment. This method of crop production, called precision agriculture, considers soil types, crop types, spatial variability of the plants, weeds, pests, and many other conditions in order to determine the most effective processes to achieve the best product (Vega, et al. 2015). It is important, throughout the crops growing season, to closely monitor the plants growth, health, and development, especially because growing time is limited (Duan, et al. 2017). This, in many cases, requires information about crop conditions to be collected frequently and at regular intervals throughout the growing season, at high resolution. Often, easily accessible data is collected at lower resolution, and irregularly which causes problems. Therefore, these methods need to be cost efficient in order for these farmers to have the ability to pay for quality services and still maximize profits (Seelan, et al. 2003).

Precision agriculture allows the integration of modern technologies to monitor and remotely manage crops. Monitoring crops can be done using remote sensing methods and can include satellite-based data, unmanned aircraft systems (UASs), global navigation satellite systems (GNSS), and light detection and ranging (LIDAR). Additional recording and analyzation can be completed with geographic information systems (GIS), plant sensors, yield monitoring instruments, and pest sensors (Seelan, et al. 2003). The acquisition of crop data via aerial instruments has been traditionally completed with satellite imagery and imagery collected from manned aircrafts. However, it has been found that remotely sensed images from these platforms are generally low-resolution, and have a long delivery time of their products (Herwitz, et al. 2004).They are also extremely expensive, are difficult to plan for data acquisition and in some cases are impossible for farmers to acquire (Jannoura, et al. 2014). This is why, in recent years, UASs have become a popular platform for obtaining remotely sensed data. Small UASs (sUAS) and micro-UASs equipped with digital imaging sensors have become a widespread method for monitoring crop development for precision agriculture because of their many positive attributes. These systems are manageable (according to the FAA a sUAS is under 55 lbs), cost-efficient, fly at low altitudes allowing high resolution to hyperspatial resolution (cm to sub-cm scale) imagery to be acquired, are flexible in terms of scheduling flight dates, and can be flown with any necessary regularity (Vega, et al. 2015).

UASs, for many years, were only used for military purposes and it was not until this decade that they became readily available for commercial use (Gago, et al. 2015). Similarly, only recently have these systems have become popular for use in precision agriculture due to their flexibility, high-resolution imagery, and small, lightweight sensors (Baluja, et al. 2012). In the early 2000's only a handful of field experiments were completed to test the quality and the capabilities of UAS derived data. One of the first and most impactful experiments was completed by NASA in 2002 (Herwitz, et al. 2004). The project location for this experiment was in Kauai, Hawaii over one of the largest coffee plantations in the nation. Coffee growth is sporadic, making this crop ideal for experimentation. The unmanned aerial vehicle (UAV) that was used in this experiment contained a wingspan of 36.3 meters and held a multispectral camera and a color camera. The results of this experiment brought the authors to conclude that UAVs equipped with digital and multispectral cameras are a good alternative to imagery acquired from traditional platforms (such as satellites and aircraft) (Herwitz, et al. 2004). This led to further UAS precision agriculture experimentation and also to the development of accuracy standards for these new and innovative remote sensing platforms.

The first experiments completed with UASs eventually led to many projects being completed with imaging via sUAS. Vega, et al. (2015) used a sUAS to acquire multispectral imagery for monitoring of a sunflower crop in Cordoba, Spain. Using the green (G), red (R), and near infrared (NIR) bands the normalised difference vegetation index (NDVI) was calculated and was used to successfully detect differences in plant yield and nitrogen content. Rasmussen, et al. 2015 conducted an experiment using two types of sUAS, a fixed wing and a rotary wing, each mounted with a different consumer-grade sensor (one multispectral, one red, green, blue (RGB), respectively). The findings of this study showed that sUAS-acquired imaging had the same capability as ground-based methods to monitor crop changes and responses to biotic and abiotic factors. Jannoura, et al. 2014 used an sUAS (hexacoptor) to collect RGB imagery to prove that true colour images could be used to calculate VIs to monitor crops. Lastly, Stanton, et al. (2017) used a fixed-wing sUAS to collect multispectral imagery to estimate the amount of damage on a sorghum crop caused by the invasive sugar cane aphid. The NDVI was used to detect plant stress due to aphid feeding injury to the foliage.

sUASs for precision agriculture has many usages. A wide variety of remotely sensed data can be collected and these data can help plan irrigation, water management, detect insect infestation problems and weed infiltration, and determine plant stress by carrying out small scale photogrammetric surveys using RGB and/or 4-band multispectral imaging (Whitehead, et al. 2015). Traditionally, surveys by means of photogrammetry are completed using large, metric cameras flown at a high altitude on a manned aircraft. Careful planning must be completed before the flight is conducted to ensure adequate side-lap and end-lap of every photograph. The imagery then undergoes a succession of corrections and transformations based on the orientation in the x-, y-, and z-directions of both the platform and of the camera at each instance that a photograph was taken, and the positional information, x, y, and z global coordinates (most platforms contain a GNSS receiver onboard for direct georeferencing) (Xiang, et al. 2011). After the images are collected key points from the overlapping images are identified and a least-squares bundle block adjustment is computed to reconstruct the camera position and orientation at each instance every photograph was taken. At this point the ground control points (GCPs) (which are established before the survey) are applied at this point for positional purposes. Then, matching points are validated and unknown parameters are calculated to densify the point cloud. The images are rectified, leading to the interpolation of a Digital Surface Model (DSM) and/or an image orthomosaic (Toutin, et al. 2004; Stanton, et al. 2017). Sugiura et.al. (2005) completed a project in 2004 testing a UASs ability to create a small-scale photogrammetric orthomosaic. Although the data was collected using a sUAS, all of the imagery was corrected using traditional photogrammetric reconstruction methods (Sugiura, Noguchi and Kazunobu 2005). Since then a new form of image processing has been introduced: Structure-from-Motion (SfM) photogrammetry coupled with dense matching using multi-view stereo (MVS) algorithms (Whitehead, et al. 2015). SfM/MVS photogrammetry (simply called SfM here) enables overlapping image sequences to be processed into dense three-dimensional (3D) point cloud data, which are then converted into reflectance maps.

SfM photogrammetry has replaced traditional photogrammetric methods in terms of processing UAS-acquired imagery because of its automation, efficiency, and ability to generate 3D point cloud data from consumer-grade, non-metric cameras typically equipped to sUAS (Stanton, et al. 2017). This method also has the ability to automatically calibrate camera internals and simultaneously solve for camera position and orientation (pose) at each image capture. This allows less user involvement, the extraction of more points, and increasing accuracy (Bakker and Lane 2017). This is possible due to an automatic feature-matching algorithm that is embedded in SfM software. Identification of key points and features allows the software to solve the camera location and position at the time each photograph was taken (Westoby, et al. 2012). One key difference between SfM and traditional photogrammetry is the use of GCPs. With traditional photogrammetry, a series of GCPs serve as tie points and are essential to stitch together adjacent imagery after necessary corrections are completed. SfM does not need GCPs to create an orthomosaic and instead uses a mass bundle adjustment that uses every recognized point that is redundantly captured from image-to-image (Snavely, et al. 2008). Therefore, GCPs are only optional when conducting SfM photogrammetry. However, just because they are optional does not mean that they are not useful. GCPs can serve as helpful reference points and are often necessary for high accuracy georeferencing of UAS-SfM derived data products (Bakker, et al. 2017; Stanton, et al. 2017).

Accurately georeferenced 3D point cloud data output from SfM photogrammetry can be used for a variety of precise mapping applications including the generation of digital surface models (DSMs) for topographic modeling, measuring canopy height, and deriving orthomosaics for plainmetric mapping (Westoby, et al. 2012). Because of its wide array of uses, UAS-SfM derived data is becoming more widely adopted into the professional surveying, engineering, and GIS world.

The number of UAS studies in literature aimed at detecting and monitoring plant stress has been increasingly growing in recent years (Gago, et al. 2015; Stanton, et al. 2017; Duan, et al. 2017). Various SfM photogrammetry trials on crops have been conducted using both RGB true color digital cameras and multispectral digital sensors that measure both visible and near-infrared wavelength bands of reflected sunlight energy (Mulla, et al. 2013; Vega, et al. 2015; Rasmussen, et al. 2015; Jannoura, et al. 2014). True color and color-infrared bands collected from digital imaging sensors are ideal for producing measurable information about plant status with spatial changeability (Jannoura, et al. 2014).

Plant health is detectable by airborne sensors because of the plant's reflectivity and absorption of electro-magnetic (EM) radiation. The pigmentation of the plants controls this reflectivity and absorption, creating incident radiation depending on the plant size, orientation, and color. Plant pigment heavily relies on the amount of chlorophyll, which intensely absorbs radiation within the visible spectrum (Mulla 2013). When a plant is stressed chlorophyll production declines, increasing the reflectance of wavelengths in the visible spectrum, including those in the red bands (Alves, Macrae and Koch 2015).

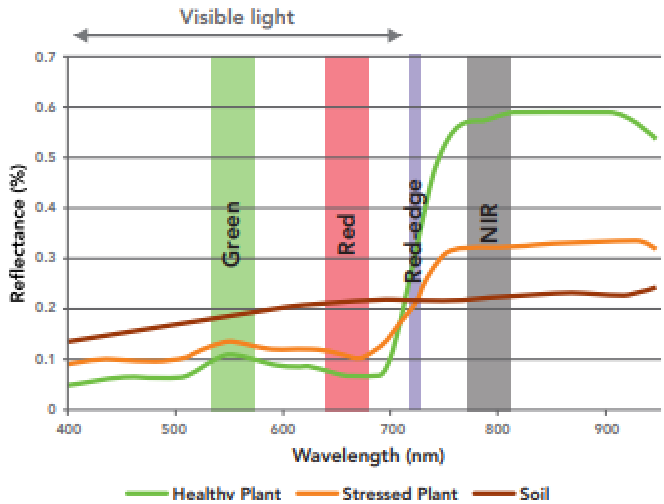

Figure 1: Reflectance of green vegetation in visible to near-infrared portion of the EM spectrum (Sequoia Data Sheet 2017; Mutanga, et al. 2004; Ramoelo, et al. 2012).

Plant health and heterogeneity can be quantitatively and qualitatively measured by means of calculating a series of remotely sensed vegetation indices (VIs), a common way of extracting crop information from multispectral digital imagery. This is completed through a series of image band calculations (Rasmussen, et al. 2015). The most common calculation performed is related to crop status such as leaf area index (LAI), canopy cover, biomass, and chlorophyll content in cereals (Hansen, et al. 2003) and determines vegetation wellbeing, or 'greenness'. This index is called the normalized difference vegetation index (NDVI) (Mulla 2013), and is calculated using the sensor's red band (R), which registers the absorption of red wavelengths due to chlorophyll concentration (Sripada, et al. 2008). Lower brightness values in the R channel implies higher absorption from the plant implying that chlorophyll content is also higher. The sensor's near-infrared (NIR) band registers the reflection of scattering NIR wavelengths by the plants and other captured land features (Mutanga, et al. 2004). The NIR channel can be useful in determining plant stress due to a higher reflection in plants containing more chlorophyll and vice versa (Sripada, et al. 2008; Mutanga, et al. 2004). The reflectance of visible light essentially relies on the amount of chlorophyll that is contained in the leaves of a plant. This is why visible light reflects differently on a green leaf versus a yellow leaf, although the NIR wavelengths could stay the same for both (Rasmussen, et al. 2015) as shown in Figure 1. The NDVI ratio is computed using the following formula:

$$\mathrm{NDVI} = \frac{\mathrm{NIR-R}}{\mathrm{NIR+R}} \quad (1)$$

where R and NIR are either the digital number (DN) values for pixels from the red and near-infrared bands of a multispectral imaging sensor (Vega, et al. 2015) or the reflectance values, which are normalized values to which a series of corrections are applied (such as target reflectance, sun zenith angle, atmospheric conditions) to produce a more realistic value (Guyot, et al. 1994). The result of this equation is a number ranging between -1.0 and 1.0,with values closer to -1.0 representing features such as soil, dirt, rocks, or vegetation that is essentially dead or dying and values closer to 1.0 suggest more green, healthy vegetation among other things (Sabins, et al. 2007). Jannoura, et al. 2014 gives a good example of how true color photographs can be used to determine and monitor plant status as well. Within their study, the normalized green-red difference index (NGRDI) is calculated using the green (G) and red (R) image bands via the following formula:

$$\mathrm{NRGDI} = \frac{\mathrm{G-R}}{\mathrm{G+R}} \quad (2)$$

with G and R representing the digital values of each bands' respective pixels. This equation accounts for the absorption of red wavelengths and the reflectance of green wavelengths by a plant that contains high amounts of chlorophyll and vice versa. The result, much like the NDVI, is a number between -1.0 and 1.0, with values near -1.0 suggesting a soil, dirt, and unhealthy vegetation and values near 1.0 suggesting healthy vegetation. The results from this study showed that NRGDI is a good alternative method when only RGB imagery is available and suggests that RGB imagery can certainly work in a less detailed project or as a data check when both RGB and NIR bands are collected.

Furthermore, the red-edge (RE) band provides useful information about vegetation. This very narrow band captures the edge of reflectance at the area of change between spectral absorption in the R and scattering in the NIR region Figure 1 (Mutanga, et al. 2004, Ramoelo, et al. 2012). VIs computed using the RE band (called narrow band indices) are said to have improved estimates of chlorophyll concentrations compared to traditional broad-band indices (such as indices using NIR) (Ramoelo, et al. 2012) due to their short spectrum range. This band has the ability to replace NIR in common VIs such as the NDVI to create the NDVI RE equation, stated as follows:

$$\text{NDVI RE} = \frac{\text{RE} - \text{R}}{\text{RE} + \text{R}} \quad (3)$$

This provides more acute information concerning plant health because of the usage of a narrow band. Broad bands, on the other hand, provide information from a wider range of spectrums, resulting in a loss of critical plant health information due to the averaging of spectral data (Hansen, et al. 2003).

Stress in crops can be due to a wide variety of problems. For example, if plants are not receiving enough water or too much water, it will result in the yellowing of their leaves. A major nutritional problem in numerous crops is the lack of iron due to crops planted in calcareous and sandy soils located mostly in arid and semi-arid climates (Prasad 2003). This iron deficiency, or iron chlorosis, greatly affects the growth, yield, and lifespan of any plant that is chlorotic (Abadia, et al. 2011). It is important that this problem is caught early in the growing season to sufficiently treat the affected plants. This is done by providing nutritional supplements to the chlorotic plants, either to the soil or directly to the leaves, early in the growing season. If the plants are not sufficiently treated, the plants will be underdeveloped and little to no yield will be produced (pictured in Figure 2) (Karagiannidis, et al. 2008). Iron chlorosis affects a multitude of crops including grape plantations (vineyards), fruit trees, peanuts, sorghum, and various types of vegetables. Some crops however, are tolerant to this nutritional disease. These crops include maize (corn), alfalfa, cotton, oats, rice, and barley (Behboudian, et al. 2003). Some particular plant species and genotypes have varied abilities to absorb iron from even calcareous and high-pH soils. These iron chlorosis tolerant plants contain proteins that are produced when soil iron levels are low, providing them the nutrition that they need. Other crop varieties do not have this special ability in iron-deprived soils, leading them to nutrient deprivation (Prasad 2003). The lack of iron in these crops reduces the appropriate amount of energy needed for proper growth, therefore decreasing the production of chlorophyll in the plants (Karagiannidis, et al. 2008). This then leads to the slowing of cell division within the foliage, making new leaves appear small and sickly (Behboudian, et al. 2003). As a result, the bottom leaves of the plant to look healthier and, as the plant grows, it will become additionally nutrient deprived. This will cause the plant to gradually yellow towards the top, appearing at different levels of severity. This is one visual symptom of an iron deficiency of the plant and is a good indicator of iron chlorosis. New leaves will typically contain dark green veins that are clearly presented against the yellowing leaf, unless the plant is

Figure 2: An underdeveloped grain sorghum plant with severe iron chlorosis (Trostle 2013).

so nutrient deprived that the leaves are a light yellow and dry, containing little to no chlorophyll (Prasad 2003).

As mentioned above, sorghum is listed as a crop that is susceptible to iron chlorosis, meaning that in many cases, individual plants or groups of plants must be treated. According to Prasad et.al. 2003, iron deficiency in sorghum crops could mean that 25% or more of the total yield could be lost due to underproduction of plant leaves, stems and roots. The iron deficiency causes uneven flowering, delays for readiness during harvest time, uneven pollination, and effects midge spraying. This is all made even more difficult because iron chlorosis does not have a pattern within a crop. Rather, it occurs in random places, where either a plant or groups of plants cannot get enough iron nutrition and may be more effective on some sorghum hybrids and less effective on others (Prasad 2003).

There are three levels of visual iron chlorosis as listed by Livingston, et.al. 1992. The first of these, stated as 'mild chlorosis' does not affect the plants' yield and causes delayed flowering by only two to three days. The leaves, instead of being a uniform green, are slightly striped with a yellowish-green and green hue, as displayed in Figure 4. The second state of chlorosis, or 'moderate chlorosis', contains yellow and green striped leaves. The chlorotic plants are scattered throughout the crop and the plants will yield less grain and irregular midge control will commence if treatment is not provided early enough in the growing season. The worst level of damage, 'severe chlorosis', is almost untreatable by the time it is detected. The leaves of the plants affected appear yellow-white in color, are thin, and the stems of the plant are fragile. These plants will not grow to a great height, and will probably not flower or provide grain. If they are treated early enough they can survive, but they will flower late and are more susceptible to midge damage (Livingston, et al. 1992). The level of chlorosis occurring in a plant could also appear to be 'in-between' these stated ranks, as will be found in this study. Figure 3 displays a leaf with moderate to severe levels of iron chlorosis because of the low amounts of chlorophyll, yet slightly detectable green veins.

Figure 3: An example of moderate/severe iron chlorosis (McClure n.d.)

Figure 4: An example of mild iron chlorosis (Scanlan 2015)

In addition to direct effects on the plants productivity, it is important that sorghum crops grow uniformly and all flowers at the same time for several management reasons. If flowers are delayed and miss pesticide spraying, they will most likely be affected by sorghum midge. The sorghum midge is a widespread damaging insect on sorghum crops in the state of Texas. One full generation lives from 14 to 16 days, and as the plants grow, the number of these pests rapidly increases. Once the sorghum has come to flower, the damage intensifies as the larva feeds on what will develop to be the grain kernel (Cronholm, et al. 2007). To prevent this pest from desolating the grain produced by sorghum crops, the plants must be treated regularly, meaning it is essential for them to grow homogeneously. To do this, the problem of iron chlorosis must first be identified and then treated.

Iron chlorosis is a major nutritional ailment that effects many types of crops, no it is important to develop a quick and effective way to identify affected plants early (Abadia, et al.

2011). Iron deficiencies are mostly detected visually, by noticing veining in the leaves, by sampling the plants' roots, and by testing the plants' leaves (Abadia, et al. 2011). The methods that are most commonly used to detect and measure the disorder however, are "completely visual and labor intensive" (Naik, et al. 2017). It is therefore important for a method to be developed to not only reduce labor, but also provide more accurate and quantitative data. Although there is plently of general information about iron chlorosis in grain sorghum (Abadia, et al. 2011; Behboudian, Pickering and Dayan 2003; Livingston, Coffman and Unruh 1992) no studies could be found that utilzies sUAS to detect iron chlorosis. However, some studies have focused on finding the disorder in other crops.

sUAS's are now popular for crop monitoring and precision agriculture, but not many studies have explored their usage on iron chlorosis in crops, especially where grain sorghum is concerned. Naik, et al. (2017) used an unmounted RGB digital camera to classify different levels of stress due to iron chlorosis in a soybean crop through heirarchical classification models. Meggio, et al. 2010 used hyperspectral imagery via manned aerial vehicle to calculate a series of VIs for detecting iron chlorosis in a yineyard. It was concluded that this type of imagery is useful in determining plants with iron chlorosis. As stated above, this disorder is popular in many types of plants and is causing farmers a loss of yield. Finding the best way to idenify the problem will benefit farmers and consumers alike.

1.2 Study Purpose and Objectives

The purpose of this study is to use a small UAS equipped with a four-band digital imaging sensor to survey and assess a small plot sorghum field to discover and monitor areas of plant stress due to iron chlorosis. The plants with iron chlorosis will be further assessed into different levels of chlorosis (mild, moderate and severe) to understand the spectral differences between them.

Using the ground collected data, correlations to the multispectral imagery will be made and used as field control to locate specific areas of iron chlorosis and its level and correlate yield data. A series of 25 vegetation indices will be calculated to assess the health of the crops and the separability of each VI will be computed to determine which best separates plants with iron chlorosis and healthy vegetation.

This study lays out the following objectives:

- Use sUAS-acquired multispectral data to derive 25 VIs for determining which is the most effective in defining iron chlorosis.
- Successfully remove background noise from the multispectral data for more precise derivation of VIs
- Calculate the separability of each VI to identify which perform best in separating pixels representing iron chlorosis, levels of chlorosis, and healthy vegetation.
- Determine if extracting canopy from the multispectral data was useful and provided better results and/or higher separability measures

CHAPTER II: STUDY AREA AND DATA SETS

2.1 Project Location

The field site was at Texas A&M AgriLife Research Center located in Corpus Christi, Texas (see Figures 5 and 6) and all data were collected during the 2017 agricultural growing season. The center contains many cultivated fields, planted with a variety of crops, which host numerous research experiments. The field used for this experiment contained 80 four-row plots planted with various sorghum hybrid plants. A total of 10 hybrids were planted, making a total of 8 plots of each planted hybrid. One-half of each hybrid type was also treated with insecticide, meaning 4 plots of each hybrid were treated, leaving the other 4 untreated.

Figure 5: Location of AgriLife Research and Extension Center, Corpus Christi, TX.

Figure 6: Location of sorghum study plot at AgriLife.

2.2 UAS Data Collection

A sUAS was flown over Texas A&M AgriLife's agricultural fields, including the sorghum field of this study, over the course of the 2017 growing season. The flights were performed once a week over the course of 12 weeks, making a total of 12 flights. The UAS used in this study was a small, fixed-wing drone called an eBee SQ (senseFly, Cheseaux-sur-Lusanne, Switzerland), pictured in Figure 7. This sUAS is about 0.71 kg (1.56 lbs), contains a wingspan of 96 cm, has an average flight time of 45 minutes, can cover 10 km^2 (3.9 mi^2) with one battery charge (senseFly Ltd 2014).

The eBee also comes equipped with a Parrot Sequoia multispectral sensor (Parrot, Paris, France), pictured in Figure 8. According to senseFly Ltd 2018 the sensor is the "smallest, lightest multispectral sensor ever released," weighing only 72 g (2.5 oz), a height of 59 mm, width of 41 mm and thickness of 29.5 mm. It also contains four 1.2 MP monochrome sensors with focal lengths of 3.95 mm (used to collect red, red-edge, green, and near-infrared wavelengths) and a 16 MP RGB sensor with a focal length of 4.88 mm (Sequoia Frequently Asked Questions n.d.; senseFly Ltd 2014). The four monochrome collect data in the green, red, red-edge, and near-infrared bandsat the central frequency of each wavelength (See Table 1 for details). The ground sample distance (GSD) per pixel of the Sequoia is 11 cm/pixel at 120m (400 ft) above ground and can get down to 2 cm (0.8 in) (Sequoia Frequently Asked Questions n.d.; senseFly Ltd 2014).

Table 1: A display of channels the Parrot Sequoia sensor records. The Recorded Frequency is the frequency recorded in each channel, which is the center of each channel.

Band	Band Widths (nm)	Recorded Frequency (nm)
Green	530-570	550
Red	640-680	660
Red-Edge	730-740	735
Near-Infrared	770-810	790

A sunshine sensor is also included along with the multispectral sensor weighing 35 g and having height, width, and depth dimensions of 47 mm, 39.6 mm and 18.5 mm, respectively. This sensor is used to radiometrically calibrate the images based on that days' sunlight (the sensor faces upwards, towards the sun) to produce radiometrically correct reflectance maps. It is also equipped with a GPS/GNSS module and an intertial measurement componant for use to loosly track the location of the UAS at each location of each image capture. (Parrot Drones SAS 2018)

A preprogramming software is included with the packaging to help preplan flights, select up to 50 waypoints (georeferenced points) for navigation and use with the GNSS for image geotagging, and set flight actions (such as take-off, turns, overlap, sidelap, landing, etc.). Since the eBee is equipped with navigation, the use of GCPs is not needed. However, the accuracy without GCPs is 1 to 5 m horizontally and 2 to 5 m vertically. With GCPs the accuracy gets down to 4 cm horizontally and 7 m vertically due to the inaccuracy of the single-frequency, non-differential GNSS receiver on board the UAS. (senseFly Ltd 2014)

Flight data was collected once a week with the eBee SQ for 12 weeks throughout the duration of the growing season over the entire AgriLife planting area. The drone was flown, on average, at 210 feet above the ground and the imagery contained 80% sidelap and 60% endlap (Flight details are included in Table 2). These images were later cropped for better analysis of the small sorghum plot (see imagery in Appendix A).

Figure 8: An image of the eBee SQ agriculture, fixed-wing platform (senseFly Ltd 2018) used to capture data about the agricultural fields in this study.

Figure 7: An image of the Parrot Sequoia 4-band multispectral sensor. The Sequoia has four 1.2 MP monochrome sensors, capturing in the red, green, red-edge, and near-infrared spectral bands, as well as a 16 MP RGB camera (senseFly Ltd 2018).

Table 2: This table includes information about data collection, including flight dates, the ground sample distance (GSD) of each flight, and what field collection was completed on which date.

Date	**sUAS**	**GSD (cm/pxl)**	**Field Data Collection**
05/05/17	eBee SQ	7.85	-
05/12/17	eBee SQ	7.38	-
05/17/17	eBee SQ	7.38	-
05/2317	eBee SQ	7.41	-
05/31/17	eBee SQ	7.57	-
06/08/17	eBee SQ	7.13	-
06/13/17	eBee SQ	6.83	-
06/22/17	eBee SQ	6.78	Flagged areas of chlorosis
06/23/17	None	None	GPS and chlorosis ‘Level’
06/28/17	eBee SQ	6.83	SPAD measurements
07/06/17	eBee SQ	6.52	-
07/15/17	eBee SQ	6.98	-
7/19/17	None	None	Collected yield samples and put to dry
07/27/17	eBee SQ	6.67	Thrashed and weighed grain

2.2.1 UAS Accessories

A series of GCPs were laid out over the entire field area for high accuracy georeferencing of the UAS imagery and to ensure the "ground truth" field data on chlorosis levels and yield co-align accurately to the UAS imagery. The GCPs consisted of 1.5 ft by 1.5 ft cement targets painted black and white. The pattern painted on the targets is displayed in Figure 9 with a 6" gap between black triangles, and a 2.5" diameter center circle. After the targets were set they were georeferenced to get an accurate result. A total of 26 GCPs were laid out over the entire AgriLife field (Figure 11 shows an example for flight date of May 5, 2017), 5 of which were over the sorghum plot alone, displayed in Figure 10 (the field in which this study is located). They served as known, stable points that aided when the stitching process began. Without these points, the positional accuracy of the derived UAS image products would be roughly geotagged at 1 to 5 meters or even worse. Constraining the SfM aerotriangulation using geodetically surveyed GCPs during the SfM processing allows high accuracy of the created geospatial data products for further GIS analysis.

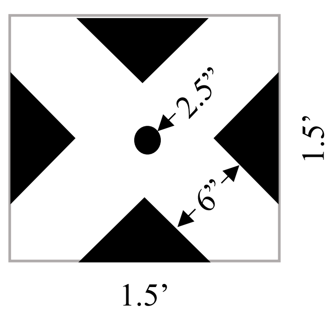

Figure 9: An example of what the GCP targets looked like. Each target was a 1.5' by 1.5' cement block, painted with a black and white pattern, with a 2.5" black dot in the center, used for georeferencing.

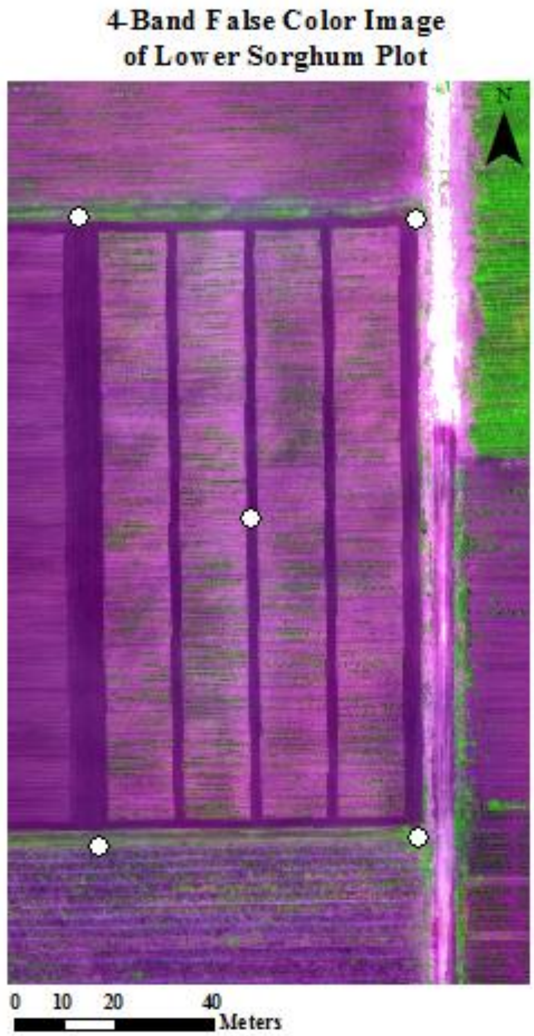

Figure 10: A display of the lower sorghum plot on a 4-band false color reflectance map. The GCP target locations are displayed as white dots, which represent the location of the targets.

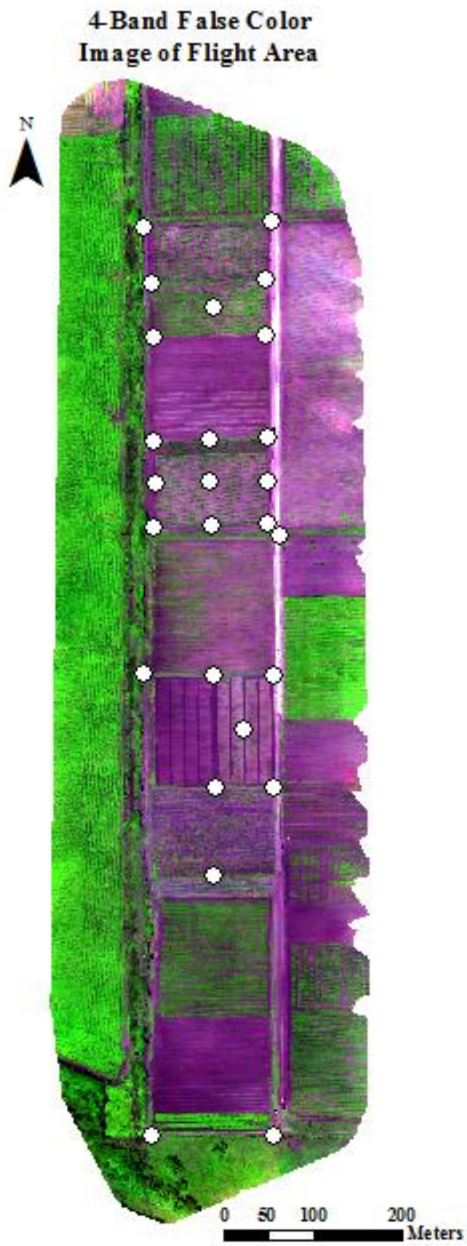

Figure 11: A display of the location of the GCPs laid out for flights over a 4-band false color reflectance map of data collected on May 5, 2017. The targets are represented by white dots, which are displayed large for visualization.

Immediately before or after a flight was completed, a radiometric calibration target was used to calibrate and correct the reflectance on the images. On any given day, lighting, the direction of the sun, position of the sensor, cloud coverage, and other factors will affect the imagery that is taken. These targets contain a white balance card that gives the reflectance properties of the bands registered by the sensor (in this case the bands are G, R, RE, and NIR) (MicaSense 2017). These 'reflectance properties' are used to convert the imagery to true reflectance values of a surface in the SfM photogrammetry process. Collecting the data for radiometric calibration involves taking a series of images of the calibration target (white balance card) and they are applied in the processing of the imagery. The software provided with the sUAS can automatically detect the calibration imagery or it can be input manually by the user (Pix4D Support 2011-2018).

2.3 Field Data Collection

During the course of this study, ground truth data were collected for the purpose of data redundancy and data correlation with iron chlorosis. This was completed through means of plant observations and consisted of data that was physically analyzed and associated with iron chlorosis. Physical analysis involved observing the plants and assessing the percentage of iron deficiency (measured by yellowness), using a SPAD chlorophyll meter (SPAD-502 DL Plus, Konica Minolta Sensing Inc., Osaka, Japan), and measuring grain yield. The dates each type of collection occurred are listed in Table 2.

Before any of these data were collected, the areas that were to be analyzed were marked with flags and georeferenced to locate individual and groups of plants on the remotely sensed imagery. Areas of iron chlorotic plants within the rows were chosen at random and marked with flags at two plants signifying endpoints and a midpoint plant. These lines of sorghum foliage were then georeferenced using an Altus GNSS receiver connected to a networked real time kinematic (RTK) network using virtual reference stations (VRS) broadcast corrections, at 5 second epochs which provide horizontal accuracy estimations of 45 mm (Cannon 2016). The program on the data collector that connects to the GPS unit contains a draw function that has the ability to draw lines and polygons ‘on the fly.’ This shortcut was used to draw short lines of plants and also included the endpoint and midpoint plants (stored as points) within those lines.

The iron chlorotic plants, or ‘yellow’ plants, were compaired to common, healthy plants (no visual signs of chlorosis), for color and reflectance comparison. Sections of healthy “green” plants were selected at random in locations near every georeferenced area of iron chlorosis for the comparison. These too were flagged and georeferenced to ensure that that there is a ‘greenness’ regulator to observe through the UAS imagery data.

2.3.1 Level of Chlorosis

Yellowness was observed and marked for each designated area on a high, medium, and low scale based on plant health. This scale reflects the different states of chlorosis that are visually variant on a plant. Healthy, normal plants with zero stress are used as control and are marked with ‘no chlorosis.’ ‘Mild chlorosis’ is visually observed on plants as mild striping of the leaves, ‘moderate chlorosis’ is a display of clearly green-and-yellow striped leaves, and ‘severe chlorosis’ is seen evidently with yellow or even yellow-white leaves. (Livingston, Coffman and Unruh 1992; Prasad 2003).

A total of 13 segments of healthy vegetation were georeferenced. The areas of iron chlorosis are made up of 5 segments of severe chlorosis, 6 segments of moderate chlorosis, and 4 segments of mild chlorosis, making a total of 15 segments. The locations of these areas are shown in Figure 12, where each color represents a different level of iron chlorosis, and healthy vegetation (the imagery used is a 4-band reflectance map of the field for the flight date closest to the chlorosis data collection).

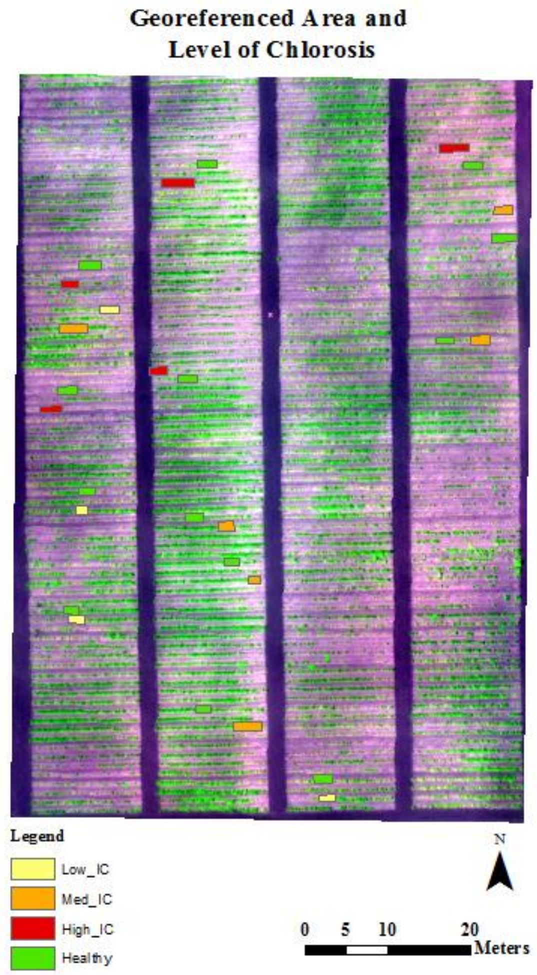

Figure 12: Areas of georeferenced plants overlaid in a 4-band false image color reflectance map. Segments of low, moderate and severe iron chlorosis are marked as low, med, high, respectively and areas of healthy plants are marked healthy.

2.3.2 SPAD Chlorophyll Meter

The relative levels of chlorophyll within a plants' tissues can be indicated using a chlorophyll meter (Alves, Macrae and Koch 2015). A (soil plant analysis development) SPAD-502 Plus chlorophyll meter (Mulla 2013; Konica Minolta 2008) was used to estimate the chlorophyll content of the marked plants. This device encompasses two windows with built-in LED lights that emit light in the red and near-infrared regions at 650 nm and 940 nm, respectively, when the measuring head is closed (Xiong, et al. 2015). When the measurements are taken, light from the emitting window is shown through the leaf and is passed to the receiving window. The receiving window contains a receptor that reads wavelengths that respond to different chlorophyll contents. This receptor then converts the amount of energy collected into a number that is displayed on the meter screen with a scale that ranges from 0 to 99.9 (Konica Minolta 2008). Both the bottom and the top leaves of the healthy and iron chlorotic sampled plants were estimated with the meter.

2.3.3 Yield Data

At the end of the growing season, right before the harvest date on July 19, 2017, yield samples of the georeferenced areas of both healthy and iron chlorotic plants were gathered. This was completed by clipping the grain head from the top of the sorghum plant, placing it in paper bags, and drying it. Then, the grain was extracted from the seed head and measured by weight (in grams) for analysis. This process was finished for each section of iron chlorotic and healthy plants. Each individual section consisted of one sampled georeferenced plant and ten random sampled plants. The grain from the ten sampled plants was used to correlate to the final VI values. The single grain head was kept separate from the rest of the row’s ten grain heads and was used to determine the amount of midge damage in the area. The plants were then dehydrated in a plant dryer, made special for dying plant samples before thrashing. The grain was thrashed using a special machine used to extract grain from sorghum. The machine consists of a feeding tube, a rotating blade, a ‘trash’ bag and a collecting tray. The sorghum was fed in through the feeding tube, where it then made contact with the rotating blade. The blade forced the seed out of the sorghum head, where it was then dropped in to the collecting tray. Any excess debris was blown into in ‘trash’ bag. The seed that fell into the collecting tray was then measured by weight in grams for yield information.

CHAPTER III: METHODOLOGY

3.1 UAS Image Processing

After the raw image data is collected from a flight, it must be post-processed to create georeferenced and radiometrically corrected reflectance maps. The imagery for this project was processed using SfM photogrammetry, which uses like-features from overlapping images to extract a series of 3-D points. Unlike traditional photogrammetry, the camera position and orientation (camera geometry) at the moment each image was taken is automatically solved without additional user information through matching attributes in multiple images (Westoby, et al. 2012). There are many open-sourced SfM photogrammetry processing solutions that are user friendly, accurate, and ideal for mapping data from UASs. Pix4Dmapper Pro (Pix4D SA, Lausanne, Switzerland) was used to process that data that was collected via sUAS for this study.

The SfM workflow begins with the raw image data. After it is uploaded into the software, a like-feature identification process, or locating key points from the overlapping images, is done using a Scale Invariant Feature Transform (SIFT) (Stanton, et al. 2017; Westoby, et al. 2012). SIFT is an object recognition algorithm used to match key points in space regardless of image position and scale (Lowe 2004). The key points are then matched in the overlapping images, so that like-points can create a TIN later in the process (Torres, Arroyo and De Haro 2012). When this is complete the key points are used to reconstruct the camera orientation and 3D position at the moment each image was taken (also known as the 'scene' at each instance an image was taken) via a bundle block adjustment as well as solving error due to intrinsic camera parameters, creating a sparse point cloud (Stanton, et al. 2017; Torres, Arroyo and De Haro 2012). In this step, the GCPs are input to readjust the the network and make the projected location more accurate.

Following this process, the sparse point cloud is densified through keypoint verification using a densification algorithm (Westoby, et al. 2012).

Using the 3-D points from the densified point cloud, a triangulated irregular network (TIN) is created, and from this, a DSM is made (Stanton, et al. 2017). At this point, the image reflectance can be calibrated using the imagery taken of the reflectance card before/after the flight. This assures that radiometric corrections are applied and that factors such incoming sunlight irradiance, sensor responses, aperture, and other factors are accounted for (Pix4D 2011-2018). From here, orthomosaics and/or reflectance maps can be created. In the case of this project, reflectance maps were used because the pixel values better indicate the true reflectance of the object. The generation of a reflectance map uses radiometric corrections to produce a product that is truest to the values it reflects. As mentioned, an orthomosaic can also be created from the TIN, in which case the intensity colors of each image will be adjusted to ‘balance’ them so they fit will together, creating a visually pleasing image (Pix4D 2011-2018).

3.2 VI Calculations

Spectral VIs consist of various arithmetic calculations of two or more spectral bands, allowing spatial patterns to be extracted from each reflectance map (Vina, et al. 2011, Rasmussen, et al. 2015, Mulla 2013). There are multiple formulas for extracting information using VIs because of the numerous quantities of image band and value calculations, each producing a unique result. Every VI creates unique pixel values that can be both viewed in the image and extracted for quantitative analysis. Different VIs highlight several information’s about the vegetation, such as soil moisture, chlorophyll content, leaf area index (LAI), or greenness (Rasmussen, et al. 2015, Jiang, et al. 2008). This is done by using the spectral band width that best corresponds to the problem at hand, such as using the red band to observe chlorophyll and/or additional plant pigments (Mulla 2013).

A total of 25 VIs were chosen for this study, all created from different combinations from the 4-band multispectral Sequoia sensor (shown in Table 3). Each VI was created for a different purpose, such as determining the amount of chlorophyll in a crop (an explanation of each VIs purpose is provided below). The table of indices is organized to separate the indices due to the 'type' of index. Listed first are VIs that contain standardized results from -1 to 1. The NDVI, the most popular and widely used VI as described in the introduction, is a measure of chlorophyll content (Rasmussen, et al. 2015), 'greenness' due to levels of chlorophyll (Gago, et al. 2015), leaf area, plant cover, and nitrogen content (Hansen and Schjoerring 2003). NDVI RE is a 'spin off' of the NDVI and may provide more acute information about areas of chlorophyll concentrations (Kross, et al. 2014). The Enhanced Normalized Difference Vegetation Index (ENDVI) equation was used from a study by Rasmussen, et al. 2015 and is very similar to the NDVI, but also uses the green band, which is related to leaf chlorophyll content, where a higher reflectance means there are greater amounts of chlorophyll (Jannoura, et al. 2014). The Enhanced Normalized Difference Vegetation Index Red-Edge (ENDVI RE) was also used from Rasmussen, et al. 2015 and uses the red-edge band in place of the near-infrared. The Green Normalized Difference Vegetation Index, as described in the introduction, uses the green band, rather than the red, as in the NDVI formula. This band, according to (Mulla 2013), makes the formula more sensitive to changes in chlorophyll content and yield prediction than the NDVI. The Green Normalized Difference Vegetation Index Red-Edge (GNDVI RE) uses the red-edge band in place of the near-infrared. Another VI based on the NDVI is the Normalized Green-Red Difference Index (NGRDI) that is used to estimate active photosynthesis and uses the green and red bands, not needing the near-infrared band that is so common in multispectral imagery (Gitelson, et al. 2002). An indicator of chlorophyll was introduced as the Normalized Difference Red Edge Index (NDRE) which uses the NIR and RE bands in the NDVI formula format (Li, et al. 2014). Along with the NDRE, the MERIS Terrestrial Chlorophyll Index (MTCI) is also an accurate depicter of plant chlorophyll and nitrogen content (Schlemmer, et al. 2013).

Three ratio VIs were also chosen for this study. These indices were chosen according to their usefulness at detecting chlorophyll amounts and overall healthiness in crops, as this is commonly associated to iron chlorosis. These VIs are ratios, giving them no standardized results. The Simple Ratio (SR) responds to the contrast between chlorophyll absorption in the R portion of the spectrum and the scattering in the NIR region (Mutanga and Skidmore 2004). It is a good estimator of canopy chlorophyll content, with a larger ratio representing denser canopy and higher chlorophyll content due to the absorption of red wavelengths (Kross, et al. 2014). The Normalized Red (NR) and Normalized Green (NG) are very similar except for the fact that the NR concentrates on the portion of the spectrum where wavelengths are absorbed by chlorophyll in the red region and the NG focuses on the area of the spectrum where other plant pigments (instead of chlorophyll) absorb energy (Mulla 2013). As described above, there are a wide assortment of image band combinations, each with a different application of purpose (Apan, et al. 2003). Some VIs however, can be affected by soil reflectance, atmospheric refraction, and other factors that can affect canopy cover reflection, especially in areas of sparse vegetation (Mulla 2013; Gago, et al. 2015). It was also found, in a number of studies, that soils with darker reflection resulted in a higher value of index when VIs were calculated and vice versa for soils with light reflections (Huete 1988). The third portion of table 2 contains a list of soil-adjusted VIs, with their respective equations, that were also calculated during this study to account for these extraneous influences (Apan, et al.

2003). The first two of these equations are the Difference Vegetative Index (DVI) and Difference Vegetative Index Red-Edge (DVI RE), which are sensitive to greenness and plants with active photosynthesis (Tucker 1979). The difference between the NIR and R bands and RE and R bands is thought to compensate for soil reflectance (Mulla 2013) because of the high absorption of chlorophyll in the R region (Tucker 1979). The Green Difference Vegetative Index (GDVI) and Green Difference Vegetative Index Red-Edge (GDVI RE) uses the G band, rather than the R as in the DVI, because G contains a lower soil-to-vegetation contrast. Chlorophylls are only slightly absorbed in this region, making this VI more sensitive to green biomass (Tucker 1979). The Soil Adjusted Vegetation Index (SAVI) was developed to be comparable to NDVI, but not containing soil-vegetation effects (Huete 1988). The equation contains a constant L that is an adjustment factor for different vegetation densities that include L = 1, for low density, L = 0.5 for intermediate density, and L = 0.25 for high density with L = 0.5 being determined the 'optimal' adjustment for reducing soil-induced noise (Rondeaux, Steven and Baret 1996) An extension of SAVI, called the Optimized Soil Adjusted Vegetation Index (OSAVI) contains a more specific constant value, which is said to perform better in reducing soil noise in vegetation cover that is over 50% (Rondeaux, Steven and Baret 1996). The Optimized Soil Adjusted Vegetation Index Red-Edge (OSAVI RE) serves the same purpose as the OSAVI, using the RE band in place of the NIR, and contained the same L values as the SAVI. The Transformed Vegetation Index (TVI), which is sensitive to greenness (Tucker 1979), returns the contrast of absorption in the R region against scattering in the NIR (Mutanga and Skidmore 2004). The Transformed Vegetation Index Red-Edge (TVI RE), is also an extension of the TVI, using the RE band in place of the NIR (L-values for the TVI and TVI RE were the same as the SAVI and SAVI RE). Lastly, the Enhanced Vegetation Index 2 (EVI2) was developed to be used in place of the Enhanced Vegetation Index

(EVI), which uses the blue band, in cases where the blue band is not available. This VI was made to be more sensitive in regions of high canopy cover, improve plant observations, and enhance vegetative signal (Jiang, et al. 2008). Examples of the indices listed above are displayed in Figure 9. The Enhanced Vegetation Index 2 Red-Edge (EVI2 RE) is also an extension of the EVI, using the RE band in Place of the NIR.

The L factor was determined by beginning, early-middle, middle, or end of season, when the plants were in different stages of growth. The beginning of the season, which used a value of L = 1 began on May 5, 2017 and ended on May 17, 2017. The early mid-season began on May 23, 2017 and ended June 13, 2017 and used the ‘optimal’ value of L = 0.5. Mid-season, when the plants were at their peak was from June 22, 2017 to July 6, 2017 and used a value of L = 1. At the end of the season the plants have peaked and start to die before yield is taken. The value for the end of season VIs was L = 0.5 from July 15, 2017 to July 27, 2017. The plants’ stages of growth were determined by a group of analysts that work at Texas A&M AgriLife Research and Extension Center. These include the preflowering stage (when the plants contain up to seven leaves), approaching flower (the boot stage) and through flowering, and the reproductive stage, where the grain develops and hardens (Stanton, et al. 2017), simply called early, mid, and late season in this study, respectively.

As mentioned in the Introduction, the RE band provides more acute information regarding vegetation health (Hansen and Schjoerring 2003). This band covers a range in the spectrum that is highly influenced by chlorophyll concentrations and is sensitive to variants of green within crop types (Ramoelo, et al. 2012, Clevers and Gitelson 2013, Mutanga and Skidmore 2004). RE captures “NIR incident radiation” that reflects off the plant leaves and, in some cases, is thought to estimate greenness variations in crops better than the NIR band (Seager, et al. 2005, Mutanga and Skidmore 2004). For these reasons, the NIR band was replaced with the RE band in a total of 8 equations to study the differences of the two bands when detecting iron chlorosis in the grain sorghum crop. These include the ENDVI RE, GNDVI RE, DVI RE, GDVI RE, SAVI RE, OSAVI RE, TVI RE, and EVI2 RE. Examples of all 25 VIs are displayed from the flight date on July 22, 2017 in Figure 13 below.

Table 3: A list the VIs calculated in this study. The VIs were calculated for every flight date (12 in total). The type of VI and resulting range of values for each is also shown.

Vegetation Index (VI)	**Abbreviation**	**Definition**	**Type**	**Range of Values**
Difference Vegetative Index	DVI	$\mathrm{NIR} - \mathrm{R}$	Soil Adjusted	-1 to 1
Difference Vegetative Index Red Edge	DVI_RE	$\mathrm{RE} - \mathrm{R}$	Soil Adjusted	-1 to 1
Enhanced Normalized Difference Vegetation Index	ENDVI	$\frac{(\mathrm{NIR} + \mathrm{G}) - 2\mathrm{R}}{(\mathrm{NIR} + \mathrm{G}) + 2\mathrm{R}}$	Standard	-1 to 1
Enhanced Normalized Difference Vegetation Index – Red Edge	ENDVI RE	$\frac{(\mathrm{RE} + \mathrm{G}) - 2\mathrm{R}}{(\mathrm{RE} + \mathrm{G}) + 2\mathrm{R}}$	Standard	-1 to 1
Enhanced Vegetation Index 2	EVI2	$2.5\left[\frac{\mathrm{NIR} - \mathrm{R}}{\mathrm{NIR} + 2.4\mathrm{R} + 1}\right]$	Soil Adjusted	-1 to 1
Enhanced Vegetation Index 2 – Red Edge	EVI2 RE	$2.5\left[\frac{\mathrm{RE} - \mathrm{R}}{\mathrm{RE} + 2.4\mathrm{R} + 1}\right]$	Soil Adjusted	-1 to 1
Green Difference Vegetative Index	GDVI	$\mathrm{NIR} - \mathrm{G}$	Soil Adjusted	-1 to 1
Green Difference Vegetative Index Red Edge	GDVI RE	$\mathrm{RE} - \mathrm{G}$	Soil Adjusted	-1 to 1
Green Normalized Difference Vegetation Index	GNDVI	$\frac{\mathrm{NIR} - \mathrm{G}}{\mathrm{NIR} + \mathrm{G}}$	Standard	-1 to 1
Green Normalized Difference Vegetation Index – Red Edge	GNDVI RE	$\frac{\mathrm{RE} - \mathrm{G}}{\mathrm{RE} + \mathrm{G}}$	Standard	-1 to 1
Green Optimized Soil Adjusted Vegetation Index	GOSAVI	$\frac{\mathrm{NIR} - \mathrm{G}}{\mathrm{NIR} + \mathrm{G} + 0.16}$	Soil Adjusted	-1 to 1

MERIS Terrestrial Chlorophyll Index	MTCI	$\frac{\mathrm{NIR} - \mathrm{RE}}{\mathrm{RE} + \mathrm{R}}$	Standard	-1 to 1
Normalized Difference Red Edge Index	NDRE	$\frac{\mathrm{NIR} - \mathrm{RE}}{\mathrm{NIR} + \mathrm{RE}}$	Standard	-1 to 1
Normalized Difference Vegetation Index	NDVI	$\frac{\mathrm{NIR} - \mathrm{R}}{\mathrm{NIR} + \mathrm{R}}$	Standard	-1 to 1
Normalized Difference Vegetation Index – Red Edge	NDVI RE	$\frac{\mathrm{RE} - \mathrm{R}}{\mathrm{RE} + \mathrm{R}}$	Standard	-1 to 1
Normalized Green	NG	$\frac{\mathrm{G}}{\mathrm{NIR} + \mathrm{R} + \mathrm{G}}$	Ratio	None
Normalized Green-Red Difference Index	NGRDI	$\frac{\mathrm{G} - \mathrm{R}}{\mathrm{G} + \mathrm{R}}$	Standard	-1 to 1
Normalized Red	NR	$\frac{\mathrm{R}}{\mathrm{NIR} + \mathrm{R} + \mathrm{G}}$	Ratio	None
Optimized Soil Adjusted Vegetation Index	OSAVI	$\frac{\mathrm{NIR} - \mathrm{R}}{\mathrm{NIR} + \mathrm{R} + 0.16}$	Soil Adjusted	-1 to 1
Optimized Soil Adjusted Vegetation Index Red Edge	OSAVI RE	$\frac{\mathrm{RE} - \mathrm{R}}{\mathrm{RE} + \mathrm{R} + 0.16}$	Soil Adjusted	-1 to 1
Soil Adjusted Vegetation Index	SAVI	$1 + \mathrm{L}\left[\frac{\mathrm{NIR} - \mathrm{R}}{\mathrm{NIR} + \mathrm{R} + \mathrm{L}}\right]$	Soil Adjusted	-1 to 1
Soil Adjusted Vegetation Index Red Edge	SAVI RE	$1 + \mathrm{L}\left[\frac{\mathrm{RE} - \mathrm{R}}{\mathrm{RE} + \mathrm{R} + \mathrm{L}}\right]$	Soil Adjusted	-1 to 1
Simple Ratio	SR	$\frac{\mathrm{NIR}}{\mathrm{Red}}$	Ratio	None
Transformed Vegetation Index	TVI	$\left[\sqrt{\frac{\mathrm{NIR} - \mathrm{R}}{\mathrm{NIR} + \mathrm{R}} + \mathrm{L}}\right]$	Soil Adjusted	-1 to 1
Transformed Vegetation Index Red Edge	TVI RE	$\left[\sqrt{\frac{\mathrm{RE} - \mathrm{R}}{\mathrm{RE} + \mathrm{R}} + \mathrm{L}}\right]$	Soil Adjusted	-1 to 1

Figure 13: A display of all of the different VIs computed for reflectance maps collected on June 22, 2017. Each VI map is depicted by the high and low values of each dataset.

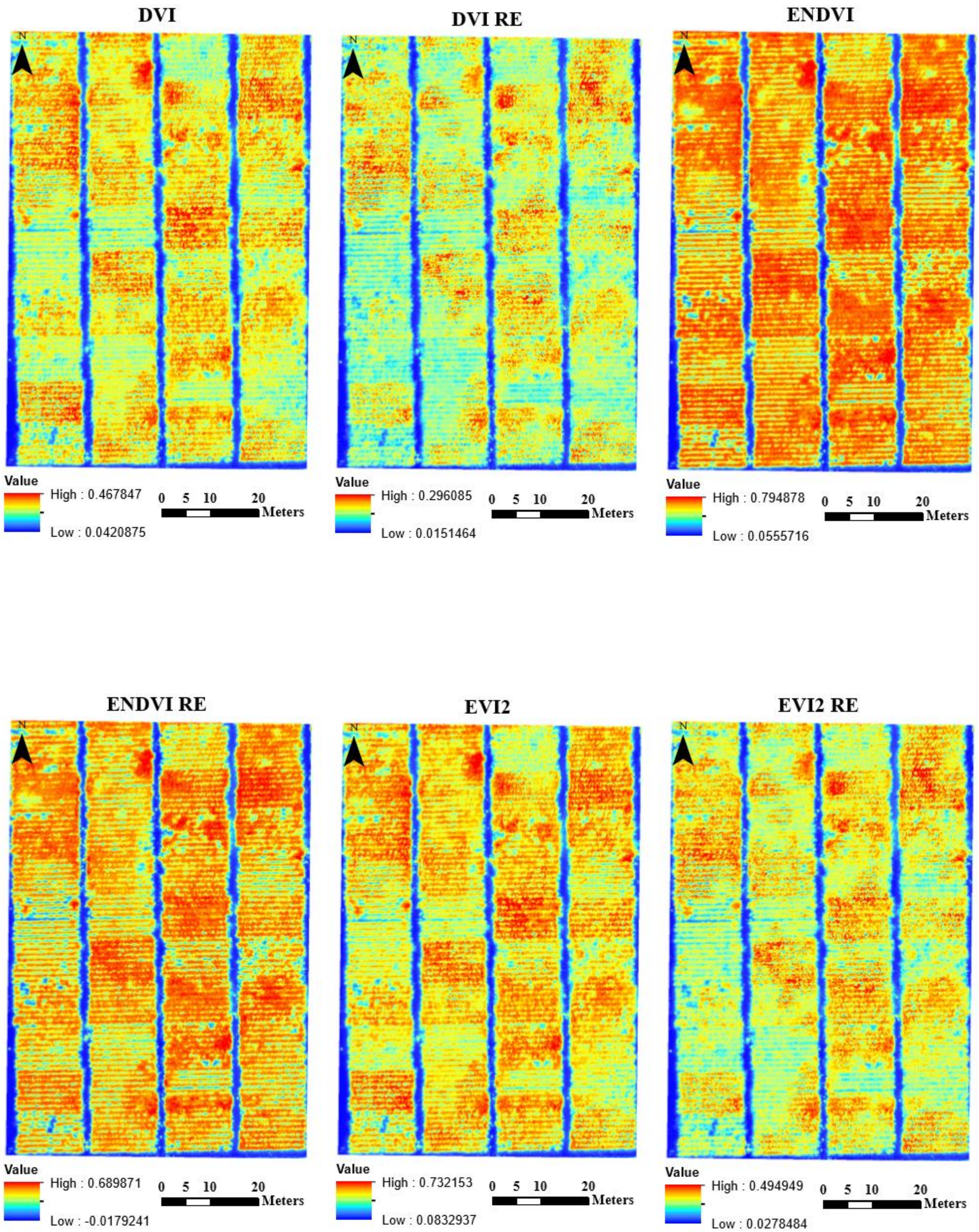

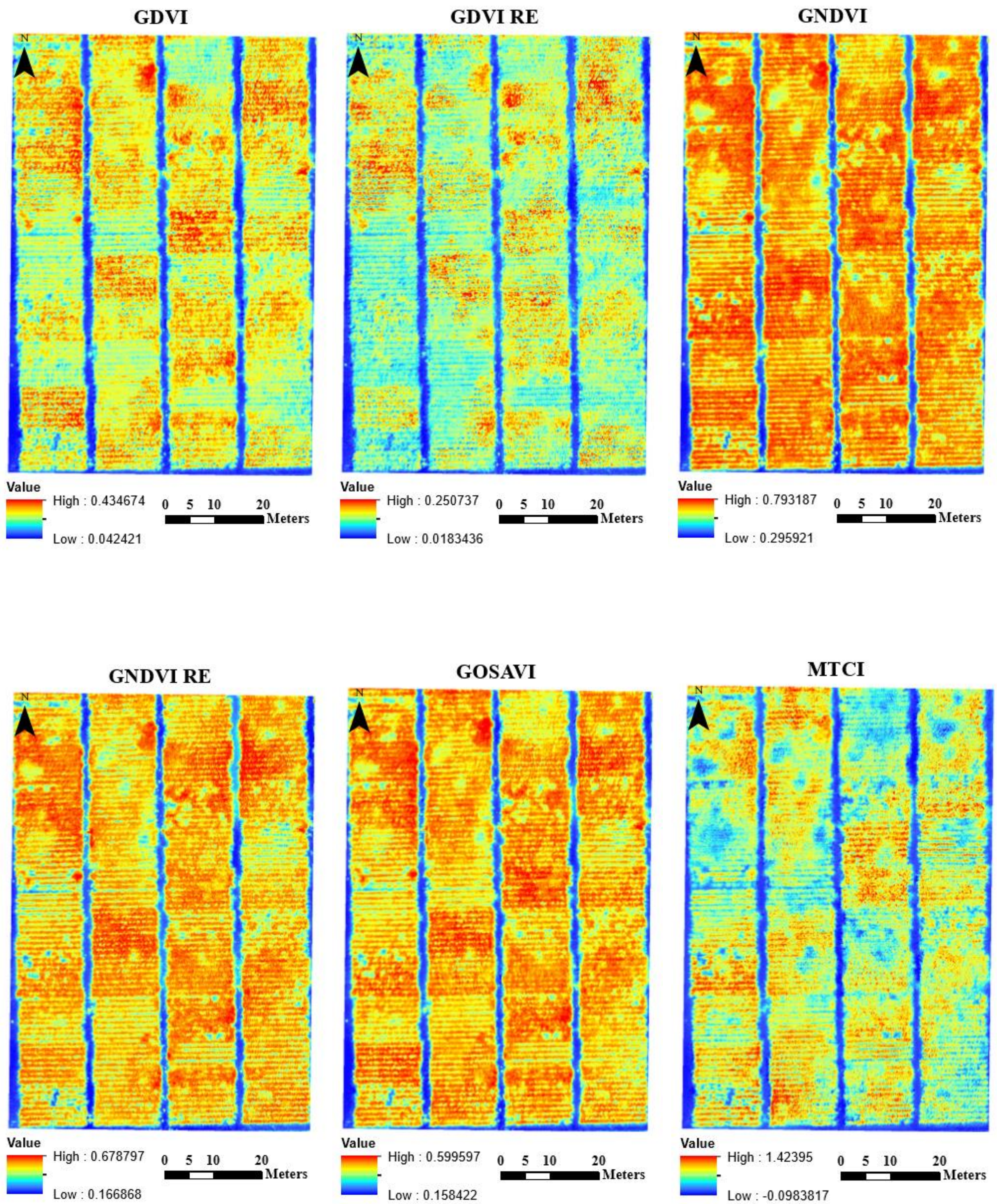
GDVI
Value
High : 0.434674
Low : 0.042421
0 5 10 20
Meters
GDVI RE
Value
High : 0.250737
Low : 0.0183436
0 5 10 20
Meters
GNDVI
Value
High : 0.793187
Low : 0.295921
0 5 10 20
Meters
GNDVI RE
Value
High : 0.678797
Low : 0.166868
0 5 10 20
Meters
GOSAVI
Value
High : 0.599597
Low : 0.158422
0 5 10 20
Meters
MTCI
Value
High : 1.42395
Low : -0.0983817
0 5 10 20
Meters

NDRE

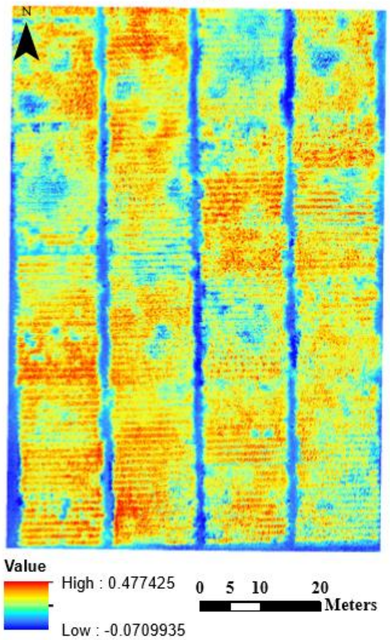

NDVI

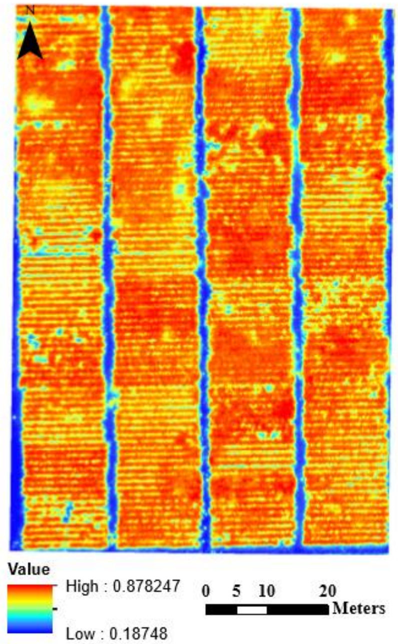

NDVI RE

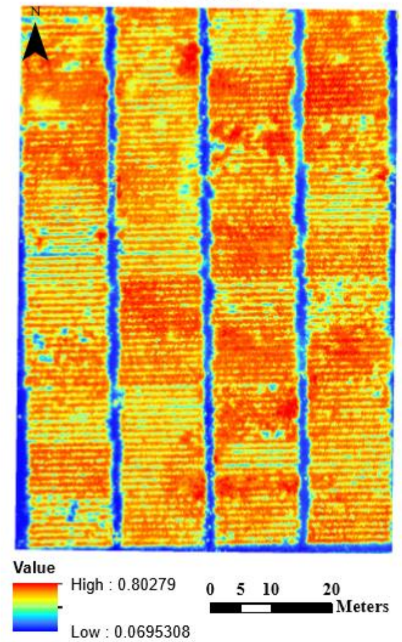

NG

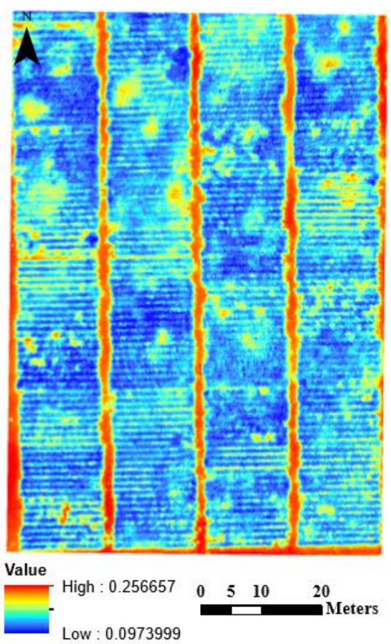

NGRDI

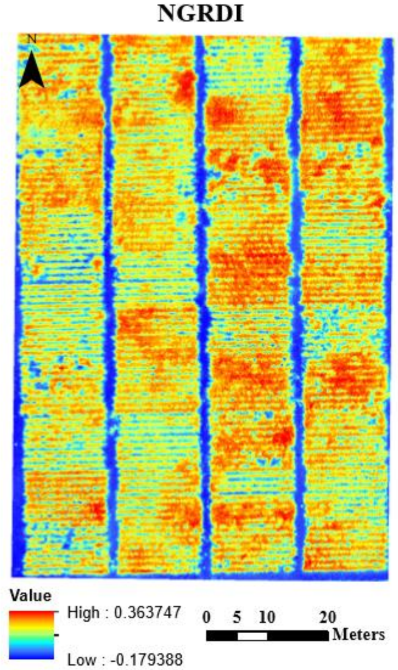

NR

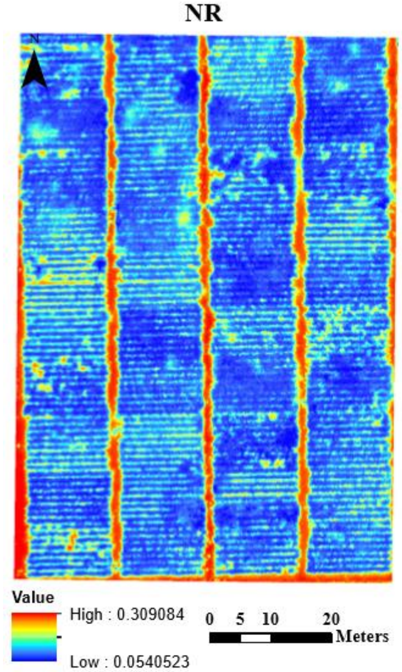

OSAVI

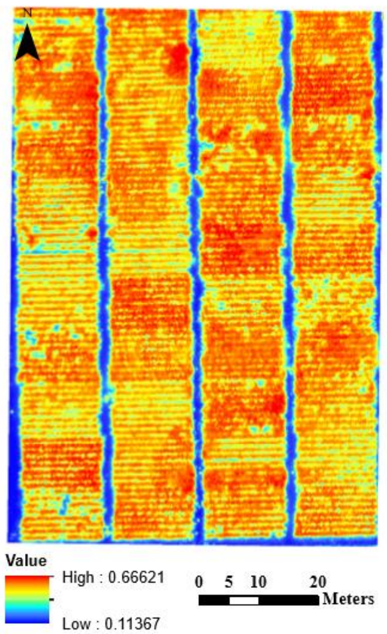

OSAVI RE

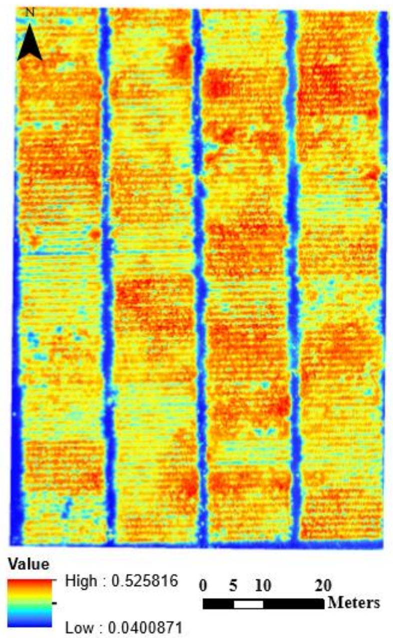

SAVI

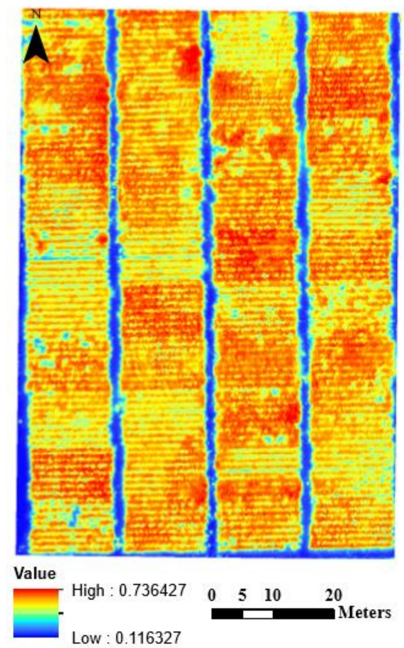

SAVI RE

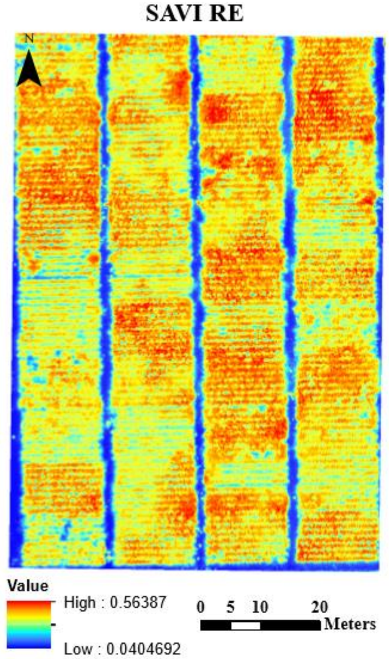

SR

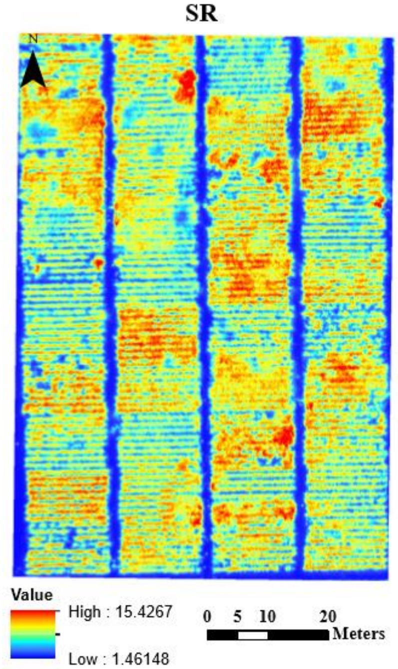

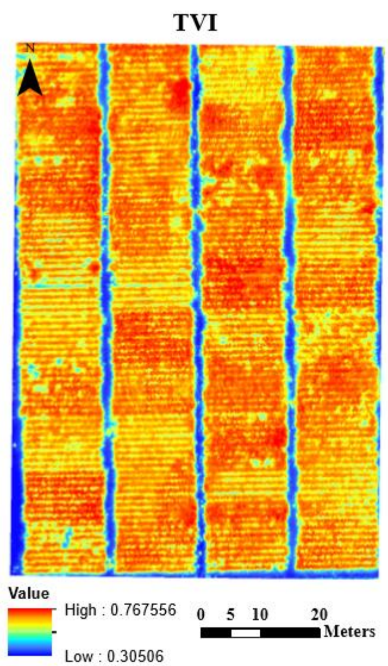

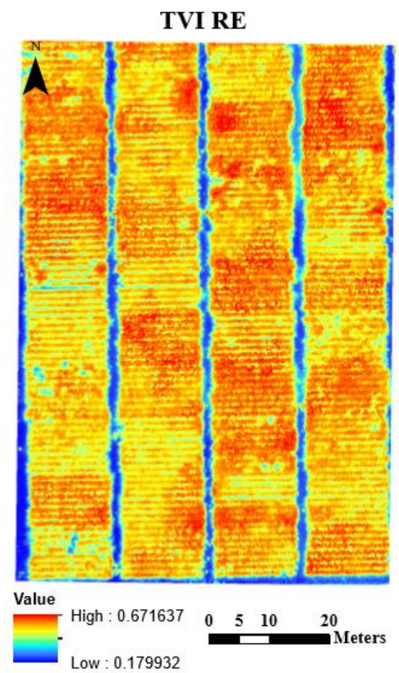

3.3 Canopy Cover Extraction

Although the VIs used in this study were developed to observe spatial patterns in crops, many of them that decipher stressed vegetation well could have potential noise from soil reflectance, especially in areas of low canopy cover (Mulla 2013). Even the soil adjusted VIs could have error due to extraneous factors that cause them to perform poorly. As a solution, the process of canopy cover extraction and soil removal from the image bands before calculating vegetation indices was implimented. This was thought to remove interference from soil background and deliver truer values from the calculated VIs.

The methodologies and processes used to complete the canopy cover extraction were researched extensively, as there were many ideas for completing this. First, a method was sought to match that of Canopeo; a program designed to compute 'Fractional Green Canopy Cover (FGCC)' by using RGB imagery in a series of band ratios (blue to green and red to green) and VIs (mainly an excess green index, which uses red, green, and blue) (Patrignani and Ochsner 2015).

The ease of use of a developed program for this step allowed a question to be asked: ’is there a band/band combination that could equal that of the blue band?’ Because this project uses red-edge and NIR bands instead of blue, an alternate method was needed to extract canopy cover.

This led to the research of another canopy cover metric that is based on multispectral imagery. However, after extensive exploration, it was discovered that there are not many ‘canopy cover metrics’ for this type of research. Further investigation concluded that the two most popular methods of removing background objects (i.e. soil background, non-plant, and unwanted objects) among researchers using multispectral imagery were: 1) image thresholding based on VIs and 2) supervised image classification methods. These methods were only tested on the reflectance maps from one date, May 17, 2017 because it was the first date in which the plants were fuller and more vegetation samples could be taken, yet not too full for the areas between rows to be covered with vegetation (the vegetation is separated by rows of soil). The two methods were then compared to determine which method better extracted the canopy cover.

3.3.1 Image Thresholding

As mentioned above, image thresholding is a popular method of canopy cover extraction that involves creating a maximum pixel on which to base the image. The process behind this method normally consists of calculating a VI, observing the histogram associated with this VI, and creating a ‘threshold,’ or a limiting pixel value. The NDVI is very commonly used when creating a threshold as shown by (Berni, et al. 2009, Bhandari, Kumar and Singh 2012, Hall, Louis and Lamb 2003, Roosjen, et al. 2017). Each of these sources uses a different thresholding value to eliminate soil background. All values were created uniquely for each image through use of the image’s histogram. For example, Hall et.al. 2003 created two unique threshold values (one for soil and one for mixed soil and vine pixels) based on two histogram peaks. Using these, he eliminated all pixels that were not solely vegetation. Lum, et al. 2016 also created a binary map based off of a threshold value of 0.6 to most accurately determine the amount of healthy vegetation within the study area. Lastly, (Roosjen, et al. 2017) chose a threshold value of 0.7, where all numbers between 0.7 and 1.0 were classified as vegetation. This value was chosen based on ‘visual inspection’ where the author believed this was an acceptable value to separate vegetation and soil background pixels. This method was tried in the multispectral data for the reflectance maps collected on May 17, 2017. First, the NDVI RE was computed using the red-edge and red bands. Then, using the histogram, a ballpark value was determined for the threshold value. After, a known, highly stressed area was focused on for validation of pixel values. In this area, individual pixels were examined for both highly stressed plants and the surrounding soil. From here, a threshold value of 0.30 was determined to be the cutoff value for this date (everything above being vegetation, including highly stressed plants) and was used to create a binary file representing vegetation and non-vegetation pixels. This image was converted into a polygon file and then used to crop soil and other background pixels from the reflectance maps as demonstrated in Figure 14 (the green band is displayed as an example of the process).

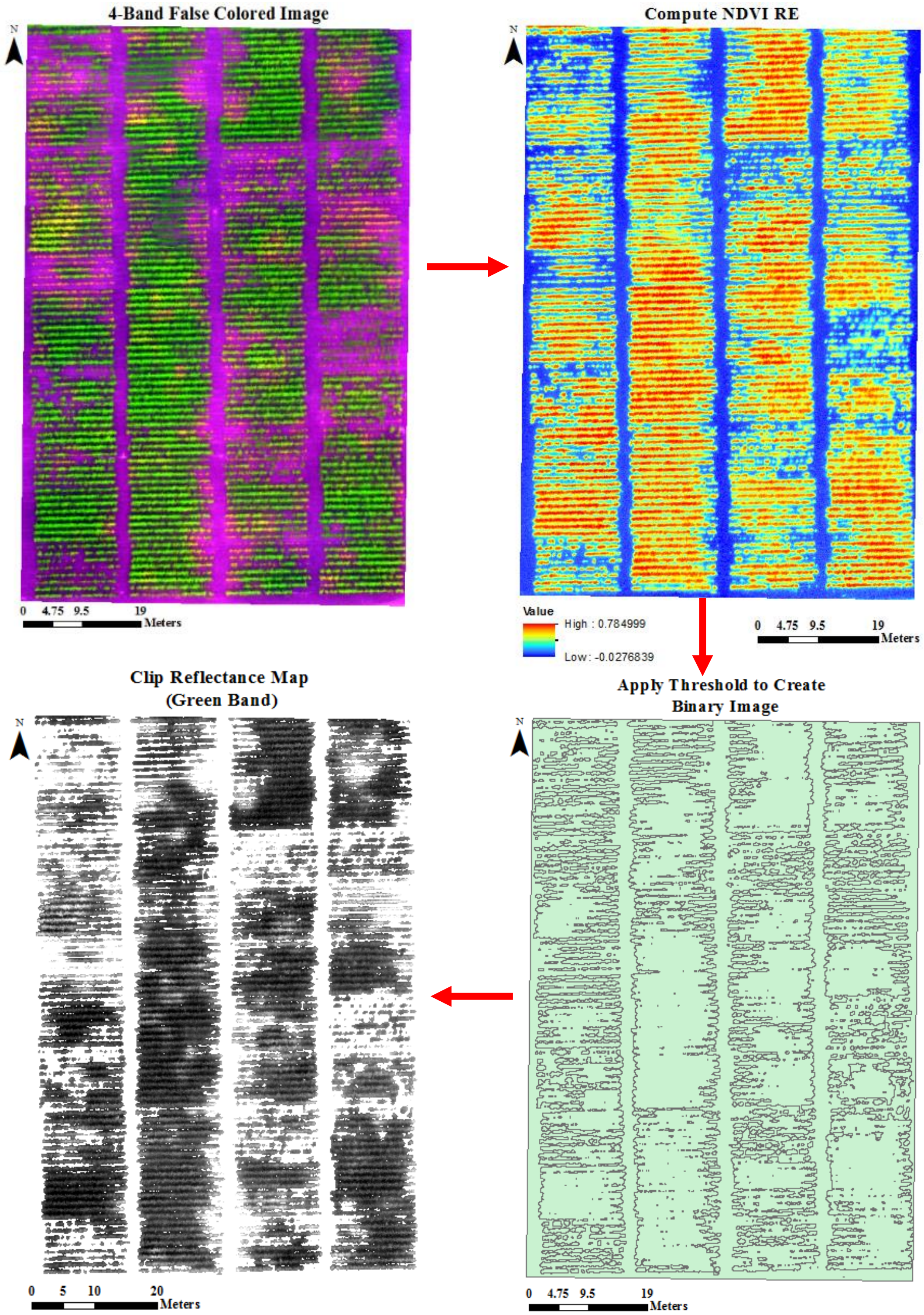

Figure 14: Canopy cover extraction via image thresholding on a combined 4-band false colored reflectance map collected on May 17, 2017. The NDVI RE was computed, and values for a known area of high stress was observed to determine a threshold value (0.30). After the value was applied a binary image was created and used to crop the individual image bands (displayed in a combined 4-band false colored reflectance map.

3.3.2 Supervised Classification

The second method of canopy cover extraction used in this project was completed by using a maximum likelihood supervised classification. There are two main approaches of image classification: supervised and unsupervised. In the unsupervised approach, the classes that are to be made are unknown and a clustering method is used to generate groups of data. The analyst need not take samples of the data, but merely input the number of desired classes, if they would like to do so (it is not required) (Omran, Engelbrecht and Salman 2005). Supervised classification requires more user-involvement in the classification process such as manually picking out training samples to 'train' the classifier before it runs, creating a signature for the classification.

There are many types of supervised classification, such as Support Vector Machines (SVM), Maximum Likelihood (ML), Decision Tree (DT), Index-Based (IB), Fuzzy (FZ), K-Means (KM), etc (Khatami, Mountrakis and Stehman 2016). Each supervised classification method works differently, for example a DT classifier has one principal node that acts as the root of the decision tree, which splits into a series of internal nodes, which are then split into terminal nodes. The data is divided down the tree to the desired classes (Otukei and Blaschke 2010). SVM classifiers create 'planes' to separate the data and provide as much separation between these planes as possible (Otukei and Blaschke 2010). The type of supervised classification used in this study is ML, which is a popular and widely used method. This method does not have a minimum sample number, and can classify both linear and non-linear data (Sisodia, Tiwari and Kumar 2014; Otukei and Blaschke 2010). This type of classifier separates data X (in this case pixels) based on its weighted likelihood (or probability) to belong to a certain class. It also takes into account the variance-covariance describing the interrelationship of the said pixels, assigning each pixel to one of the classes (Otukei and Blaschke 2010; Strahler 1980).

The process of a ML supervised classification involved manually choosing ‘training samples’ from the image, which included creating two types of samples: one for soil and one for vegetation. When a sufficient number of samples were taken from the image, spectral signatures of said samples were then used to ‘train’ the classier to extract like signatures.

The training samples used for this study were chosen by the author who had previous knowledge of the sorghum field. At least 1,000 pixels were included in each training class (one class for vegetation, one class for background noise such as soil, targets, etc.). Some areas that were difficult to sample were areas of intense iron chlorosis. The pixel values were, in some cases, very similar to those of the soil. This is where the georeferenced plants were useful. The points and polygons were used to determine what areas and plants were iron chlorotic and these areas were carefully picked to train the classifier for maximum accuracy. These areas were particularly important to focus on because these plants and segments are what is desired to be located in the imagery and analyzed using the VIs. It was vital that the classifier did not wrongly classify this vegetation as soil and exclude it from the resulting image.

A maximum likelihood classifier was used to extract the spectral information from the compiled multispectral image bands by separating the pixels into the class of the highest probability of belonging (Otukei and Blaschke 2010). This resulted in a binary classification of pixels, one class for soil, and the other for canopy. When the classification was complete, the raster image could be converted into a polygon file that could be manipulated to exclude one of the two classes (in this case, the soil class). This canopy shape file was then used to crop the individual raster image bands, which could then be used to create additional VIs. The workflow for extracting canopy cover with a supervised classification is demonstrated in Figure 15.

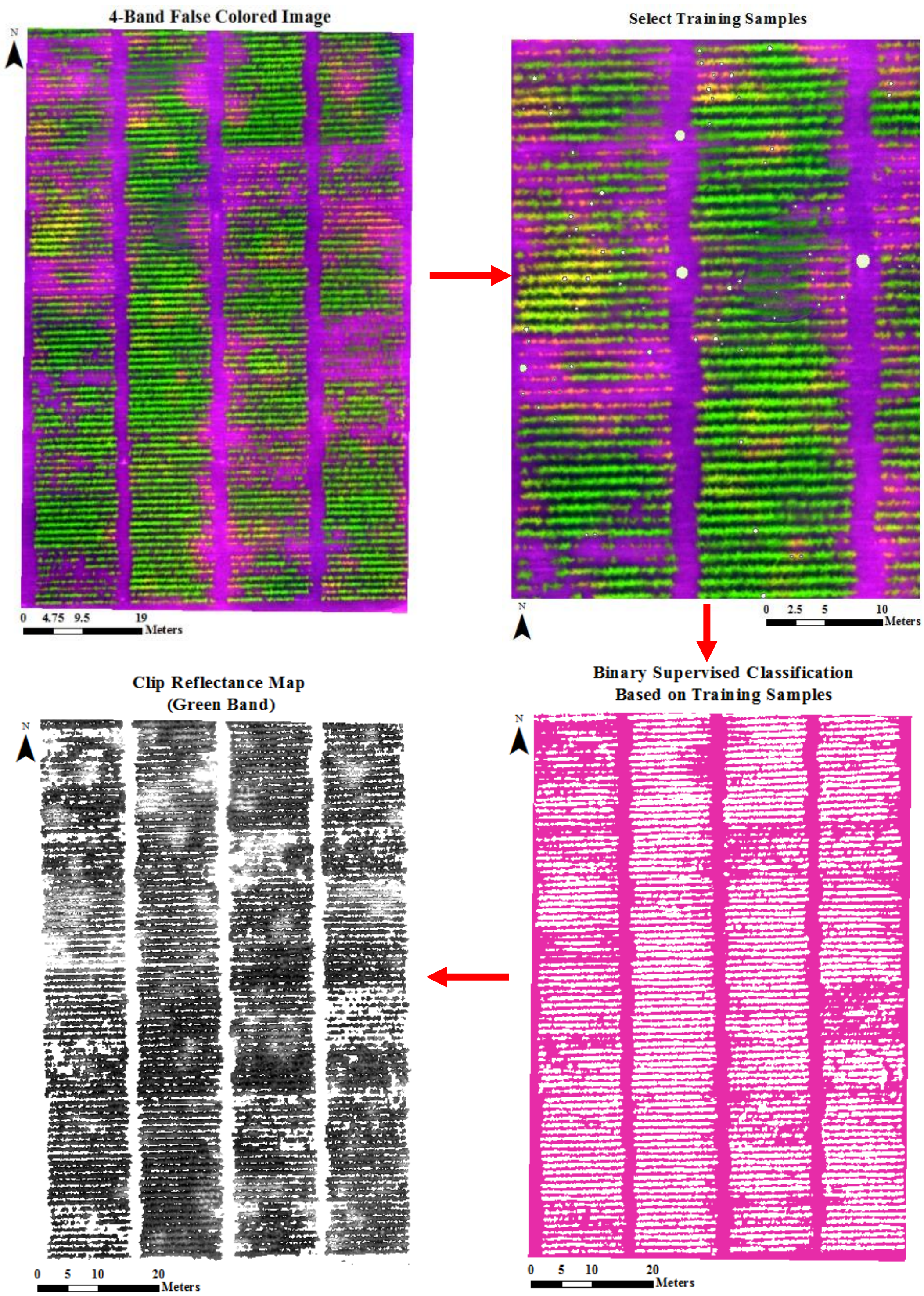

Figure 15: Supervised binary, maximum likelihood classification method used to extract canopy cover. First, training samples are manually chosen from a 4-band reflectance map, collected on May 17, 2017, to mark areas of vegetation and areas of background (soil, targets, etc). Then, the samples are used to classify the reflectance map based on which pixels are 'most likely' to fall into each category. When the classification is complete, the resulting image is used to clip the individual bands, resulting in a soil-removed reflectance map (the band shown here is green).

3.3.3 Thresholding vs Classification

After extracting canopy cover with both methods of classification and threshold, it was determined that supervised classification was more accurate at eliminating background soil from the reflectance maps. This was decided through the computation of a two-class confusion matrix, which uses random sample pixels to determine the accuracy of a classifier, where the said sample pixels can be separated into a single class (Lewis and Brown 2010). The sample data was manually picked from the data, a 4-band multispectral image from June 17, 2017. It consisted of 100 pixels per class, the two classes being soil and non-soil, that were spaced throughout the scene. A classifier was then run to predict the accuracy of the supervised classification and the threshold method in comparison to the 'ground truth' sample data. The results were then formed into the confusion matrix.

Two classes existed in the matrix, what an object was actually classified as, and what class the classifier predicted the object belonged to (Deng, et al. 2016). The confusion matrix displayed the number of pixels that were classified correctly, and how many pixels belonged in the other class. A series of accuracies are also computed, the overall accuracy, the user accuracy and the producer accuracy. The accuracies for the threshold method were as follows: overall = 0.8591 (around 86%), user (soil) = 100%, user (canopy) = 79.47%, producer (soil) = 69%, producer (canopy) = 125.83%. Likewise, accuracies for the supervised classification method were as follows: overall = 1.0 (around 100%), user (soil) = 100, user (canopy) = 100%, producer (soil) = 100, producer (canopy) = 84.17%. A comparison of the supervised classification and threshold methods are displayed in Figure 16 for visual comparison.

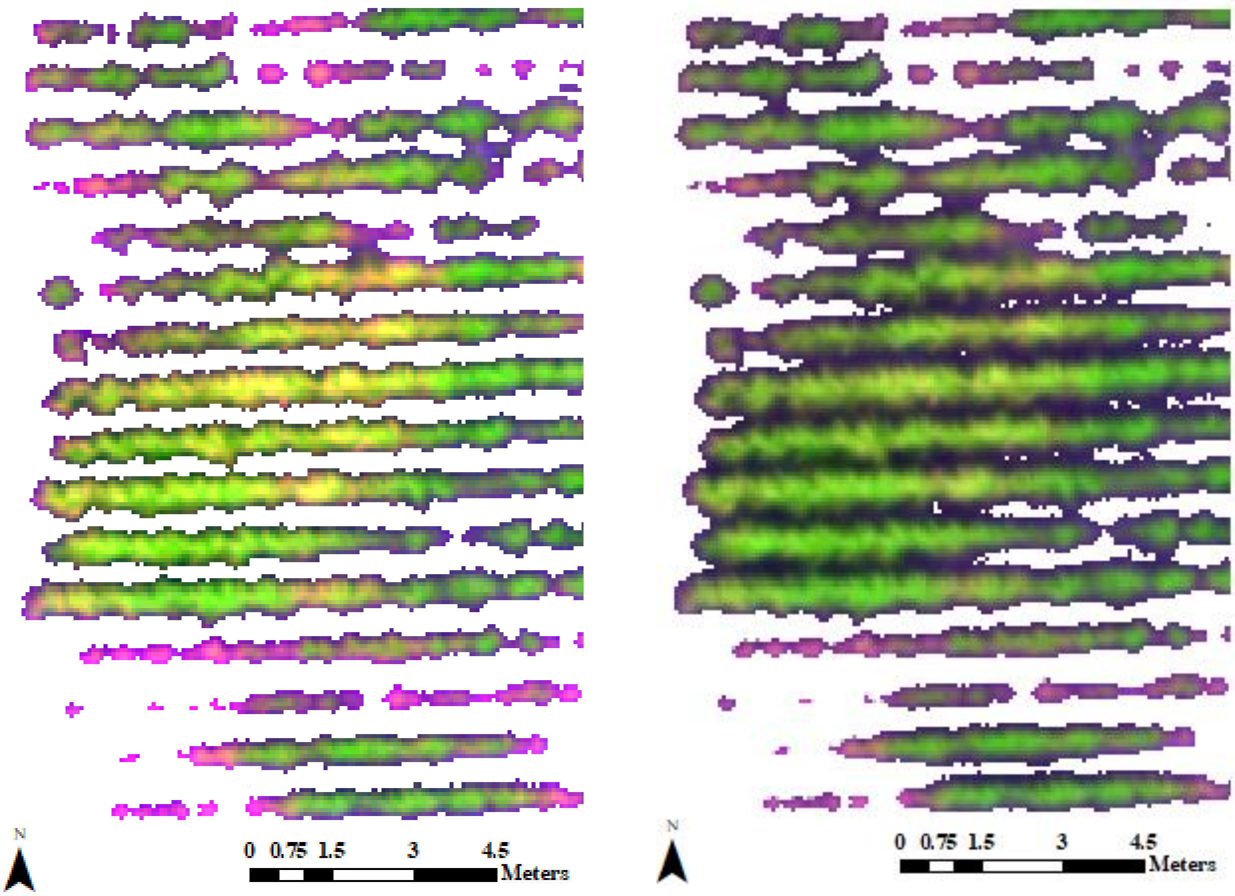

Figure 16: A comparison of methods used for canopy cover extraction for the flight date completed on May 17, 2017, depicted by 4-band false colored reflectance maps. On the left is the supervised classification method, and on the right is the image thresholding method.

Training the classifier allowed the highly stressed plants' pixel values to be viewed by the classifier as vegetation, keeping them in the resulting image. It is possible that the threshold value of 0.30 did not eliminate soil pixels that bordered canopy, but kept the pixels representing plants with severe iron chlorosis. The threshold value could have been set higher to eliminate the bordering soil, but this would have been problematic because of the low values of iron chlorosis. These low values representing stressed vegetation pixels would also have been eliminated if this were done.

To better examine the differences between the two methods of soil removal, the NDVI RE was calculated. Figure 17 and Figure 18 show the resulting images side-by-side. As can be seen from Figure 18, the threshold method contains more soil pixels and does not fully separate rows of healthy vegetation. However, Figure 18 shows that the classification method did indeed separate these rows effectively and also kept the stressed vegetation (shown on the left column of plants, in the center rows).

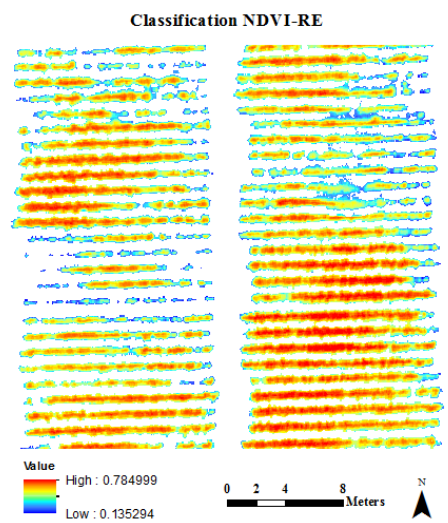

Figure 17: NDVI-RE computed from canopy extracted by ML supervised classification from reflectance maps collected on May 17, 2017.

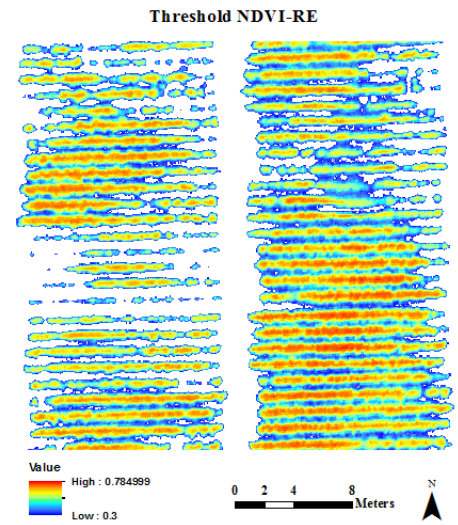

Figure 18: NDVI-RE computed from canopy extracted by threshold from reflectance maps collected on May 17, 2017.

3.4 Canopy Cover VIs

When a method of canopy cover extraction was selected, the chosen VIs (listed in Table 3) were calculated with the soil-removed R, G, RE, and NIR bands for all the VIs across every date. The results, displayed in Figure 19 are displayed in the same color scheme as the soil-included VIs above with red colors representing higher values and blue colors representing lower values. Each VI is depicted with the low and high values being the lowest and highest value resulting from that metric.

Figure 19: A display of all of the different VIs computed for the soil-removed reflectance maps initially collected on June 22, 2017. Each VI map is depicted by the high and low values of each dataset.

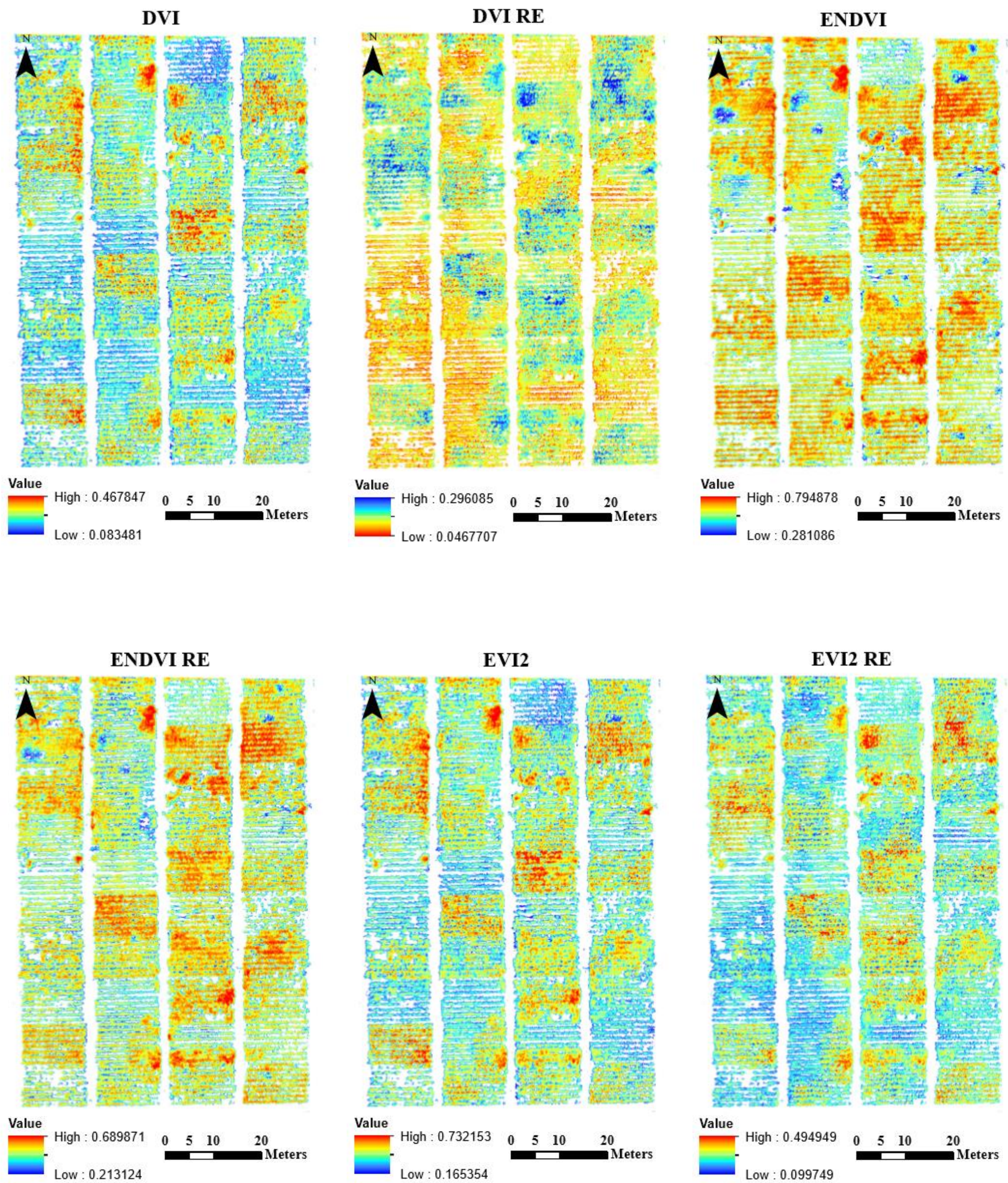

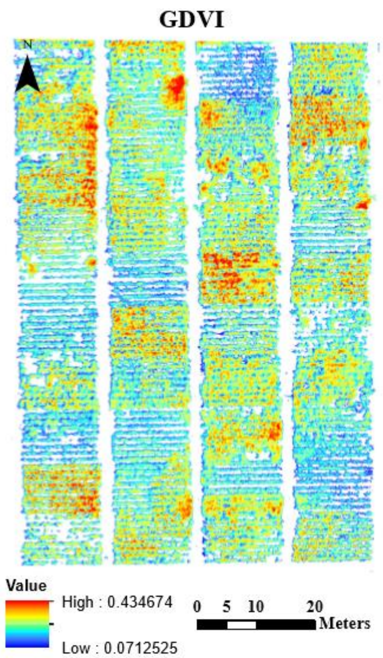
GDVI
N
Value
High : 0.434674
Low : 0.0712525
0 5 10 20
Meters

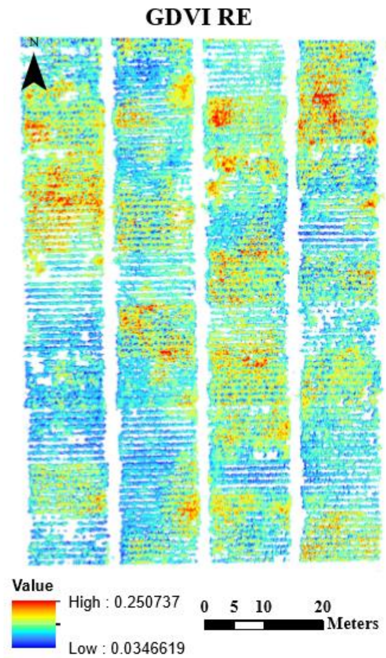
GDVI RE
N
Value
High : 0.250737
Low : 0.0346619
0 5 10 20
Meters

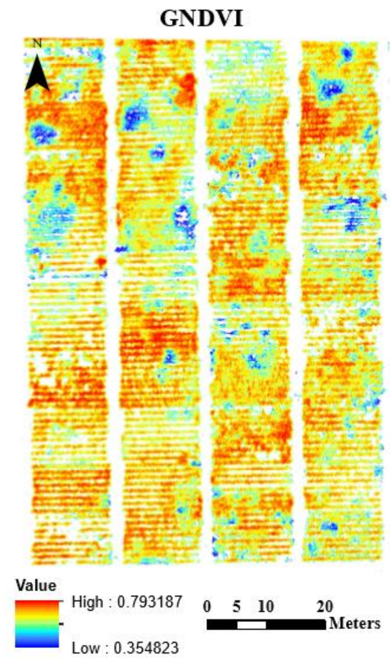
GNDVI
N
Value
High : 0.793187
Low : 0.354823
0 5 10 20
Meters

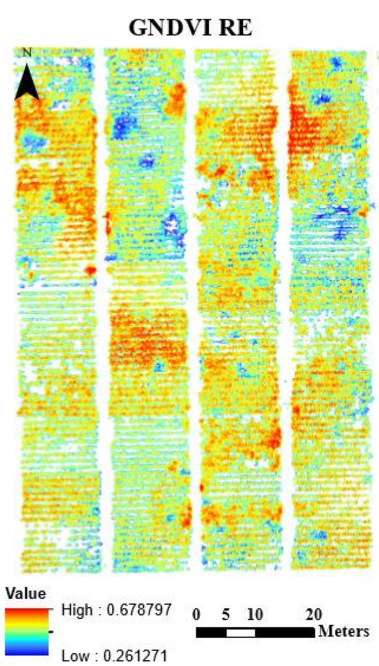
GNDVI RE
N
Value
High : 0.678797
Low : 0.261271
0 5 10 20
Meters

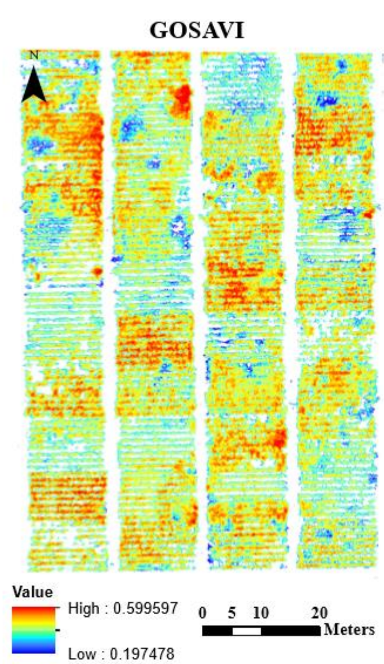
GOSAVI
N
Value
High : 0.599597
Low : 0.197478
0 5 10 20
Meters

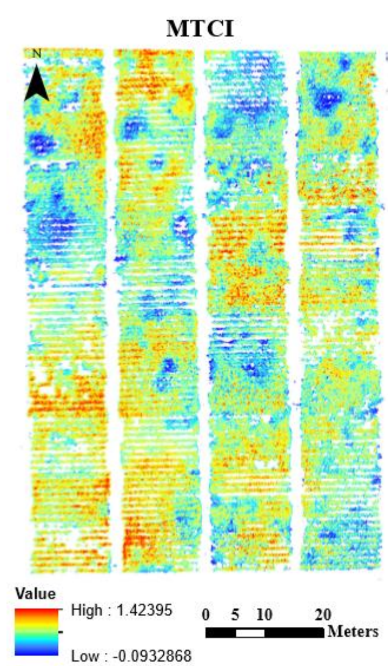
MTCI
N
Value
High : 1.42395
Low : -0.0932868
0 5 10 20
Meters

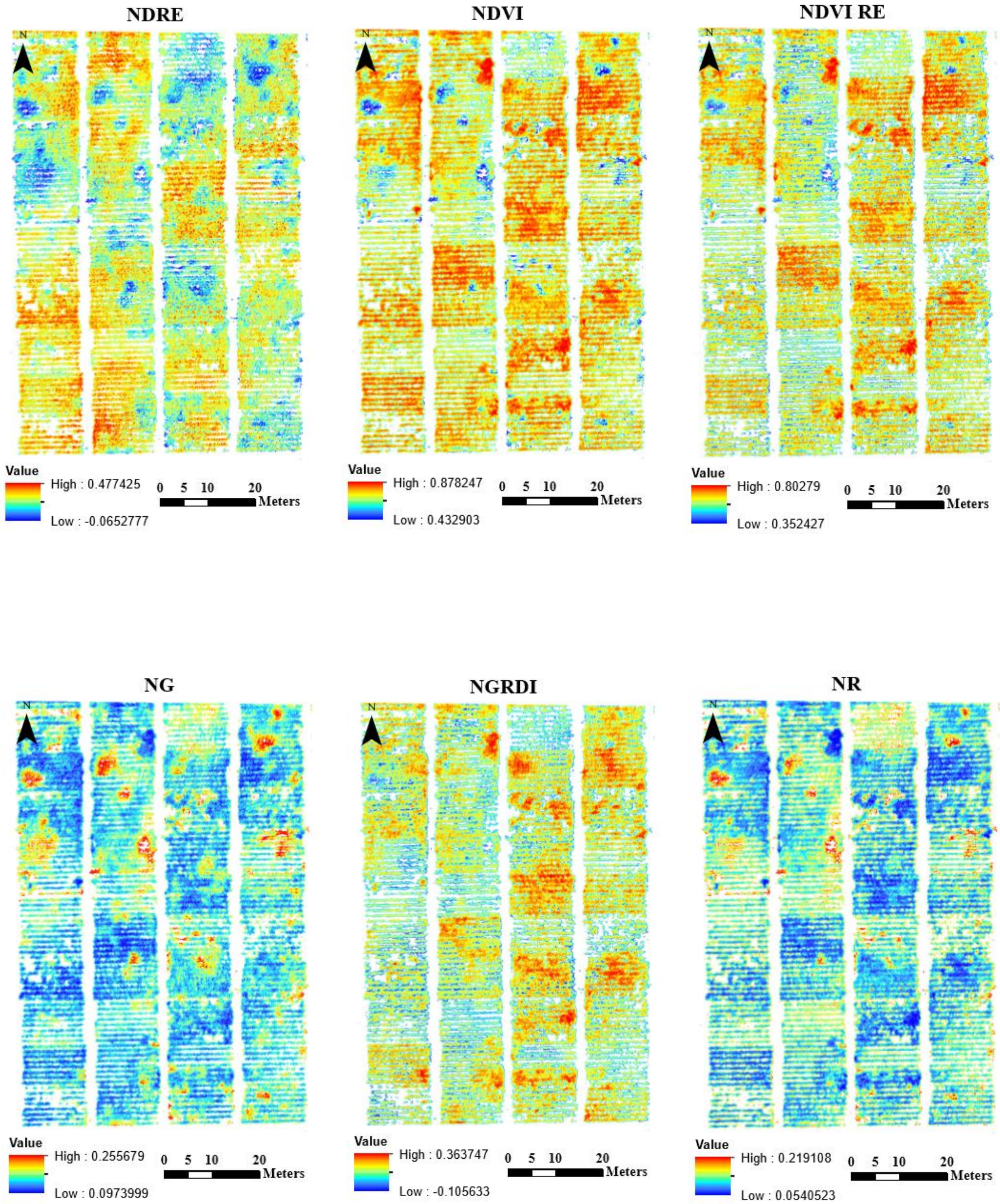
NDRE
N
Value
High : 0.477425
Low : -0.0652777
0 5 10 20
Meters
NDVI
N
Value
High : 0.878247
Low : 0.432903
0 5 10 20
Meters
NDVI RE
N
Value
High : 0.80279
Low : 0.352427
0 5 10 20
Meters
NG
N
Value
High : 0.255679
Low : 0.0973999
0 5 10 20
Meters
NGRDI
N
Value
High : 0.363747
Low : -0.105633
0 5 10 20
Meters
NR
N
Value
High : 0.219108
Low : 0.0540523
0 5 10 20
Meters

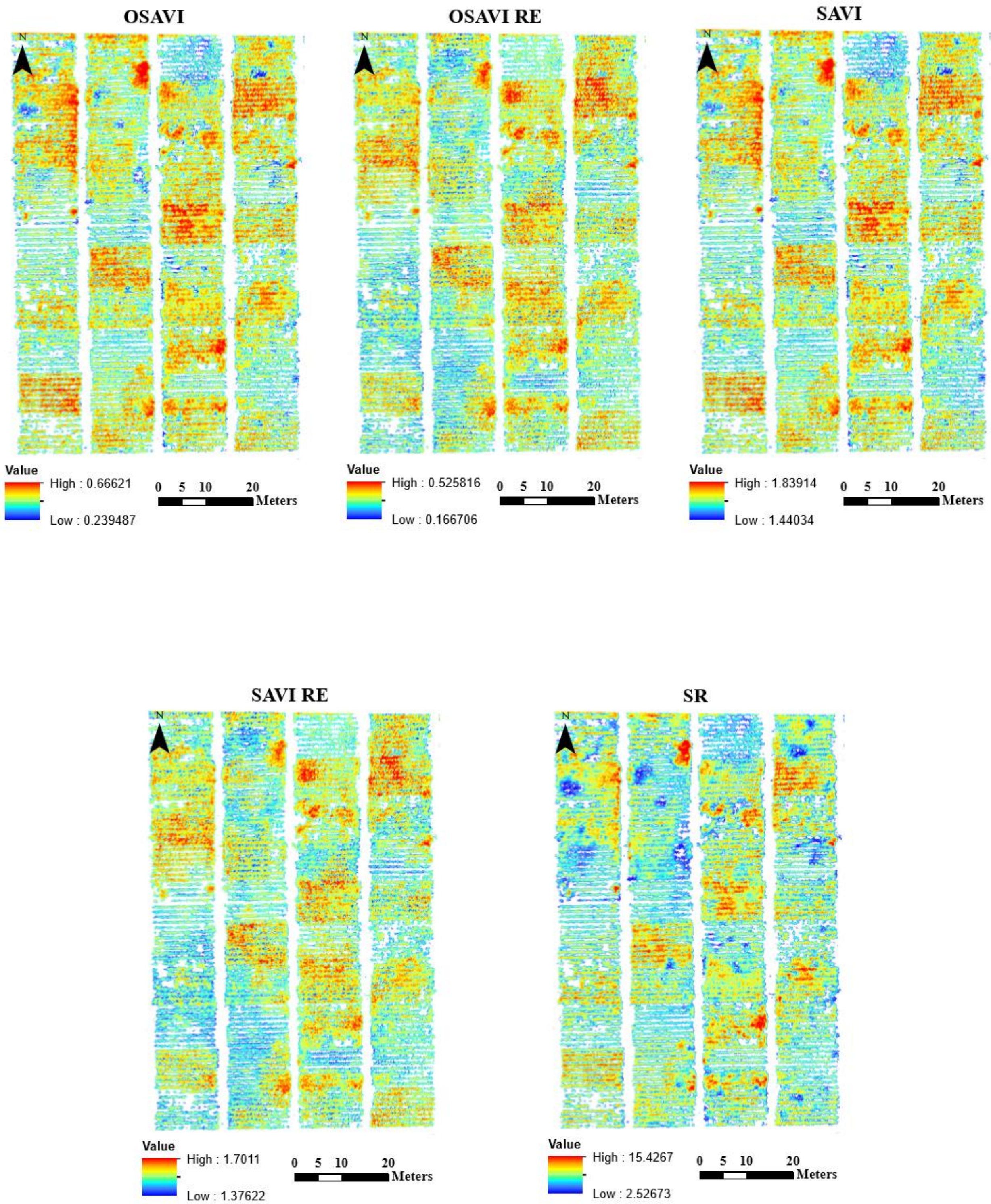
OSAVI
N
Value
High : 0.66621
Low : 0.239487
0 5 10 20
Meters
OSAVI RE
N
Value
High : 0.525816
Low : 0.166706
0 5 10 20
Meters
SAVI
N
Value
High : 1.83914
Low : 1.44034
0 5 10 20
Meters
SAVI RE
N
Value
High : 1.7011
Low : 1.37622
0 5 10 20
Meters
SR
N
Value
High : 15.4267
Low : 2.52673
0 5 10 20
Meters

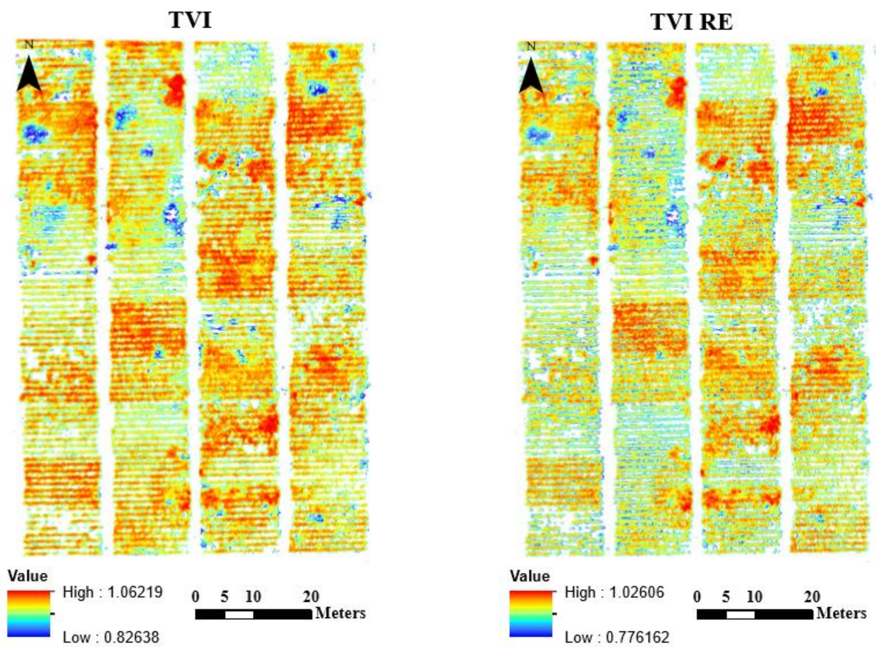

3.5 Data Extraction

In order to determine which metric performed best, each VIs ability to separate the healthy vegetation and chlorotic vegetation (separability) needed to be calculated. To do this, the data from the known, georeferenced areas needed to be extracted. Kotsiantis, et.al. (2011) states that the data used in many separability equations must exclude as many outliers as possible. The polygons that were initially built to extract iron chlorosis were too large and the edges of these went beyond the confines of pixels containing the georeferenced plants. Because of this, these polygons were deemed inapropriate for use. They were moved and fitted to exclude as many outliers as possible by carefully placing them around their respective areas to achieve the best fit for more accurate results.

In order to complete the separability calculations, the data had to be extracted from the imagery in a readable, quantitative format (most of which was completed with a series of scripts written to batch-process the data, see appendix B). As explained in section 2.3.1 areas of healthy vegetation and iron chlorosis were georeferenced and marked as to what level of chlorosis each area contained. Figure 12 shows these georeferenced areas along with the level of chlorosis within each polygons. These polygons were used to extract the pixels for each respective level of iron chlorosis and for combined iron chlorosis from the VIs computed for every flight date (although the plants were only georeferenced once and iron chlorosis was already established, the polygons were still used in earlier dates to determine if the problem can be seen early in the season). The pixels were further broken down into sections of high, medium and low iron chlorosis for better analysis of separation (script available in Appendix B.1). The process of extraction involved using these polygons to clip each VI map from every date for, both the soil-included and soil removed plants (making a total of 50 VIs for each date), and saving them into separate files. For every VI, this meant making a file for each, containing only pixels representing healthy vegetation, mild chlorosis, moderate chlorosis, severe chlorosis, and combined chlorosis, respectively (making a total of 5 files for each VI).

After each raster image was cropped for the respective datasets, each tiff file was converted to an ASCII text file (script available in Appendix B.2) in order for the pixel values to be in a useable format. Then, the pixel numbers from each text file were used in the f-Distance equation (Equation 5) (script available in Appendix B.3). Lastly, the JM distance was computed, using the median rather than the mean (script available in B.4), as validation measure to compare to the f-Distance method (Equation 4). The total amount of pixels for each file are as follows: healthy = 5152 pixels, iron chlorosis (combined) = 5963 pixels, mild chlorosis = 5152 pixels, moderate chlorosis = 5963 pixels, severe chlorosis = 5963 pixels.

3.6 Separability of Iron Chlorotic and Healthy Plants

Feature separability analysis, in this case, is the process of finding which VI best separates pixels reflecting iron chlorosis and pixels that represent green, healthy plants. There are many statistical analyses and methods of doing so for two-class features (Agapiou, Hadjimitsis and Alexakis 2012, Villa, et al. 2014, Luzum, Slatton and Shrestha 2005), but a few precautionary steps must be taken before they are used to achieve accurate results. Firstly, it is important to exclude outliers from the data. Although this in many cases can be difficult to achieve, the data samples should be chosen with the utmost care to avoid inaccuracy in the initial data. Secondly, one must take caution not to over-fit the data. Having too many samples will lead to overfitting and the results will be unintentionally separated into their respective classes, no matter the actual separability (Kotsiantis 2011).

The measure used in this study was developed by Luzum, Slatton, & Shrestha et.al. 2005 for the use of data that is not Gaussian distributed and does not rely on the data being normally distributed. This measure, called the f-Distance in this study, uses the median value, instead of the mean, because it is not as affected by outliars and for this case is given by:

$$\mathrm{d_f} = \left| \frac{\mathrm{median}(\mathrm{f^{IC}}) - \mathrm{median}(\mathrm{f^{G}}))}{\sqrt{(\mathrm{mad}(\mathrm{f^{IC}}))^2 + (\mathrm{mad}(\mathrm{f^{G}}))^2}} \right| \quad (4)$$

where

f^{IC} is the measure of pixels of iron chlorosis

f^{G} is the measure of pixels for healthy, green plants

$mad()$ is the median absolute deviation given by:

$$\mathrm{mad(x)} = \mathrm{median}|\mathrm{x} - \mathrm{median(x)}|$$

This metric provides a unit less scale for determining the separability of the median values for features f^{IC} and f^{G} (Luzum, Slatton and Shrestha 2005).

A frequently used measure of separability is called the Jeffries-Matusita (JM) Distance, which is based from the Bhattacharyya Distance, provides the likeness between two features through the amount of overlapping between the classes (Bindel, et al. 2011, Villa, et al. 2014). The JM Distance is given by the following equation:

$$\mathrm{JM} = 2(1 - \mathrm{e}^{-\mathrm{B}}) \quad (5)$$

where

$$\mathrm{B} = \frac{1}{8}(\mathrm{m_i} - \mathrm{m_j})^2 \frac{2}{\sigma_i^2 + \sigma_j^2} + \frac{1}{2}\ln\left[\frac{\sigma_i^2 + \sigma_j^2}{2\sigma_i\sigma_j}\right] \quad (6)$$

m_i and m_j are the mean values

σ_i and σ_j are the variance values

This equation produces a resulting index value from 0 to 2, with values closer to 2 being highly separable and values closer to 0 being non-separable. To add to the JM Distance, another measure was developed to measure the Percentage of Totally Separable Class Pairs (TSP):

$$\mathrm{TSP} = 100\,\frac{\mathrm{JM_N}}{\mathrm{N}} \quad (7)$$

where

JM_N are all class pairs with a calculated JM distance

N is the number of class pairs

with the resulting number being in percentage form (Michelson, Liljeberg and Pilesjo 2000). This method was used as comparison and validation for the separability method for the f-distance calculated for the date closest to the field data collection (June 28, 2017). After calculating the f-Distance and the JM distance for the data collected on June 28, 2017 it was decided that the JM distance was not appropriate for this study because too many VIs were ranked at the highest separability (a value of 2), with no way to determine which was better, and therefore the separability for the rest of the dates was decided by the f-Distance which has no set scale.

The f-Distance was then used to calculate the distance between iron chlorosis and green plants for the initial VI calculations and the soil-removed VIs to determine the top performing metrics for the entire season (all 12 flights). This was completed with the assumption that iron chlorosis was developing from the beginning of the season in the georeferenced, field control areas. The healthy and chlorotic vegetation served as the two classes in feature space. The data was normalized by the equation, whose result is a measure of the mean values, or centers of the polygons, in feature space in relation to the range of the pixels within the polygons (Luzum, Slatton and Shrestha 2005). When this was completed, the separability between areas of mild, moderate and severe iron chlorosis and healthy plants was also calculated for both regular and soil-removed VIs (all 12 flights) to reveal which metric had the highest separation at each level. This was also completed with the assumption that the 'levels' of chlorosis did not progress throughout the season (for example, maybe an area of severe iron chlorosis was mild at the beginning of the season). This provided a unitless number for every measure, allowing the metrics with the largest divergence to be ranked from best performing to worst performing VI.

CHAPTER IV: RESULTS AND DISCUSSION

4.1 VI Separability Results

As mentioned, two separability measures were tested, the JM-Distance and the f-Distance for one date, June 28, 2017. It was found that the results from the JM-Distance were not as diverse as the f-Distance, being that the scale of measure is only from 0 to 2, with 2 being highly separable. The results can be seen in Table 4 for the soil-included metrics. (the results from the soil-removed VIs can be viewed in Appendix C in comparison with the f-Distance results). Many of the resulting distances had a value of two, with no distinct way to decide which index performed better. This implied that the f-Distance was the better measure for this study, providing unique values for each metric.

4.1.1 Separability of Iron Chlorosis and Green Plants

The pixel values from the healthy vegetation and from the areas of iron chlorosis were used to produce a number representing each VI's performance with separating said pixels (see Appendix D for full results) with the f-Distance metric. For each date the separability of every soil-included VI and soil-removed VI was calculated and these values were sorted to determine the best and worst metrics. The three soil-included VIs and soil-removed VIs with the highest values (the best separability) for each date were tabulated and are displayed in Appendix D. The three-overall worst VIs were also noted and shown in Appendix D (results for the entire dataset are in Appendix F). From these, the most separable VIs were graphed and compared for every date (Figure 20).

Table 4: A comparison of the results of the JM-Distance and f-Distance computed from the June 28, 2017 data. The values for both are ranked from low to high for the soil-included metrics.

Vegetation Indices Ranked Low - High			
Vegetation Index (VI)	**Seperability Ranking (d_f)**	**Vegetation Index (VI)**	**Seperability Measure (JM Dist)**
DVI	0.0073336	DVI	0.055895
EVI2	0.16269	SR	0.091059
OSAVI RE	0.19958	EVI2	0.61302
GDVI	0.20832	ENDVI_RE	1.1497
ENDVI_RE	0.22929	OSAVI RE	1.3414
NGRDI	0.282	SAVI	1.4068
SAVI	0.30752	GDVI	1.5175
SAVI RE	0.31298	SAVI RE	1.603
GDVI RE	0.32356	NDVI_RE	1.6683
NDVI_RE	0.35987	NGRDI	1.6866
TVI RE	0.36068	OSAVI	1.9712
OSAVI	0.41307	TVI RE	1.9834
EVI2 RE	0.47051	EVI2 RE	1.9971
NR	0.76518	DVI RE	1.9997
DVI RE	0.76662	ENDVI	1.9997
ENDVI	0.76662	GDVI RE	2
TVI	0.87325	GNDVI	2
NDVI	0.87441	GNDVI_RE	2
SR	0.91543	GOSAVI	2
GOSAVI	1.0295	MTCI	2
GNDVI_RE	1.0677	ND RE	2
GNDVI	1.6975	NDVI	2
MTCI	1.7009	NG	2
ND RE	1.7079	NR	2
NG	1.8839	TVI	2

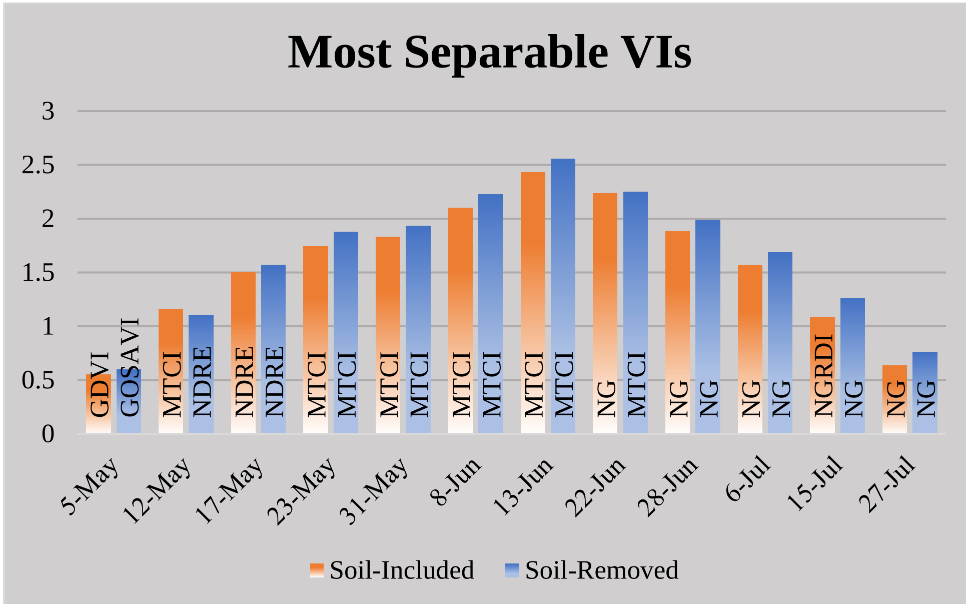

Figure 20: The most separable VI for each date for the combined chlorosis data. These Vis best separated the pixels of healthy vegetation and iron chlorosis as a whole.

After comparing the best performing VIs, it was found that, for the soil-included VIs, the best performing indices (with a couple of exceptions) were the MTCI for the first 7 weeks, and the NG for the last 5 weeks, with the MTCI performing the best overall. The GDVI, NDRE, and NGRDI did perform slightly better in some cases, but the MTCI and NG were still within the top three VIs for their ability to separate the healthy and iron chlorotic pixels.

The soil-removed VIs were more consistent, as can also be seen in Figure 20. There is a distinct transition from one VI to another starting with GOSAVI, moving to NDRE for weeks in the beginning of the season, MTCI mid-season, and lastly NG for the end of season, with the MTCI also performing the best, as with the soil-included metrics.

The poorest performing metrics for both soil-included and soil-removed metrics were a wide range of VIs with the NGRDI containing the lowest amount of separability for both (Figure 21).

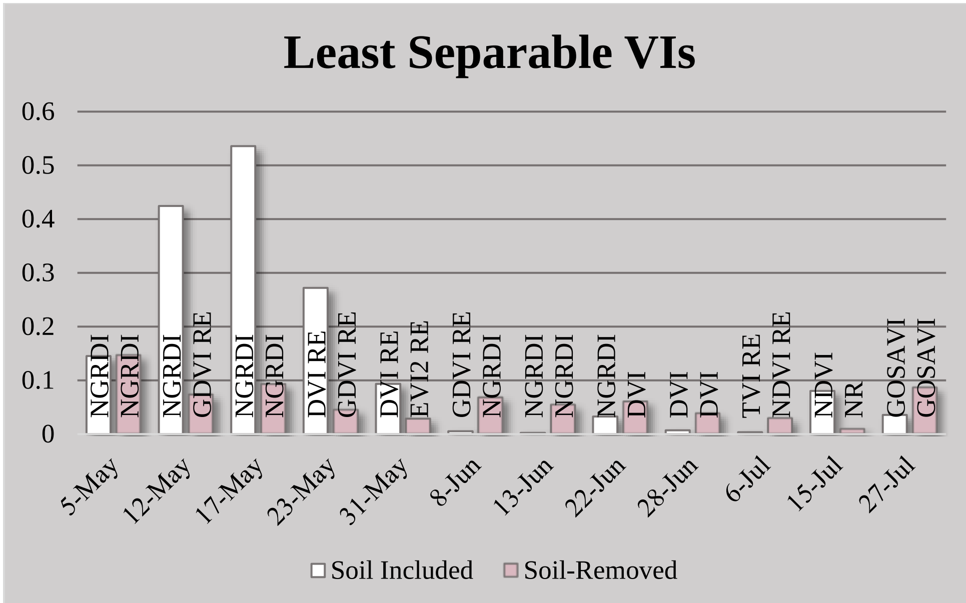

Figure 21: The least separable VI for each date for the combined chlorosis data. These VIs best separated the pixels of healthy vegetation and iron chlorosis as a whole.

Because the field data was collected later in the season (June 28, 2017) it can only be inferred that iron chlorosis was already established early in the season. The reflectance maps from the first flight (May 5, 2017) were overlaid to create a 4-band false colored image to display that iron chlorosis (plants within the red boxes) was apparent in the grain sorghum (Figure 22) at this time. However, because this cannot be proved just by observing the reflectance maps, the data was also analyzed just for the soil-removed and soil-included VIs calculated from the field data collection date (Table 5).

The results from this ranking show that the top VI for both soil-included and soil-removed metrics is the NG, with the following best metrics being the NDRE, GNDVI, and MTCI, respectively, with soil-removed metrics containing higher levels of separability. The bottom ranked VIs include the GDVI, EVI2 and DVI, with the DVI containing the least amount of separability for both types of metrics, respectively.

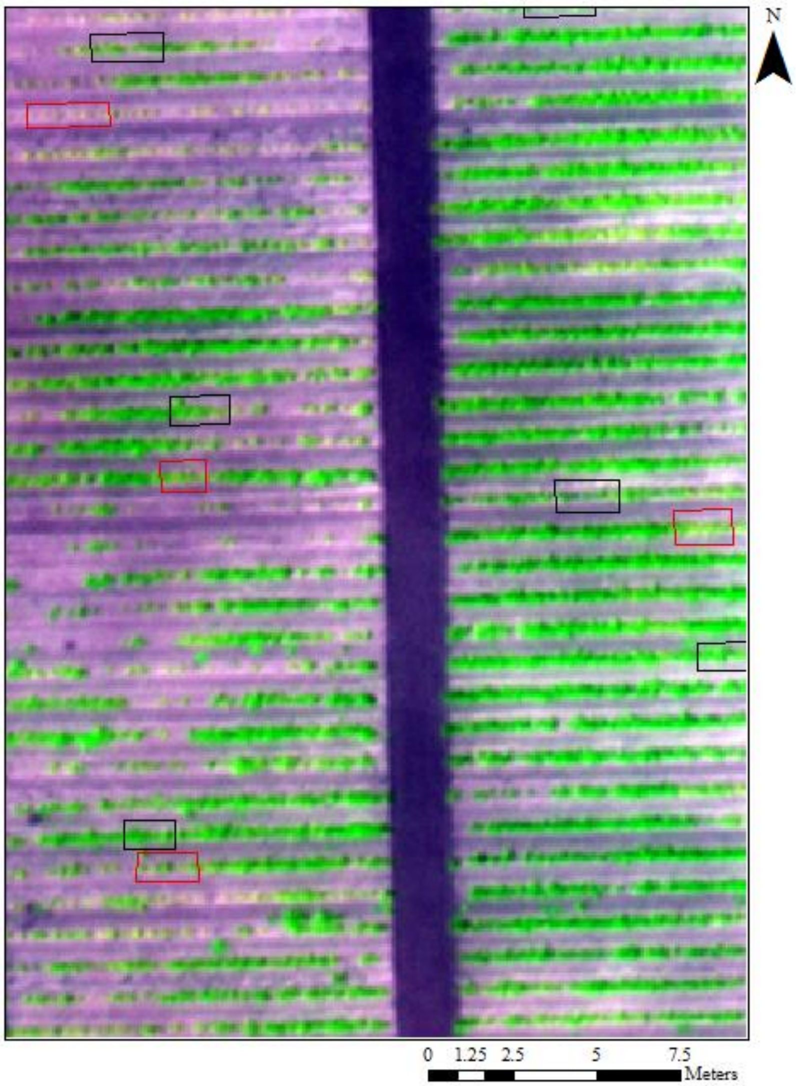

Figure 22: A display of iron chlorosis (red boxes) against healthy vegetation (black boxes) from field data collection, which took place on June 28, 2017. The background is a 4-band false colored image from multispectral data collected on May 5, 2017. It is apparent that areas of iron chlorosis were established early in the season (and is detectable via UAS), as can be viewed by the sparse, and sometimes yellowing vegetation.

Table 5: A ranking of VIs (from most separable to least) from metrics calculated using June 28, 2017 reflectance maps. The field data was also completed on this date, making this true ground/flight data.

June 28, 2017 VI Rankings			
Soil Included		**Soil Removed**	
NG	1.8839	**NG**	1.9873
NDRE	1.7079	**GNDVI**	1.8227
MTCI	1.7009	**MTCI**	1.7575
GNDVI	1.6975	**NDRE**	1.7382
GNDVI_RE	1.0677	**GNDVI_RE**	1.2086
GOSAVI	1.0295	**GOSAVI**	1.1782
SR	0.9154	**SR**	1.0099
NDVI	0.8744	**NDVI**	0.9483
TVI	0.8733	**TVI**	0.9462
DVI_RE	0.7666	**ENDVI**	0.8322
ENDVI	0.7666	**NR**	0.8277
NR	0.7652	**DVI_RE**	0.7430
EVI2_RE	0.4705	**EVI2_RE**	0.5889
OSAVI	0.4131	**OSAVI**	0.4751
TVI_RE	0.3607	**GDVI_RE**	0.4289
NDVI_RE	0.3599	**NDVI_RE**	0.3925
GDVI_RE	0.3236	**TVI_RE**	0.3924
SAVI_RE	0.3130	**SAVI_RE**	0.3837
SAVI	0.3075	**NGRDI**	0.3493
NGRDI	0.2820	**SAVI**	0.3492
ENDVI_RE	0.2293	**OSAVI_RE**	0.2610
GDVI	0.2083	**ENDVI_RE**	0.2411
OSAVI_RE	0.1996	**GDVI**	0.2021
EVI2	0.1627	**EVI2**	0.1637
DVI	0.0073	**DVI**	0.0386

4.1.2 Separability of the 'Level' of Chlorosis and Green Plants

As mentioned above, the separability of the three levels of chlorosis were computed from the georeferenced segments. The highest performing VIs overall (between the soil-included and soil-removed VIs are displayed in Figure 23. The three highest performing indices were noted and are shown Appendix E, in graduated levels (a full list of results for each stage of chlorosis is located in Appendix G). The most separable indices are the MTCI, NDRE, and NG, as in section 4.1.1, with the NG being the most separable for both soil-included and soil-removed VIs. The performance for the beginning, mid, and end season varied by level. Mild chlorosis was most separable by the NDRE at the beginning of the season, MTCI mid-season and NDRE at the end of the season. Moderate chlorosis was most separable by the NDRE at the beginning of the season, NG mid-season and NGRDI at the end of the season. Lastly, severe chlorosis was most separable by the MTCI at the beginning of the season, and NG mid to end-season. When observing the values and the VIs with the worst performance overall (for all metrics including soil-included and soil-removed), displayed in Figure 24, it seems that most of the metrics are random. There are a select few metrics that performed badly across all levels and those include, but are not limited to, the DVI_RE, SAVI_RE, TVI_RE, DVI, and NGRDI. However, the metric that was the least separable overall was the NGRDI, followed by the DVI RE.

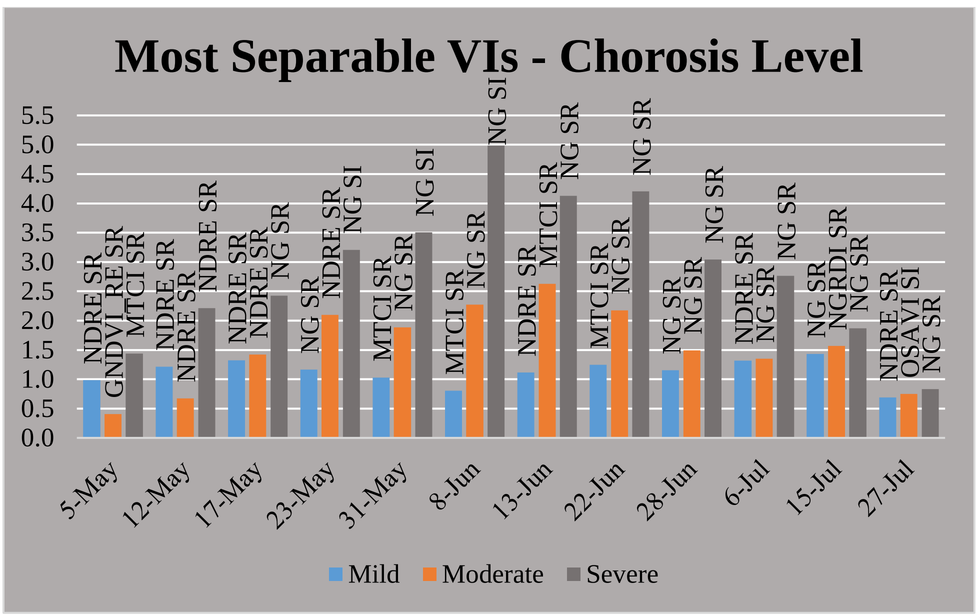

Figure 23: The most separable VIs for each level of chlorosis depicted by each date. The values shown were the highest out of all datasets (soil-included and soil-removed). Therefore, the VI with the highest separability is displayed, with 'SR' indicating a soil-removed index and 'SI' indicating a soil-included index.

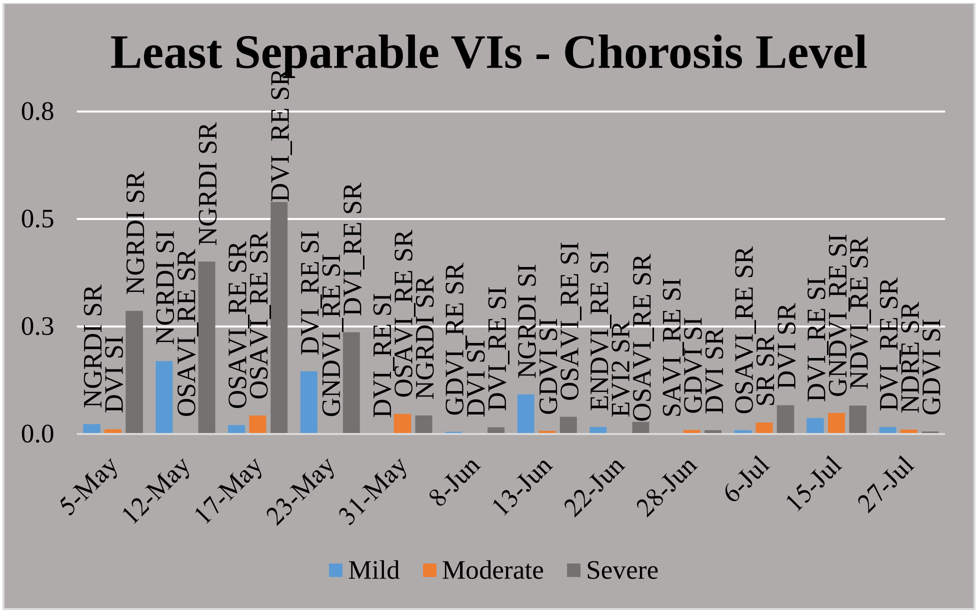

Figure 24: The least separable VIs for each level of chlorosis depicted by each date. The values shown were the lowest for all datasets (soil-included and soil-removed). Therefore, the VI with the lowest separability is displayed, with 'SR' indicating a soil-removed index and 'SI' indicating a soil-included index.

As mentioned in Section 4.1.1, the establishment of iron chlorosis in some areas could have possibly taken place later in the season. This is also true for levels of chlorosis as well. It is possible that an area of iron chlorosis was, at first, mild and as the season progressed, this area turned into moderate chlorosis. An overlay of the field data (collected June 28, 2017) is displayed on a 4-band false colored image (from the data collected on May 5, 2017), to display areas marked mild, moderate, and severe chlorosis, in Figure 25. Because the only proof that chlorosis in this field developed early in the season is that of visualization of the reflectance maps, an analysis of the most separable VIs for the flight date that took place on the same day as field collection was completed (Figure 26).

The results from this ranking show that the NG is the most separable metric for detecting mild, moderate, and severe chlorosis for both soil-included and soil-removed VIs. The least separable VI was different for all dates, with the SAVI RE and GDVI being the least separable for the soil-included metrics and the ENDVI RE, GDVI, and DVI being the least separable for the soil-included metrics, respectively.

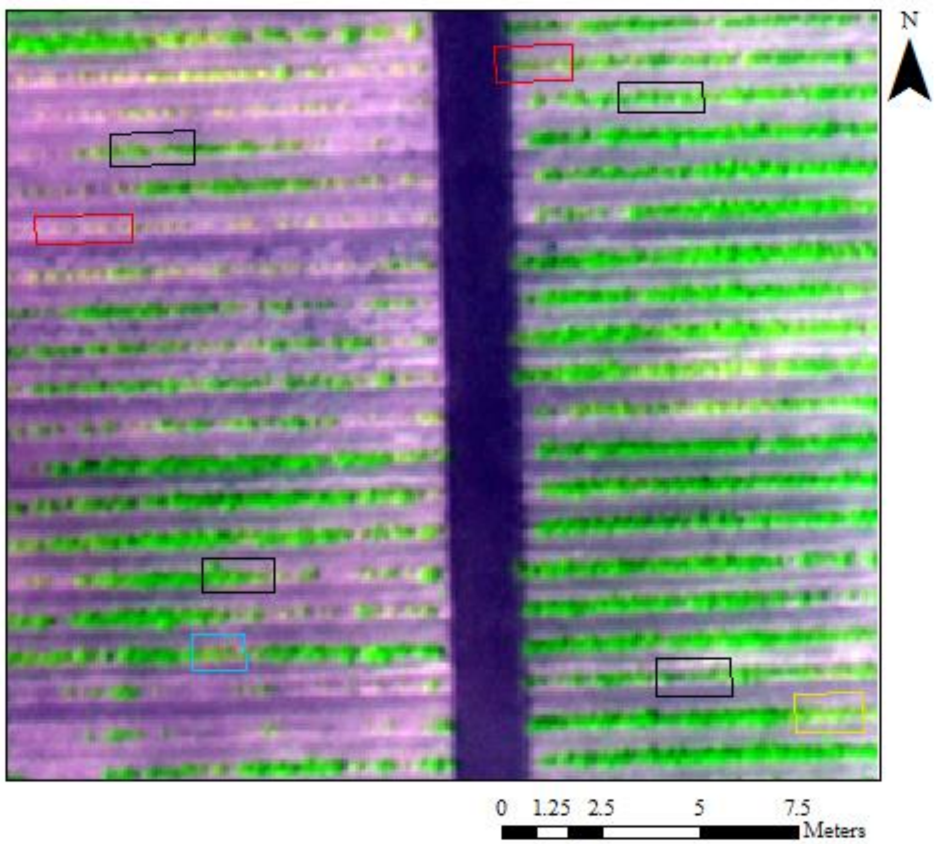

Figure 25: a display of mild (blue box), moderate (yellow box) and severe (red boxes) iron chlorosis in relation to healthy vegetation (black boxes) from field data collected on June 28, 2017. The background is a 4-band false colored image from multispectral data collected on May 5, 2017. It is apparent that chlorosis, especially mild and severe, is detectable, via UAS, from the beginning of the growing season

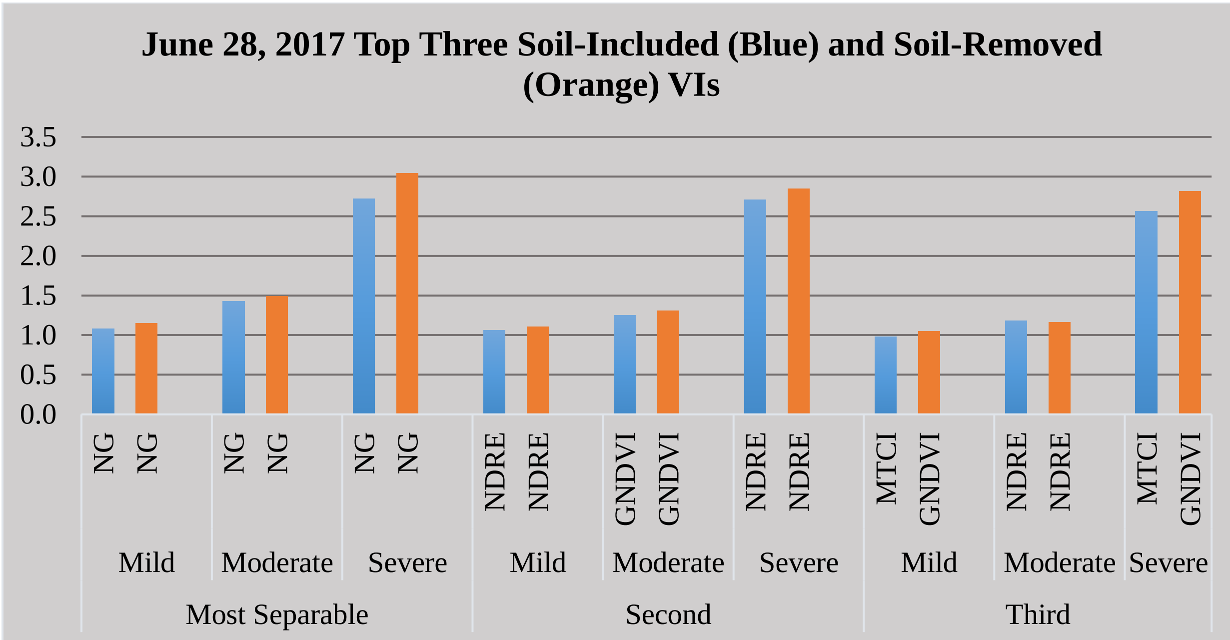

Figure 26: A display of the top three ranked VIs, by level of chlorosis, for the collection date of June 28, 2017. The soil-included VIs are displayed in blue and the soil-removed VIs in orange, respectively.

4.2 Comparison of Values for Top VIs

The results from the separability test display which VIs perform the best, the worst, and which fall somewhere in-between. The most separable VIs presented in Figures 20 and 23, which displayed the top-performing VIs for separating healthy and iron chlorosis pixels as a whole, and the most separable VIs for levels of chlorosis, respectively, were analyzed further to give a general display of the change in values over time. A prominent area of iron chlorosis was chosen to present alterations in the crop over the growing season (these areas are displayed in Appendix H as multispectral images for both the regular and soil-removed images). This segment is noted to contain severe amounts of chlorosis and is located alongside an area of green, healthy plants, making visualization of both the difference in coloration and development of the plants simpler. The mean values of iron chlorosis and green vegetation for the best performing VIs as well as the NDVI (the most well-known and widely used VI) are plotted against each other in Figure 27 and

Figure 28. These figures visually display the separation between iron chlorosis and green vegetation. They also explain trends over the season such as the growth and declination of values as the plants grow, peak, and start to die before yield is taken. It is also noticeable that as the plants reach their peak, the values between green and iron deficient separate more, explaining why at each point in the season, a different VI is dominant (one VI for each the beginning, middle, and end of the season depending on trends in the data).

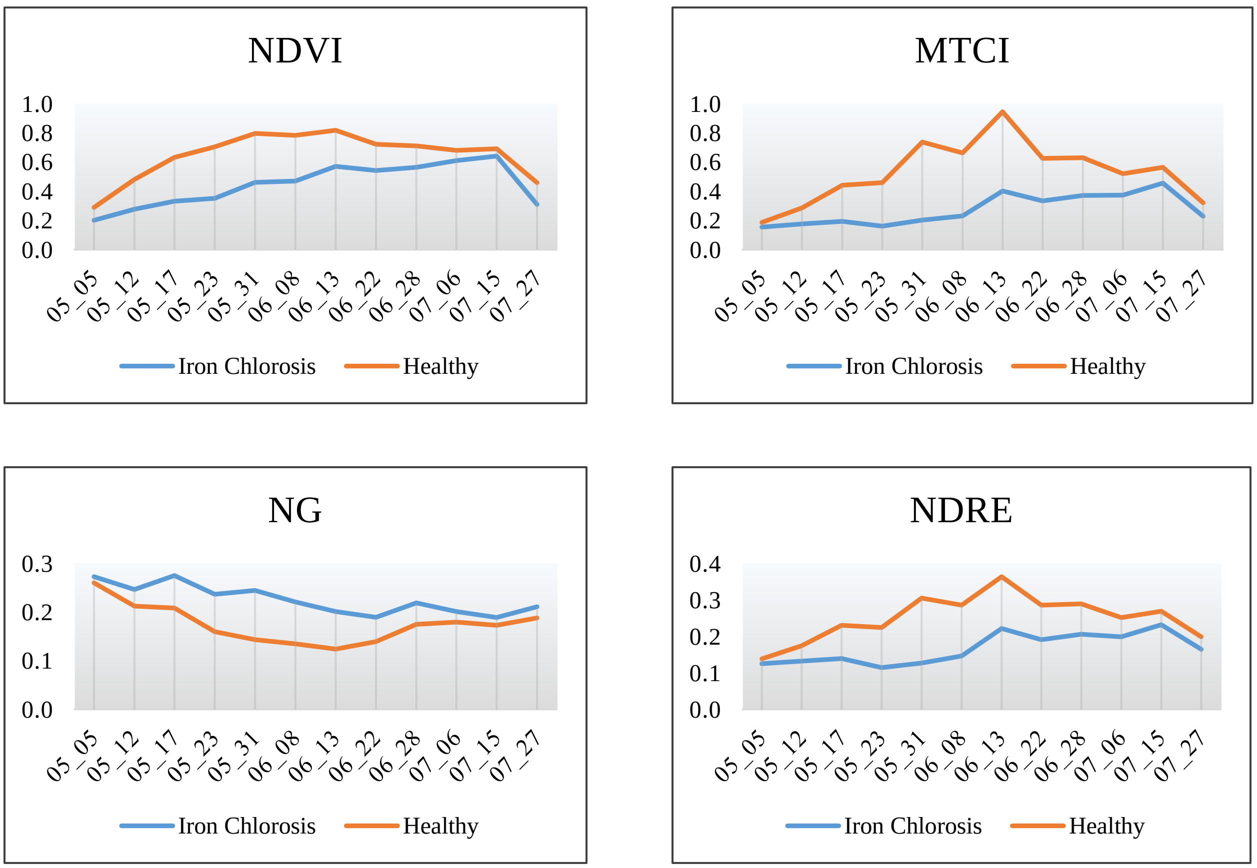

Figure 27: Mean values over the entire growing season of highest performing soil-included VIs, the MTCI, NG and NDRE, in comparison with one of the most widely known/used VIs (NDVI). The graphs visually display the amount of separability each VI has for every collection date.

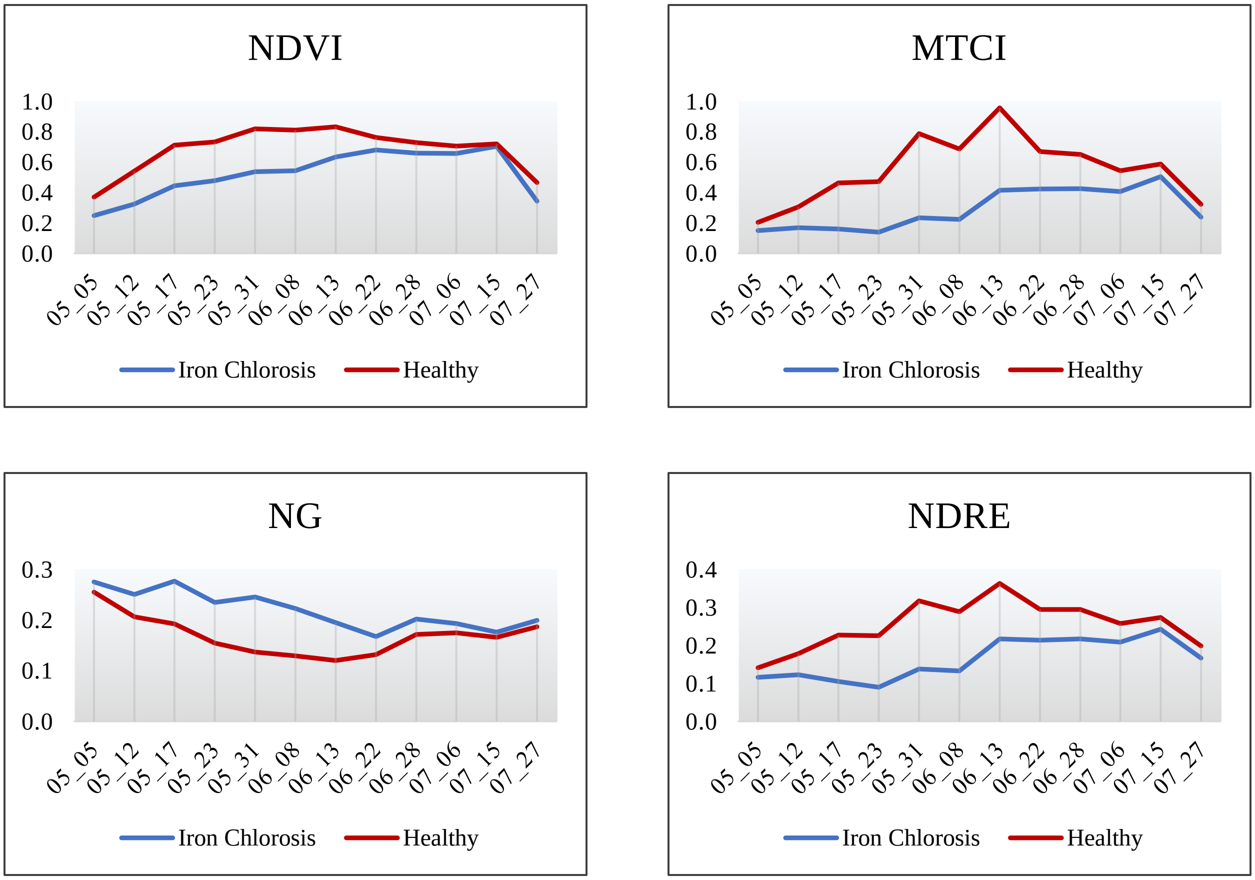

Figure 28: Mean values over the entire growing season of highest performing soil-removed VIs, the MTCI, NG and NDRE, in comparison with one of the most widely known/used VIs (NDVI). The graphs visually display the amount of separability each VI has for every collection date.

Visualizing the patterns of the values for each VI helps associate and disassociate them from stressed and healthy plants from each other and also each metric with one another. For example, the NDRE and MTCI have similar patterns, with the peaks and falls of the values. Upon further analysis of these two equations it can be seen that they are similar, with the numerator being the same and the denominator of the NDRE containing the NIR and RE bands and the MTCI having the R and RE bands. Additional thoughts on the metrics provide that the NDRE tended to perform better at the beginning and the end of the season whereas the MTCI performed better mid-season, which are seen in the median values, especially for the soil-removed VIs.

The NG, which performed very well in terms of separating the healthy and iron chlorosis values, contains larger values for pixels representing the latter and lower values for pixels representing the former, in contrast to the other VIs. This index, and the other ratio VIs all act in the same way, and therefore caution should be taken when analyzing them, as they are not the norm. This VI performed exceptionally well when determining areas of severe iron chlorosis and separated the pixels well mid-season for the mild and moderate levels. The curves for the median values seem to follow this trend, separating more mid-season yet remaining more separated than most toward the end of the season.

Graphing the trends in these values also visually displays the difference between the regular and soil-removed VIs' values. The rise and fall of the pixel values seems to be almost identical in the two, but the separation between iron chlorosis and healthy vegetation grows slightly, especially in the MTCI and NG equations. Because low values that weren't vegetation were taken away, the new low values were that of stressed vegetation. While the high values of healthy vegetation stayed the same, the gap between the values increased, making the soil-removed VIs the better alternative for determining stress due to iron chlorosis.

4.3 Yield/SPAD Data in Correlation to Top VI Values

4.3.1 Yield Data

As mentioned in section 2.3.3, the yield data from the georeferenced areas were gathered and measured (in grams) at the end of the growing season on July 19, 2017. Some plants, when the grain head was collected, contained a significant amount of midge damage resulting in a loss of data. The amount of grain lost due to midge damage was visually assessed by a group of people for a more accurate assessment. Using this valuation an estimation of grain was calculated as if the sorghum midge problem been eradicated before damage was done to the crop (this data was used to display how significant the midge damage was in some areas and was not used for correlation and regression analyses). The estimates along with an estimated error can be found in Appendix I, organized by the row in which each georeferenced area was located. The rows are named according to the location from the bottom-right corner of the crop, as is displayed in Figure 30.

The weight of the grain was used to correlate the top VI's and their associated values with the measured sections for the flight date closest to yield collection, which took place on July 15, 2017. This data, located in Figure 31 for the MTCI, Figure 32 for the NG and 33 for NDRE, respectively provides the weight of grain yielded from each area, along with the respective mean pixel value from each VI. The data shows that there are some irregularities with value and yield, resulting in odd plots, with the correlation lines not truly fitting the random-looking data. This is most likely due to the type of hybrid of each space. As can be seem from Figure 29 (a plot map of the crop), some zones of plants are healthier than others. For example, areas labeled with the number 5 are not as healthy as areas labeled with the number 1 in this map. Each of these numbers represent a different hybrid of grain sorghum. There was a total of 10 hybrids planted in the field and are named according to the crop map provided by the planters from AgriLife. Half of each hybrid plot is also marked with A or B, with A being the un-sprayed half of the plot and B being the sprayed half (spray being pesticides), as demonstrated in Figure 30. These are most likely the reasons why some areas with iron chlorosis have a greater yield than some areas of healthy plants, making this portion of data difficult to fully analyze. Hybrid types, treated and untreated plots, and especially midge damage, make yield a less important factor in the process of determining stress due to iron chlorosis.

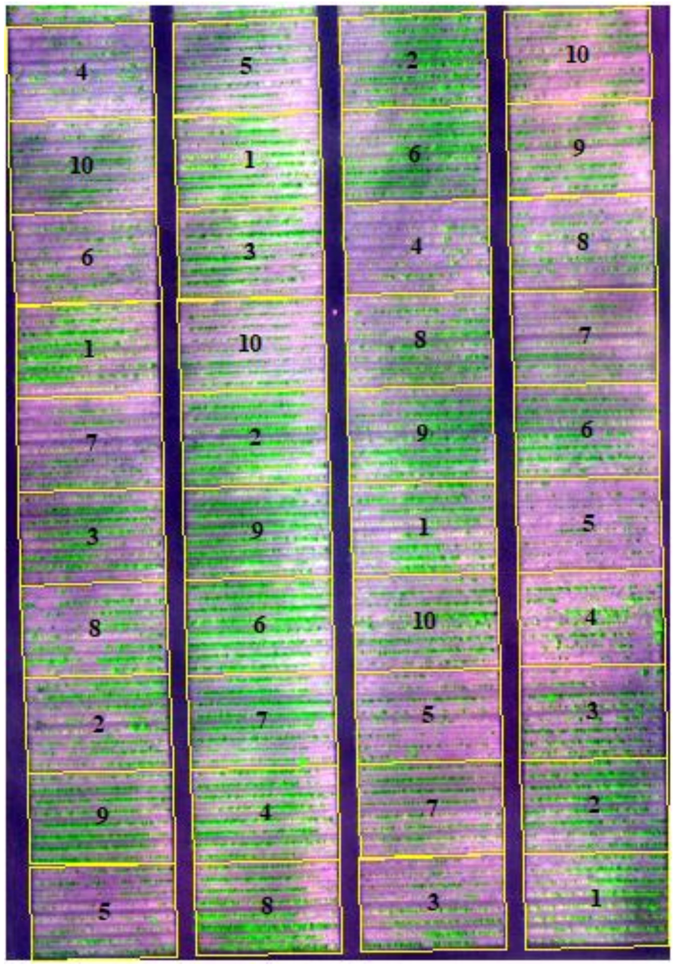

Figure 29: A general plot map of the sorghum field numbered by hybrid type (May 5, 2017). Each numbered area is a different hybrid. There are two four-row plots located inside each hybrid plot (one plot treated, the other untreated) and four hybrid plots in the entire field.

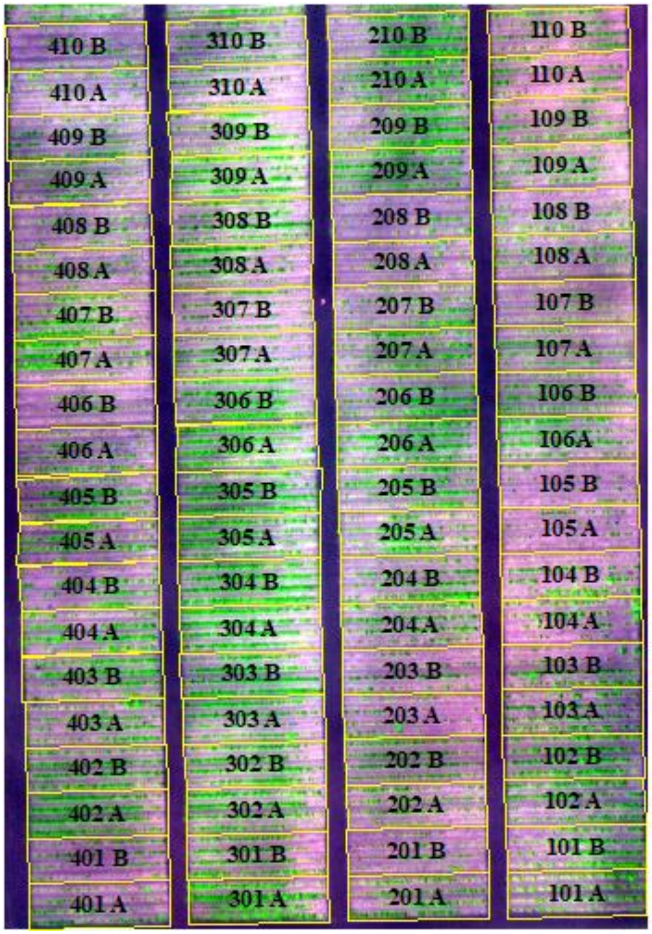

Figure 30: A field map of the sorghum plot labeled by row. (May 5, 2017) Each plot contains four rows in total, either untreated (marked with an A) or sprayed (marked with a B).

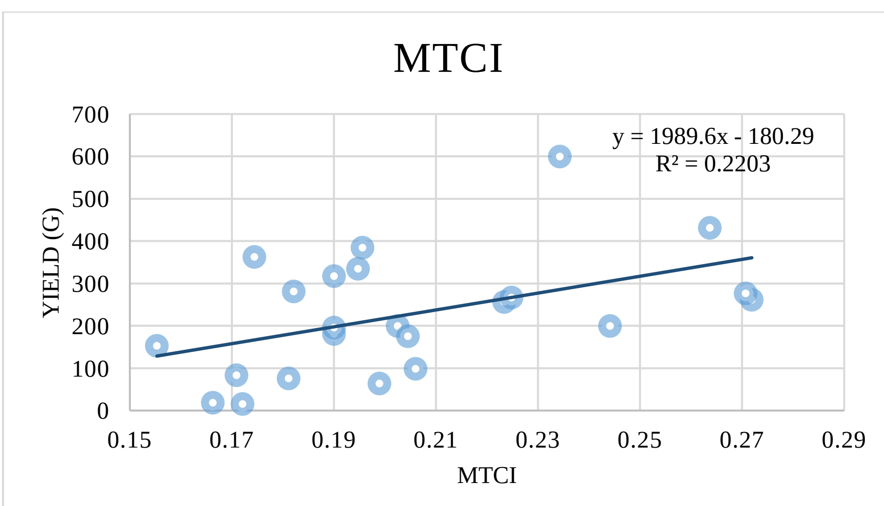

Figure 31: A plot of mean MTCI values from July 15, 2017 in relation to yield measurements (in grams). The scatterplot was fitted with a best-fit line.

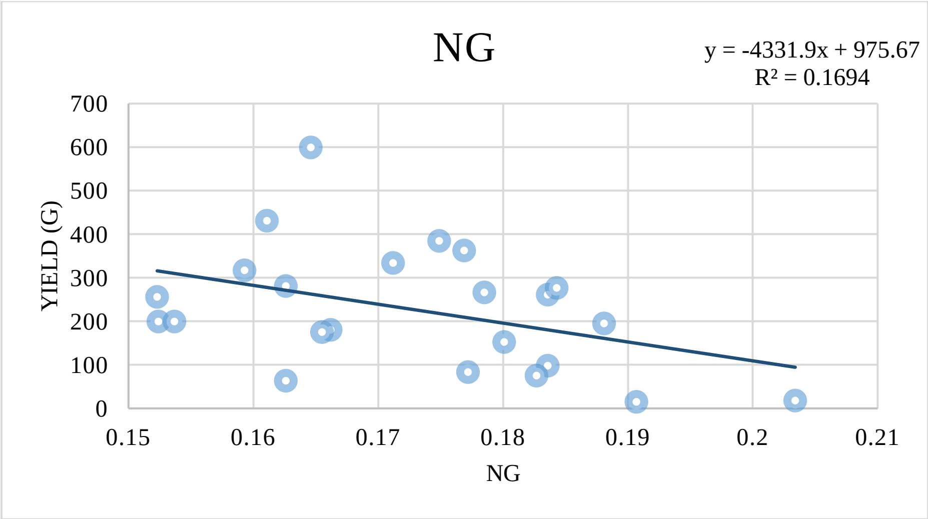

Figure 32: A plot of NG values from July 15, 2017 in relation to yield measurements (in grams). The scatterplot was fitted with a best- fit line.

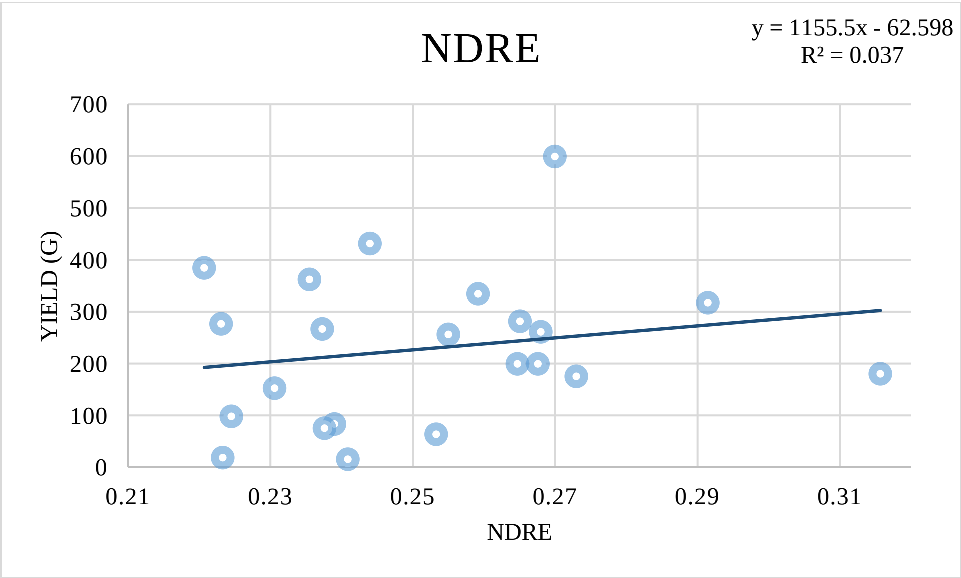

Figure 33: A plot of NDRE values from July 15, 2017 in relation to yield measurements (in grams). The scatterplot was fitted with a best- fit line.

4.3.2 SPAD Data

As mentioned in section 2.3.2, the leaves of the georeferenced plants were measured with a SPAD-502 Plus chlorophyll meter (Konica Minolta 2008). These measurements were used to correlate with the mean VI values from the most separable VIs, being the soil-removed NG, MTCI, and NDRE, respectively. These field measurements took place on the flight date July 28, 2017, from which the mean values were extracted. Figures 34, 35, and 36 show the relationship between the VIs and SPAD chlorophyll measurements. Every metric shows a positive relationship between the two data classes, displaying a connection between VI values and SPAD values. This demonstrations that areas with higher measured chlorophyll amounts (with a SPAD meter) are reflected by VI values for healthier vegetation.

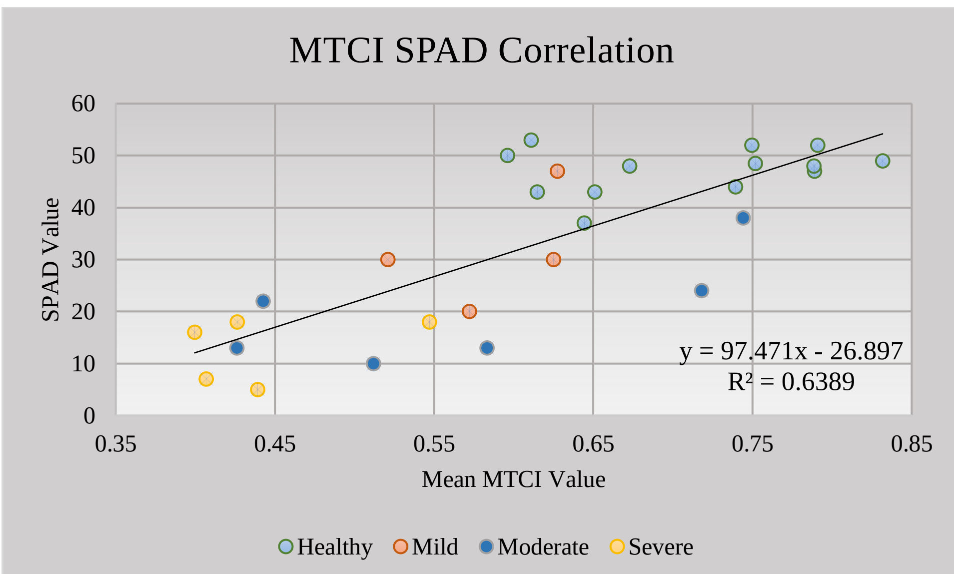

Figure 34: A correlation of the mean values from the soil-removed MTCI metric and SPAD chlorophyll measurements. All data was collected on July 28, 2017. The data shows that higher chlorophyll values correspond to higher MTCI values.

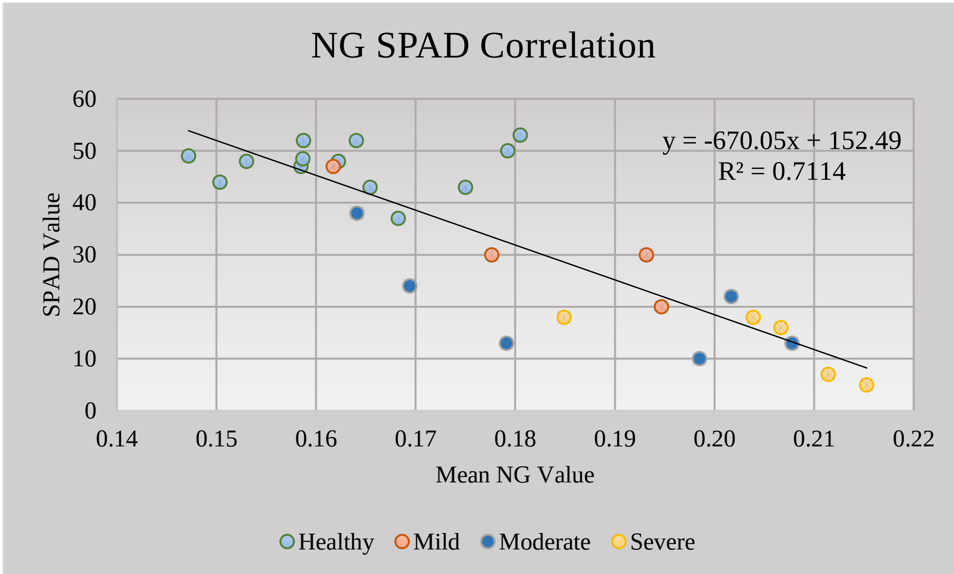

Figure 35: A correlation of the mean values from the soil-removed NG metric and SPAD chlorophyll measurements. All data was collected on July 28, 2017. The data shows that higher chlorophyll values correspond to lower NG values (lower NG values correspond to healthier vegetation).

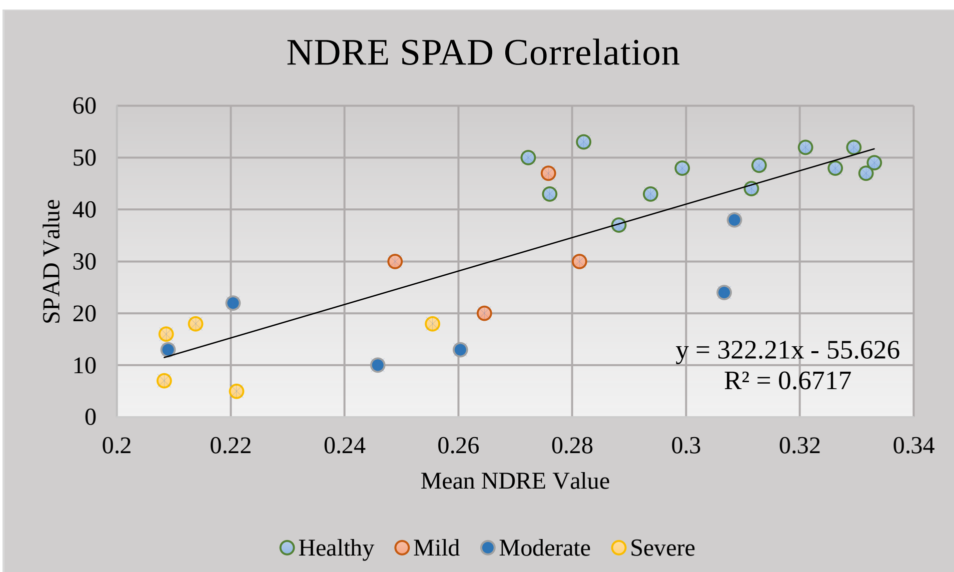

Figure 36: A correlation of the mean values from the soil-removed NDRE metric and SPAD chlorophyll measurements. All data was collected on July 28, 2017. The data shows that higher chlorophyll values correspond to higher NDRE values.

4.3.3 Yield/SPAD Correlation

The correlation between the yield measurements and the SPAD chlorophyll amounts was also observed, as shown in Figure 37. The figure is a display of measured chlorophyll amounts and yield weight. Although this is a correlation between two forms of field collected data, it is a display of true measurements.

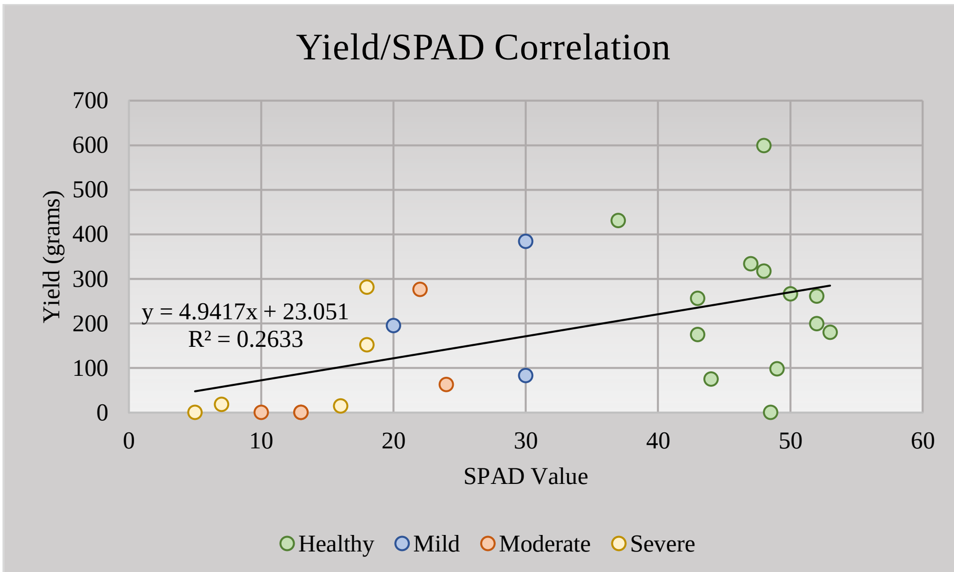

Figure 37: A correlation between yield measurements and SPAD chlorophyll data. The data shows that higher chlorophyll amounts generally correspond to higher yields.

4.4 Discussion

4.4.1 VI Rankings of ‘Combined Chlorosis’ Separation

The separability of healthy vegetation and combined iron chlorosis was calculated, finding that the top VIs were the NDRE early-season, MTCI mid-season, and NG end-season, with the MTCI being at the top for most dates. The results from the soil-removed separability also helped verify this, providing a more distinct grouping of these VIs. However, the highest performing metrics were mostly consistent between the soil-included and soil-removed VIs, although the level of separability between the two was generally higher in the soil-removed metrics. It should also be mentioned that, in cases where the NDRE performed the best, the MTCI ranked second in terms of separability, making it almost just as effective, thus simplifying the findings.

This provides a unique solution, as the most widely used metric is the NDVI. For example, the NDVI metric was utilized by Vina, et al. (2011) to monitor a sunflower crop, and by Alves, Macrae and Koch (2015) to determine stress due to chlorophyll reductions in a soybean crop. Mulla, et al. (2013) and Gago, et al. (2015) both discuss using soil-adjusted VIs, such as the SAVI metric to detect stress in sparse vegetation. However, the NDVI has been bested by other metrics in previous studies, such as the NRGDI, SAVI, NDVI RE, and others (Kross, et al. 2014; Rondeaux, Steven and Baret 1996). Mutanga and Skidmore, et.al (2004) had high precision measures with the NDVI RE, in comparison with the NDVI. Even the SAVI, mentioned above, was expanded upon to make the OSAVI, that according to (Rondeaux, Steven and Baret, et al. (1996) is useful for vegetation analysis. The NDVI, SAVI, OSAVI and other metrics were not found to be as useful for detecting iron chlorosis in grain sorghum, conversely. The results from the separability rankings displayed a distinctive set of results, for both metrics with higher divergence and lower separation.

The poorest performing metrics contained a wide assortment of VIs, which included both regular and soil adjusted indices of both peer reviewed paper-proven formulas and red-edge substitution formulas. The separability values for these metrics are very low, and in many cases close to 0, especially at the beginning and the end of the season, where values for even the best performing metrics were low.

The DVI and some other soil-adjusted indices also performed poorly for both soil-included and soil-removed, but the soil-removed had more soil-adjusted indices listed as the least separable.

This is to be expected since there was no soil in this imagery to correct, indicating that some soil-adjusted indices, such as the SAVI and OSAVI did not perform poorly for the soil-included data. The DVI and DVI RE, as another example were amongst the lowest separable VIs for both soil-included and soil-removed, making them amongst the lowest performing overall.

Although the field data for iron chlorosis was collected towards the end of the season, it is implied in the results above that the deficiency was present during the entire season. This cannot be proven through field data, but it can be implied through multispectral data, as pictured in Figure 22. It is apparent that the iron chlorotic areas contain sparse vegetation that, in some areas, is already beginning to yellow. This gives an idea of how chlorosis progresses, from the beginning of the season, for some areas.

The Resulting VIs from just the data collected on June 28, 2017 also reflect the findings from the other dates, with the NG being the most separable. The other top VI's included the GNDVI, NDRE, and MTCI for both soil-removed and soil-included metrics. The amount of separability was higher for the soil-removed VIs, as was found for all the datasets.

4.4.2 VI Rankings by Level of Chlorosis Separation

Upon observing the values and metrics that performed the best for each level, it is apparent that the same metrics tended to do well for both the soil-included and soil-removed VIs. It can also be inferred that as the levels of iron chlorosis graduate, the leading VIs changed, and the f-Distance values increased. This demonstrates that areas of higher levels of chlorosis have a greater separability from green plants and gives an improved understanding as to which VIs perform better at each level. For mild chlorosis the NDRE was in the list of top three metrics most of the season, for moderate chlorosis the performance is split between the NDRE, NG and NGRDI, respectively, and for severe chlorosis the NG is dominant for almost the entire growing season (results can be seen in Figure 23 for the top VI for each level overall. See Appendix D for the top three ranking VIs for each level of soil-included and soil-removed VIs). There is a transition from one metric to another through the levels, which evidences that each stage of chlorosis is identifiable by different VIs.

The formulas that did seem to work well for detecting iron chlorosis for combined iron chlorosis and for all levels, however, were those which used both the NIR and RE bands. Both the MTCI and NDRE (which use both NIR and RE) equations out-performed metrics using only NIR or only RE. The G band also performed better than expected in the NG, NGRDI, and GNDVI equations. The NG, the most separable VI across all datasets, was one of the three ratio VIs tested, had better results than the almost-identical NR metric, although the only difference between the two is the use of the G and R bands. The GNDVI also uses the G and R bands to create a ratio, much like the NDVI equation, substituting G for NIR and this, too was among one of the highest ranked metrics.

As mentioned in section 4.1.2, the worst performing VIs were also analyzed for the three levels of iron chlorosis to determine which of the metrics did not perform as expected. These are displayed in Figure 24 and display which VI was the least separable across all VIs tested for both soil-included and soil-removed indices. It was found that the least separable VI overall was the NGRDI. It is also apparent that many of the metrics changed to include the RE band, instead of NIR, did not work as well as was originally anticipated. This is interesting considering that fact that the NDRE and MTCI both use the RE band.

These results show that the NIR and RE bands, in conjunction with one another, seem to perform better than these respective bands alone. Although the RE band is said to be extremely useful when analyzing vegetation (Hansen and Schjoerring 2003), this band did not perform as well as initially thought. There did not seem to be a significant change in the amounts of chlorophyll detected with this band, making the performance of this band mediocre when used alone in this study. However, the scattering of IR wavelengths captured by the NIR and the detection of chlorophyll of the RE band together created good results.

The separability results also hint that R and G bands also appear to work well in contrast to one another. This could be due to the fact, as stated in the introduction, that the absorption of R wavelengths and the reflection of G wavelengths by greener vegetation and the reflection of R wavelengths and absorption of G wavelengths by stressed vegetation create a well-balanced contrast to determine areas of iron chlorosis (Sripada, et al. 2008).

As mentioned above, the NDVI did not achieve results as well as predicted. As mentioned, this metric is one of the most commonly used VIs for determining plant stress. Also, the SAVI, which was derived from the NDVI equation to compensate for soil effects (and is also one of the more popular soil-adjusted indices) did not perform well and, in some cases, was amongst even the worst metrics for both the soil-included and soil-removed metrics (it is to be expected from soil-removed metrics to perform poorly with soil adjusted VIs). These findings are surprising, considering the popularity of the SAVI, hinting that this VI is not the best for determining iron chlorosis.

As was discussed in Section 4.1.2, the 'levels' of iron chlorosis may have changed throughout the season. An area of moderate chlorosis could have been mild at the beginning of the season. From Figure 25, it is apparent that the different levels of chlorosis can be seen starting to form, giving a visual confirmation that some levels of chlorosis did stay consistent throughout the growing season. The most separable VIs are also consistent with the popular findings of the dataset as a whole. The NG was the most separable metric for both soil-included and soil-removed VIs for all levels of chlorosis, with the separation increasing as chlorosis intensifies, respectively.

4.4.3 The Separability for all Groups

The most separable VIs were unexpected, as they are not the most popular or widely used indices. The RE band, which is said to have better estimates of chlorophyll amounts in a plant did not perform well by itself when replacing the NIR band, but did work well in conjunction with it. The G band also out-performed the R band in many cases, making the GNDVI more separable than the well-known NDVI and also making the NG become one of the top-performing VIs, possibly due to its reflectivity in healthy vegetation and absorption in stressed plants.

While some VIs had higher separability values in specific cases, such as for only mild chlorosis, the MTCI, NDRE, and NG performed the best for all. The NDRE and NG both did well in the beginning of the season to determine areas of iron chlorosis. The NDRE performed better for mild and moderate levels, whereas the NG did the best when detecting severe chlorosis and the MTCI performed well for the group as a whole (Results displayed in Figure 23 with the top three ranking VIs located in Appendix E). However, the NG overall was the most separable VI for most cases, making it the top-ranking index. Some VIs separated the two pixel classes better at the end of the season, such as the OSAVI and DVI. While the mid to end of season data is important, the early season information is more useful. It is early in the season, while the plants are young and still have growing potential, that they should be treated, making the end of season data less important in terms of this study.

Every VI performed poorly at separating the two classes in the very early and end parts of the season. As the plants continued to grow, the distinction between iron chlorosis and healthy vegetation began to grow, even by the second or third week, which should give ample time for treatment. The distinction between the two populations was especially clear in the areas of severe iron chlorosis, where the plants contain the most need for treatment. The separation for severe chlorosis was still distinct enough to show stress in the early-season with the NG, further implying that this index performed well, especially for this level of stress.

4.4.4 Yield/SPAD Measurements in Relation to Top Ranking VIs

While the yield data was not a leading factor to determine areas of iron chlorosis, they did highlight a few pieces of information about the crop. One important finding to note is that the most separable metric, the NG, did not have many outlying points in Figure 30, displaying lower yield values for higher NG values. This is an indication that healthier plants do contain a higher yield (the NG is one of the few VIs in which a lower VI value indicates healthier vegetation).

Although some areas of iron chlorosis contained a higher yield amount than those of the healthy plants, it is most likely because of the hybrid type that this is so. Therefore, by observation of the hybrid map, areas of healthier plants can be differentiated using sUAS-derived multispectral data, and it is also apparent that some hybrids fare better than others. This can be linked to the rise and fall of values (the range of values) of healthy vegetation and provide an explanation for why this wider range occurred in the data.

The sUAS-acquired multispectral imagery can be used to detect areas of healthier vegetation, which can be linked to higher yield values. Some areas or sparse vegetation, although healthy, did not have high yield counts (yield values can be found in Appendix I and can be correlated to the general plot map in Figure 29).

The correlation between SPAD estimated chlorophyll amounts and VI values contained an evident relationship. As the chlorophyll amounts increased, so did the VI values (apart from the NG, in which lower values are related to higher chlorophyll amounts and healthier vegetation).

The correspondence between the NG and chlorophyll amounts also seemed to contain a better 'grouping' of data, rather than a widespread trend.

Yield estimates and SPAD chlorophyll data was also correlated, giving a positive relationship. However, the link between the two classes was not as linear, suggesting that some areas of healthy vegetation do not have high yields. This, as mentioned before, is probably due to hybrid type.

CHAPTER V: CONCLUSION AND FUTURE WORK

5.1 Conclusion

This project used a sUAS to collect 4-band multispectral imagery to assess their utility for extracting VIs to discover and monitor iron chlorosis in grain sorghum. The 4-band multispectral imagery was processed using SfM image processing to derive reflectance maps that could subsequently be used to calculate a series of VIs. These VIs were then were evaluated on their ability to separate healthy vegetation and iron chlorosis as a whole, and at levels of mild, moderate and severe, based on their separability rankings. The VIs that ranked the highest have the potential to predict oncoming areas of iron chlorosis, or iron chlorosis in its early stages.

A series of ground truth data was collected to pre-determine strained areas which included georeferenced iron chlorotic plants, assessing the amount of chlorosis, using a SPAD chlorophyll meter to measure the relative amount of chlorophyll, and collecting the yield. Over the course of the growing season a series of weekly flights were performed with an eBee SQ fixed-wing drone mounted with a Parrot Sequoia multispectral sensor. The imagery (as mentioned above) was processed with SfM photogrammetry to create multispectral reflectance maps in the R, RE, NIR and G bands.

The multispectral data was then used to calculate a total of 25 VIs, gathered from multiple sources that validated their use in detecting plant stress from factors relating to iron chlorosis. For further analysis of these indices, the soil was removed from the imagery for one date (May 17, 2017) using a maximum likelihood supervised classification and a probabilistic classifier to determine which method provided more ideal results. When a method was chosen (maximum likelihood classification), the soil was removed from the reflectance maps for all dates. From these, another set of soil-removed VIs were calculated, mostly independent of the background factors that caused low values. The VIs were delineated (using the field collected GPS observations) to extract pixels representing two classes, iron chlorosis and healthy vegetation.

The separability between these areas was calculated using two methods, the JM-Distance and the f-Distance to determine which method produced superior results, for data collected on June 28, 2017. When the more appropriate metric for this study was found (the f-Distance), it was used to rank class separability for each VI. The f-Distance was also computed for areas of mild, moderate, and severe levels of chlorosis to determine which VI performed the best at each.

It was found that the most separable VIs across all dates for both soil-included and soil-removed VIs were the MTCI, NDRE, and NG, with the NG being the most separable for most dates (including the date of field collection). The separability values from the soil-removed VIs were also generally higher than the soil-included, implying that removing soil from the reflectance maps before calculating VIs is useful, and provides better results.

The VI results also were used to relate the yield and SPAD chlorophyll measurements. There was no specific correlation that could be found between the VI values and the weight of the grain due to the many different hybrids planted in the field. The 4-band multispectral reflectance maps and VI maps showed that some hybrids are generally healthier than others, skewing the data. A relationship between yield and SPAD measurements was found, although some plants with higher chlorophyll readings had lower yields. These also probably relate to hybrid type. There was a correlation between chlorophyll measurements and VI values, relating low chlorophyll measurements to high levels of chlorosis and vice versa.

In conclusion, sUAS-derived multispectral imaging, created from SfM photogrammetry, is useful when determining plant stress due to iron chlorosis in grain sorghum crops. The multispectral image bands could calculate a plethora of VIs, which were able to detect iron chlorosis, the best overall VI for this being the NG. This study was successful in demonstrating the uses of sUAS's for the detection of iron chlorosis, monitoring areas of crop stress, and assessing areas of crop health.

5.2 Future Work

The sUAS-acquired 4-band multispectral imagery were utilized to compute 25 VIs in this study. Some of those VIs were modified to include the bands collected by the Sequoia sensor, and some were modified to exclude the blue (B) band, which was not available. This band is not one of the more common to be found in VIs formulated to monitor vegetation, but it can be used, as in a study conducted by Gitelson, et al. 2002, in which a VI utilized the R, G, and B bands. A sensor with this band could be useful for both calculating VIs and also for using Canopeo (Patrignani and Ochsner 2015) for extracting canopy cover.

The VIs could further be utilised to predict yield in grain sorghum over an entire crop or for different hybrids. One problem with this study was correlating the VIs with the yield data. If more yield counts were taken, they could potentially have found a correlation with yield counts.

One main downfall of this study was the lack of ground truth data. While the UAS imagery was collected once a week to privide sufficient data, the measurements for iron chlorosis took place on only two days (one day for georeferencing one for SPAD measurements and assessment of chlorosis levels. Data collection should have taken place for the entire growing season to see how chlorosis progressed and at what stage it is visible to the eye, for field measurements.

As mentioned, this study used UAS-derived imagery to compute VIs, with consistent results. With the top VIs, a supervised machine lerarning algorithm could be built, with these VIs used as training data. This algorithm could be tested on the 4-band false colored multispectral reflectance maps to determine how well each VI can detect iron chlorosis, if they can detect different levels of chlorosis, and how early the chlorosis can be detected. The ultimate goal of this study in the future is to create an automatic classifier built for UAS-acquired multispectral imagery to detect iron chlorosis, by level, early in the season, with enough time for farmers to treat it and produce a yield from the affected plants.

REFERENCES

Abadia, Javier, Saul Vazquez, Ruben Rellan-Alvarez, Hamdi El-Jendoubi, Anunciacion Abadia, Ana Alvarez-Fernandez, and Ana Flor Lopez-Millan. 2011. "Towards a knowledge-based correction of iron chlorosis." *Plant Physiology and Biochemistry,* Rebruary 3: 471-482.

Agapiou, Athos, Diofantos G. Hadjimitsis, and Dimitrios D. Alexakis. 2012. "Evaluation of Broadband and Narrowband Vegetation Indices for the Identification of Archaeological Crop Marks." *Remote Sensing 4,* December 7: 3892-3919.

Alves, Tavvs M., Ian V. Macrae, and Robert L. Koch. 2015. "Soybean Aphid (Hemiptera: Aphididae) Affects Soybean Spectral Reflectance." *Journal of Economic Ecnomology*, 2655-2664.

Apan, Armando, Alex Held, Stuart Phinn, and John Markley. 2003. "Formulation and assessment of narrow-band vegetation indices from EO-1 hyperion imagery for discriminating sugarcane disease." *Spatial Sciences Institute Biennial Conferences.* Canberra, Austrailia: Spatial Knowledge Without Boundaries.

Bakker, Maarten, and Stuart N. Lane. 2017. "Archival photogrammetric analysis of river-floodplain systems using Structure from Motion (SfM) methods." *Earth Surface Processes and Landforms,* 1274-1286.

Baluja, Javier, Diago P. Maria, Pedro Balda, Roberto Zorer, Franco Meggio, Fermin Morales, and Javier Tardaguila. 2012. "Assessment of vineyard water status variability by thermal and multispectral imagery using an unmanned aerial vehicle (UAV)." *Irrigation Science 30*, August 21: 511-522.

Behboudian, M.H., A.H. Pickering, and E. Dayan. 2003. "NUTRITION: Deficiency Diseases, Principles." In *Encyclopedia of Applied Plant Sciences*, by Brian Thomas, Brian G Murral and Denis J Murphy, 642-649. Waltham: Elsevier Ltd.

Berni, Jose A. J., Pablo J. Zarco-Tejada, Lola Suarez, and Elias Fereras. 2009. "Thermal and narrowband Multispectral Remote Sensing for Vegetation Monitoring From an Unmanned Aerial Vehicle." *IEEE Transactions of Geoscience and Remote Sensing 47(3),* March: 722-738.

Bhandari, A. K., A. Kumar, and G. K. Singh. 2012. "Feature Extraction using Normalized Difference Vegetation Index (NDVI): a Case Study of Jabalpur City." *Procedia Technology 6,* 612-621.

Bindel, Marcus, Soren Hese, Christian Berger, and Christiane Schmullius. 2011. "Feature selection from high resolution remote sensing data for biotope mapping vol. XXXVIII-4/W19." *ISPRS.* Hannover, Germanmy.

Cannon, Gus. 2016. *TxDOT Survey Manual.* April 01. http://onlinemanuals.txdot.gov/txdotmanuals/ess/gps_surveying.htm.

Clevers, J.G.P.W., and A.A. Gitelson. 2013. "Remote estimation of crop and grass chlorophyll and nitrogen content using red-edge bands on Sentinel-2 and -3." *International Journal of Applied Earth Observation and Geoinformation 23* 344-353.

Cronholm, Greg, Allen Knutson, Roy Parker, and Bonnie Pendleton. 2007. *Managing Insect and Mite Pests of Texas Sorghum.* Corpus Christi, Tx: Texas A&M AgriLife Extension.

Deng, Xinyang, Qi Liu, Yong Deng, and Sankaran Mahadevan. 2016. "An improved method to construct basic probability assignment based on the confusion matrix for classification problem." *Information Sciences 340-341*, May 1: 250-261.

Duan, T., S.C. Chapman, Y. Guo, and B. Zheng. 2017. "Dynamic monitoring of NDVI in wheat agronomy and breeding trials using an unmanned aerial vehicle." *Field Crops Research*, May 31: 71-80.

Gago, J., C. Douthe, R.E. Coopman, P.P. Gallego, M. Ribas-Carbo, J. Flexas, J. Escalona, and H. Medrano. 2015. "UAVs challenge to assess water stress for sustainable agriculture." *Agricultural Water Management 153*, Februrary 19: 9-19.

Gitelson, Anatoly A., Yoram J. Kaufman, Robert Stark, and Don Rundquist. 2002. "Novel algorithms for remote estimation of vegetation fraction." *Remote Sensing of Environment 80* 76-87.

Guyot, Gerard, and Xiang-Fa Gu. 1994. "Effect of Radiometric Corrections on NDVI-Determined from SPOT-HRV and Landsat-TM Data." *Remote Sensing of Environment 49:3*, September: 169-180.

Hall, Andrew, John Louis, and David Lamb. 2003. "Characterising and mapping vineyard canopy using high-spatial-resolution aerial multispectral images." *Computers & Geosciences 29*, March 10: 813-822.

Hansen, P.M., and J.K. Schjoerring. 2003. "Reflectance measurement of canopy biomass and nirtogen status in wheat crops using normalized difference vegetation indices and partial least squares regression." *Remote Sensing of Environment 86*, May 3: 542-533.

Herwitz, S. R, L. F Johnson, S. E Dunagan, R. G Higgins, D. V Sullivan, J. Zheng, B. M Lobitz, et al. 2004. "Imaging from an unmanned aerial vehicle: agricultural surveillance and decision support." *Computers and Electronics in Agriculture Volume 44 Issue 1*, February 23: 49-61.

Huete, A. R. 1988. "A Soil-Adjusted Vegetation Index (SAVI)." *Remote Sensing of Environment 25* 295-309.

Jannoura, Ramia, Katja Brinkmann, Daniel Uteau, Christian Bruns, and Rainer Georg Joergensen. 2014. "Monitoring of crop biomass using true colour aerial photographs taken from a remote controlled hexacopter." *Biosystems Engineering 129*, November 28: 341-351.

Jiang, Zhangyan, Alfredo R. Huete, Kamel Didan, and Tomoaki Miura. 2008. "Development of a two-band enhanced vegetation index without a blue band." *Remote Sensing of Environment*, June 6: 3833-3845.

Karagiannidis, N., T. Thomidis, G. Zakinthinos, and C. Tsipouridis. 2008. "Prognosis and correction of iron chlorosis in peach trees and relationship between iron concentration and Brown Rot." *Scientia Horticulturae*, June 3: 121-127.

Khatami, Reza, Giorgos Mountrakis, and Stephen V. Stehman. 2016. "A meta-analysis of remote sensing research on supervised pixel-based land-cover image classification processes: General guidelines for practitioners and future research." *Remote Sensing of Environment 177*, May: 89-100.

Konica Minolta. 2008. "Chlorophyll Meter SPAD-502 Users Manual."

Kotsiantis, S. B. 2011. *Feature selection for machine learning classification problems: a recent overview*. Rio, Greece: Educational Software Development Labratory, Department of Mathematics, University of Patras.

Kross, Angela, Heather McNairn, David Lapen, Mark Sunohara, and Catherine Chanpagne. 2014. "Assessment of RapidEye vegetation indices for estimation of leaf area index and biomass in corn and soybean crops." *International Journal of Applied Earth Observation and Geoinformation*, September 7: 235-248.

Lewis, H.G., and M. Brown. 2010. "A generalized confusion metrix for assessing area estimates from remotele sensed data." *International Journal of Remote Sensing 22:16*, November 25: 3223-3235.

Li, Fei, Yuxin Miao, Guohui Feng, Fei Yuan, Shanchao Yue, Xiaowei Gao, Yuqing Liu, Bin Liu, Susan L. Ustin, and Xinping Chen. 2014. "Improving estimation of summer maize nitrogen status with red edge-based spectral vegetation indices." *Field Crops Research* 111-123.

Livingston, S. D., C. G. Coffman, and L. G. Unruh. 1992. *Correcting Iron Deficiencies in Grain Sorghum.* Corpus Christi, Tx: Texas Agricultural Extension Service.

Lowe, David G. 2004. "Distinctive Image Features from Scale-Invariant Keypoints." *International Journal of Computer Vision*, January 5: 1-28.

Lum, Christopher, Madison Mackenzie, Charlie Shaw-Feather, Elaiza Luker, and Matthew Dunbabin. 2016. "Multispectral Imaging and Elevation Mapping from an Unmanned Aerial System for Precision Agriculture Applications." *13th International Conference on Precition Agriculture.* St. Louis, Missouri, USA: The International Society of Precision Agriculture. 1-17.

Luzum, Brian J., K. Clint Slatton, and Ramesh L. Shrestha. 2005. "Analysis of Spatial and Temporal Stability of Airborne Laser Swath Mapping Data in Feature Space." *IEEE Transactions on Geoscience and Remote Sensing 43:6*, June: 1403-1420.

McClure, Bill. n.d. "Sorghum Fertility Management." *Agronomy.* Johnston, Iowa: DuPont Pioneer.

Meggio, F., P.J. Zarco-Tejada, L.C. Nunez, G. Sepulcre-Canto, M.R. Gonzalez, and P. Martin. 2010. "Grape quality assessment in vineyards affected by iton deficiency chlorosis using narrow-band physiological remote sensing indices." *Remote Sensing of Environment 114*, April 10: 1968-1986.

MicaSense. 2017. *The Importance of Radiometric Calibration.* December 11. https://support.micasense.com/hc/en-us/articles/115002327753-The-Importance-of-Radiometric-Calibration.

Michelson, Daniel B., B. Marcus Liljeberg, and Petter Pilesjo. 2000. "Comparison of Algorithms for Classifying Swedish Landcover Using Landsat TM and ERS-1 SAR Data." *Remote Sensing of Environment 71*, 1-15.

Mulla, David J. 2013. "Twenty five years of remote sensing in precision agriculture: Key advances and remaining knowledge gaps." *Biosystems Engineering, Volume 114, Issue 4*, April: 358-371.

Mutanga, O., and A.K. Skidmore. 2004. "Narrow band vegetation indices overcome the saturation problem in biomass estimation." *International Journal of Remote Sensing* 25:19, 3999-4014, DOI: 10.1080/01431160310001654923.

Naik, Hsiang Sing, Jiaoping Zhang, Alec Lofquist, Teshale Assefa, Soumik Sarkar, David Ackerman, Arti Singh, Asheesh K. Singh, and Baskar Ganapathysubramanian. 2017. "A real-time phenotyping framework using machine learning for plant stress severity rating in soybean." *Plant Methods 13:23*, April 8.

Omran, Mahamed G.H., Andries P Engelbrecht, and Ayed Salman. 2005. "Differential Evolution Methods for Unsupervised Image Classification." *2005 IEEE Congress on Evolutionary Computation.* Edinburgh, Scotland, UK: IEEE. 966-973.

Otukei, J.R., and T. Blaschke. 2010. "Land cover change assessment using decision trees, support vector machines and maximum liklihood classification algorithms." *International Journal of Applied Earth Observation and Geoinformation 125* 527-531.

Parrot Drones SAS. 2018. "Sequoia - User Guide." Paris, France.

Patrignani, Andres, and Tyson E. Ochsner. 2015. "Canopeo: New Powerful New Tool for Measuring Fractional Green Canopy Cover." *Agronomy Journal 107*, January 25: 2312-2320.

Pix4D. 2011-2018. *Pix4D Quick Links.* https://support.pix4d.com/hc/en-us/sections/200591079-Quick-links.

—. 2011-2018. *Pix4Dmapper Software Manual.* https://support.pix4d.com/hc/en-us/sections/200591059-Manual.

Pix4D Support. 2011-2018. *How to process Sequoia imagery.* https://support.pix4d.com/hc/en-us/articles/209362146-How-to-process-Sequoia-imagery#label1.

Prasad, P.V.V. 2003. "NUTRITION: Iron Chlorosis." In *Encyclopedia of Applied Plant Sciences*, by Brian Thomas, Denis J Murphy and Brian G Murray, 649-656. Gainesville: Elsevier Ltd.

Ramoelo, A., A.K. Skidmore, M.A. Cho, M. Schlerf, R. Mathieu, and I.M.A. Heitkonig. 2012. "Regional estimation of savanna grass nitrogen using the red-edge band of the spaceborne RapidEye sensor." *International Journal of Applied Earth Observation and Geoinformation 19*, May 15: 151-162.

Rasmussen, Jesper, Georgios Ntakos, Jon Nielsen, Jesper Svensgaard, Robert N. Poulsen, and Svend Christensen. 2015. "Are vegetation indices derived from consumer-grade cameras mounted on UAVs sufficiently reliable for assessing experimental plots?" *European Journal of Agronomy,* November 29: 75-92.

Rondeaux, Genevieve, Michael Steven, and Frederic Baret. 1996. "Optimization of Soil-Adjusted Vegetation Indices." *Remote Sensing of Environment* 95-107.

Roosjen, Peter P. J., Juha M. Soumalainen, Harm M. Bartholomeus, Lammert Kooistra, and Jan G. P. W. Clevers. 2017. "Mapping Reflectance Anisotropy of a Potato Canopy Using Aerial Images Acquired with an Unmanned Aerial Vehicle." *Remote Sensing 9(5),* April 29: 417.

Sabins, Floyd F. 2007. *Remote Sensing: Principles and Interpretation, Third Edition.* Illinois: Waveland Press Inc.

Scanlan, Craig. 2015. "Diagnosing iron deficiency in cereals." *Agriculture and Food.* Government of Western Austrailia Department of Primary Industries and Regional Development, May 6.

Schlemmer, M., A. Gitelson, J. Schepers, R. Ferguson, Y. Peng, and J. Shanahan. 2013. "Remote estimation of nitrogen and chlorophyll contents in maize at leaf and canopy levels." *International Journal of Applied Earth Observation and Geoinformation 25,* April 5: 47-54.

Schmidt, K.S., and A.K. Skidmore. 2003. "Spectral discrimination of vegetation types in a coastal wetland." *Remote Sensing of Environment 85* 92-108.

Seager, S., E.L. Turner, J. Schafer, and E.B. Ford. 2005. "Vegetation's Red Edge: A Possible Spectroscopic Biosignature of Extraterrestrial Plants." *Astrobiology 5* 372-390.

Seelan, Santhosh K., Soizik Laguette, Grant M. Casady, and George A. Seielstad. 2003. "Remote sensing applications for precision agriculture: A learning community approach." *Remote Sensing of Environment 88,* April 22: 157-169.

senseFly Ltd. 2014. "eBee Extended User Manual." Lausanne, Switzerland: senseFly Ltd, September.

—. 2018. *eBee SQ.* https://www.sensefly.com/drone/ebee-sq-agriculture-drone/.

2017. *Sequoia Data Sheet.* March 21. https://support.micasense.com/hc/en-us/articles/216631668-Sequoia-Data-Sheet.

n.d. *Sequoia Frequently Asked Questions.* https://pix4d.com/sequoia-faq/.

Sisodia, Pushpendra Singh, Vivekanand Tiwari, and Anil Kumar. 2014. "Analysis of Supervised Maximum Likelihood Classification for Remote Sensing Image." *IEEE International Conference on Recent Advances and Innovations in Engineering.* Jaipur, India: IEEE. 1-4.

Snavely, Noah, Steven M. Seitz, and Richard Szeliski. 2008. "Modeling the World from Internet Photo Collections." *International Journal of Computer Visualization*, October 31: 189-210.

Sripada, Ravi P., John P. Schmidt, Adam E. Dellinger, and Douglas B. Beegle. 2008. "Evaluating Multiple Indices from a Canopy Reflectance Sensor to Estimate Corn N Requirements." *Agrnomy Journal 100* 1553-1561.

Stanton, Carly, Michael J. Starek, Norman Elliott, Michael Brewer, Murilo M. Maeda, and Tianxing Chu. 2017. "Unmanned aircraft system-derived crop height and normalized difference vegetation index metrics for sorghum yield and aphid stress assessment." *Journal of Applied Remote Sensing 11(2),* 026035-1 to 026035-20.

—. 2017. "Unmanned aircraft system-derived crop height and normalized difference vegetation index metrics for sorghum yield and aphid stress assessment." *Journal of Applied Remote Sensing.*

Strahler, Alah H. 1980. "The Use of Prior Probabilityes in Maximum Likelihood Classification of Remotely Sensed Data." *Remote Sensing of Environment 10*, 135-163.

Sugiura, Ryo, Noboru Noguchi, and Ishii Kazunobu. 2005. "Remote-sensing Technology for Vegetation Monitoring using an Unmanned Helicopter." *Biosystems Engineering*, December 11: 369-379.

Torres, J.C., G. Arroyo, and J. De Haro. 2012. "3D Digitization using Structure from Motion." *CEIG - Spanish Computer Graphics Conference.* Jaen, Spain: CEIG.

Toutin, T. 2004. "Review article: Geometric processing of remote sensing images: models, algorithms and methods." *International Journal of Remote Sensing, 25:10*, May 20: 1893-1924.

Trostle, Dr. Calvin. 2013. "Iron (Fe) Deficiency in Grain Sorghum." *Texas A&M Agrilife Extension.* July 25. http://texassorghum.org/iron-fe-deficiency-in-grain-sorghum.html.

Tucker, Compton T. 1979. "Red and Photographic Infrared Linear Combinations for Monitoring Vegetation." *Remote Sensing of Environment 8* 127-150.

Vega, Francisco Aguera, Fernando Carvajal Ramirez, Monica Perez Saiz, and Francisco Orgaz Rosua. 2015. "Multi-temporal imaging using an unmanned aerial vehicle for monitoring a sunflower crop." *Biosystems Engineering 132*, February 18: 19-27.

Villa, Paolo, Mariano Bresciani, Federica Braga, and Rossano Bolpagni. 2014. "Comparative assessment of broadband Vegetation Indices over aquatic vegetation." *IEEE Journal of Selected Topics in Applied Earch Observations and Remote Sensing*, April 23: 3117-3127.

Vina, Andres, Anatoly A. Gitelson, Anthony L. Nhuy-Robertson, and Yi Peng. 2011. "Comparison of different vegetation indices for the remote assessment of green leaf area index crops." *Remote sensing of Environment*, September 13: 3468-3478.

Westoby, M.J., J. Brasington, N.F. Glasser, M.J. Hambrey, and J.M. Reynolds. 2012. "'Structure-from-Motion' photogrammetry: A low-cost, effective tool for geoscience applications." *Geomorphology,* September 6: 300-314.

Whitehead, K., and C. Hugenholtz. 2015. "Applying ASPRS Accuracy Standards to Surveys from Small Unmanned Aircraft Systems (UAS)." *Photogrammetric Engineering & Remote Sensing*, October: 787-793.

Xiang, Haitao, and Lei Tian. 2011. "Development of a low-cost agricultural remote sensing system based on an autonomous unmanned aerial vehicle (UAV)." *Biosystems Engineering, Volume 108, Issue 2*, Feburary: 174-190.

Xiong, Dongliang, Jia Cheng, Tingting Yu, Wanlin Gao, Xiaoxia Ling, Yong Li, Shaobing Peng, and Jianliang Huang. 2015. "SPAD-based leaf nitrogen estimation is impacted by environmental factors and crop leaf characteristics." *Scientific Reports 5:13389* 1-12.

LIST OF APPENDICES

Appendix A: Time Series of Plot represented by sUAS acquired 4-band false colored multispectral image

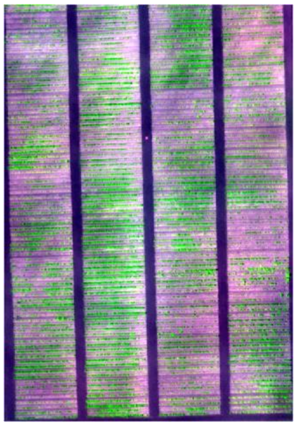

May 5, 2017

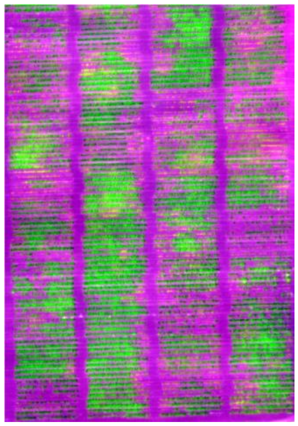

May 12, 2017

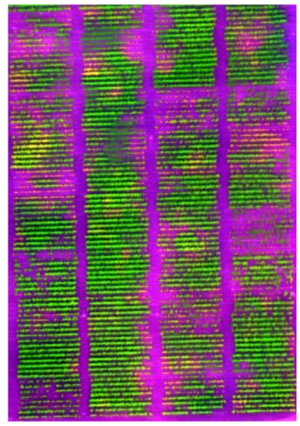

May 17, 2017

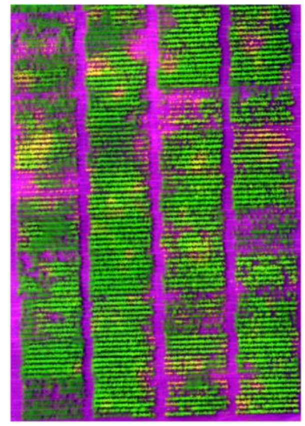

May 23, 2017

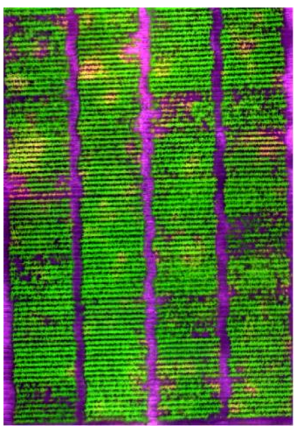

May 31, 2017

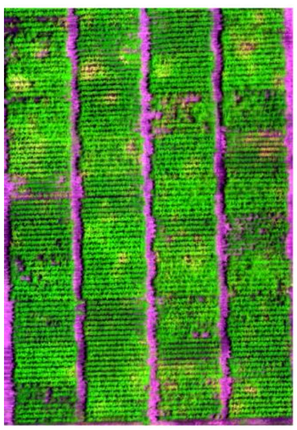

June 8, 2017

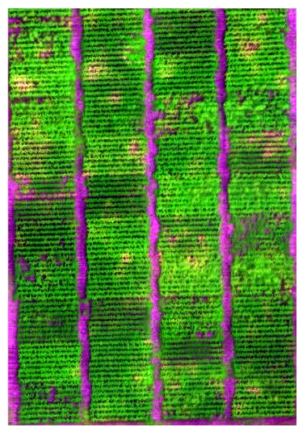

June 13, 2017

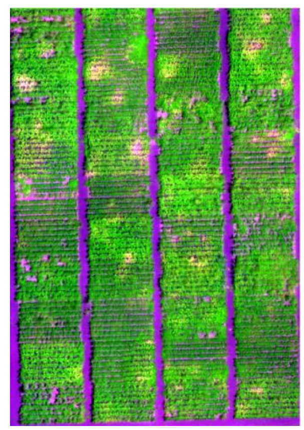

June 22, 2017

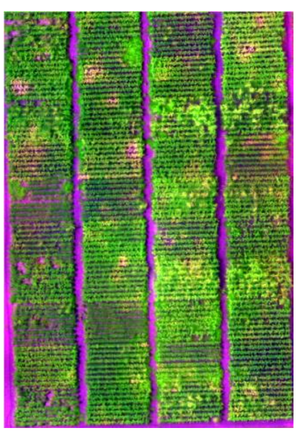

June 28, 2017

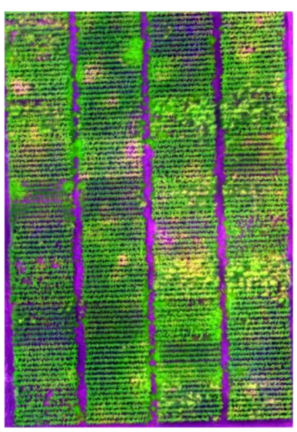

July 6, 2017

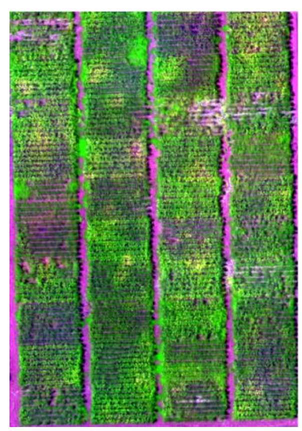

July 15, 2017

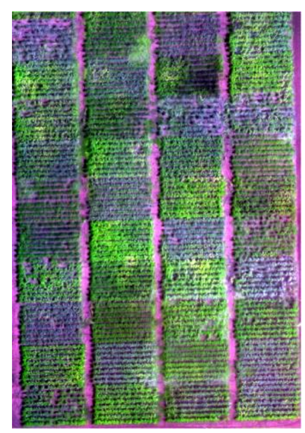

July 27, 2017

Appendix B: Examples of the code used to automate methodology processes

Appendix B.1: A sample of code used to clip the raster images

```
#-------------------------------------------------------------------------------
# Name:        Extract By Mask
# Purpose:     Extract areas of High, Med, and Low levels of IC from VI datasets
#
# Author:      Isabel Garcia
#
# Created:     06/06/2018
# Copyright:   (c) Isabel Garcia 2018
# Licence:     <your licence>
#-------------------------------------------------------------------------------

import arcpy
from arcpy import env
# Import Spatial Analysis toolbox
from arcpy.sa import *

# Check the ArcGIS Spatial Analyst
arcpy.CheckOutExtension("Spatial")

# Import mask data (common for all CC VIs)
mask = "C:/Users/igarcia21/Documents/AgriLife 2017/Polygons/Segments_Low_IC.shp"

# Set local variables (VI files)

## DVI
dvi = "C:/Users/igarcia21/Documents/AgriLife 2017/Multispec Imagery/17_05_05/CC VIs/CC_DVI/CC_DVI.tif"

# Execute Extract By Mask and save the output file to desired location

## DVI
out_dvi = ExtractByMask(dvi, mask)
out_dvi.save("C:/Users/igarcia21/Documents/AgriLife 2017/Multispec Imagery/17_05_05/CC VIs/CC_DVI/CC_DVI_L.tif")
```

Appendix B.2: A sample of code used to convert tiff to ASCII

```
#-------------------------------------------------------------------------------
# Name:        Raster to ASCII Regular VI
# Purpose:     Convert Clipped Y and G .tif Images to .txt
#
# Author:      Isabel Garcia
#
# Created:     28/05/2018
# Copyright:   (c) Isabel Garcia 2018
#-------------------------------------------------------------------------------

import arcpy
from arcpy import env

# Set local variables

## DVI
dviY = "C:/Users/Isabel Garcia/Documents/AgriLife 2017/Multispec Imagery/17_07_27/VIs/DVI/DVI_Y.tif"
out_dvi_y = "C:/Users/Isabel Garcia/Documents/AgriLife 2017/Multispec Imagery/17_07_27/VIs/DVI/DVI_Y.txt"

# Execute RasterToASCII

## DVI
arcpy.RasterToASCII_conversion(dviY, out_dvi_y)
arcpy.RasterToASCII_conversion(dviG, out_dvi_g)
```

Appendix B.3: Example of the code used to calculate f-Distance

```
%% Isabel Garcia
% Seperability Script
% Luzum, Slatton, & Shrestha et.al. 2005

%% DVI

% Step 1: Import and clean files

format short g

% Import files
% Skip the header lines to access only the data
% 6 skips the first 6 lines, 0 skips 0 columns
green  =  dlmread('C://Users/Isabel  Garcia/Documents/AgriLife  2017/Multispec
Imagery/17_05_12/VIs/DVI/dvi_g.txt'...
    ,'', 6, 0);

yellow  =  dlmread('C://Users/Isabel  Garcia/Documents/AgriLife  2017/Multispec
Imagery/17_05_12/VIs/DVI/dvi_y.txt'...
    ,'', 6, 0);

% Convert matrix to vector;
gVector = green(:);
yVector = yellow(:);

% Rid all of the null values from the file
g = gVector(gVector ~= -9999);
y = yVector(yVector ~= -9999);

% Step 2: Perform initial calculations

% Compute median values
mG = median(g);
mIC = median(y);

% Compute median absolute deviation
madG = median(abs(g-median(g)));
madIC = median(abs(y-median(y)));

% Step 3: Calculate seperability

dvi_Sep = abs((mIC-mG)/sqrt(madIC^2+madG^2))
```

Appendix B.4: Example of the validation code used to calculate Jeffries-Matusita (JM) Distance

```
%% Isabel Garcia
% Seperability Script
% JM Distance with Median (instead of mean)

%% Step 1: Import and clean files

format short g

% Import files
% Skip the header lines to access only the data
% 6 skips the first 6 lines, 0 skips 0 columns
green = dlmread('C://Users/igarcia21/My Documents/Agrilife 2017/Multispec Imagery/17_06_28/CC VIs/CC_OSAVI_RE/cc_osavi_re_g.txt'...
    ,'', 6, 0);

yellow = dlmread('C://Users/igarcia21/My Documents/Agrilife 2017/Multispec Imagery/17_06_28/CC VIs/CC_OSAVI_RE/cc_osavi_re_y.txt'...
    ,'', 6, 0);

% Convert matrix to vector;
gVector = green(:);
yVector = yellow(:);

% Rid all of the null values from the file
g = gVector(gVector ~= -9999);
y = yVector(yVector ~= -9999);

%% Step 2: Compute B

% Compute median values
mG = median(g);
mIC = median(y);

% Compute variance
varG = var(g);
varIC = var(y);

% Compute B
B = 1/8*(mG - mIC)^2 * 2/(varG^2+varIC^2) + 1/2 * log((varG^2+varIC^2)/(2*varG*varIC)); %in MatLab log() is ln

%% Step 3: Calculate seperability, JM Distance

JM = 2*(1-exp(-B))
```

Appendix C: A comparison between JM distance and f-Distance separability measures for soil-included and soil-removed datasets from June 28, 2017.

Note: The separability measures are ranked from smallest (worst performing) to largest (best performing).

Soil-Included Vegetation Indices Ranked Low - High			
Vegetation Index (VI)	**Seperability Ranking (d_f)**	**Vegetation Index (VI)**	**Seperability Measure (JM Dist)**
DVI	0.0073336	DVI	0.055895
EVI2	0.16269	SR	0.091059
OSAVI RE	0.19958	EVI2	0.61302
GDVI	0.20832	ENDVI_RE	1.1497
ENDVI_RE	0.22929	OSAVI RE	1.3414
NGRDI	0.282	SAVI	1.4068
SAVI	0.30752	GDVI	1.5175
SAVI RE	0.31298	SAVI RE	1.603
GDVI RE	0.32356	NDVI_RE	1.6683
NDVI_RE	0.35987	NGRDI	1.6866
TVI RE	0.36068	OSAVI	1.9712
OSAVI	0.41307	TVI RE	1.9834
EVI2 RE	0.47051	EVI2 RE	1.9971
NR	0.76518	DVI RE	1.9997
DVI RE	0.76662	ENDVI	1.9997
ENDVI	0.76662	GDVI RE	2
TVI	0.87325	GNDVI	2
NDVI	0.87441	GNDVI_RE	2
SR	0.91543	GOSAVI	2
GOSAVI	1.0295	MTCI	2
GNDVI_RE	1.0677	ND RE	2
GNDVI	1.6975	NDVI	2
MTCI	1.7009	NG	2
ND RE	1.7079	NR	2
NG	1.8839	TVI	2

Soil-Removed Vegetation Indices Ranked Low - High			
Vegetation Index (VI)	**Seperability Measure (d_f)**	**Vegetation Index (VI)**	**Seperability Measure (JM Dist)**
DVI	0.038603	SR	0.13697
EVI2	0.16366	DVI	0.15055
GDVI	0.20214	EVI2	0.93438
ENDVI_RE	0.24106	ENDVI_RE	1.6244
OSAVI RE	0.26103	GDVI	1.7299
SAVI	0.34924	SAVI	1.9137
NGRDI	0.34929	NGRDI	1.9682
SAVI RE	0.3837	OSAVI RE	1.9743
TVI RE	0.3924	NDVI_RE	1.9764
NDVI_RE	0.39247	SAVI RE	1.9916
GDVI RE	0.42888	DVI RE	2
OSAVI	0.47513	ENDVI	2
EVI2 RE	0.58889	EVI2 RE	2
DVI RE	0.74297	GDVI RE	2
NR	0.82774	GNDVI	2
ENDVI	0.83222	GNDVI_RE	2
TVI	0.94619	GOSAVI	2
NDVI	0.94828	MTCI	2
SR	1.0099	ND RE	2
GOSAVI	1.1782	NDVI	2
GNDVI_RE	1.2086	NG	2
ND RE	1.7382	NR	2
MTCI	1.7575	OSAVI	2
GNDVI	1.8227	TVI	2
NG	1.9873	TVI RE	2

Appendix D: Top and Bottom three separable VIs for combined chlorosis.

Top three performing soil-included VIs by date. The values are the separability values, calculated by the f-Distance, between healthy vegetation and vegetation containing all levels of iron chlorosis.

Best Performing Soil-Included VIs						
Date	**1st**		**2nd**		**3rd**	
05_05	GDVI	0.55226	SR	0.52892	MTCI	0.52796
05_12	MTCI	1.1568	ND RE	1.1306	NG	0.91686
05_17	ND RE	1.4994	MTCI	1.4707	NG	1.3394
05_23	MTCI	1.7439	ND RE	1.7166	NG	1.6539
05_31	MTCI	1.8286	NG	1.7654	GNDVI	1.6336
06_08	MTCI	2.1011	ND RE	1.9462	NG	1.9437
06_13	MTCI	2.4312	ND RE	2.3358	NG	2.1075
06_22	NG	2.2345	MTCI	2.2184	ND RE	2.0848
06_28	NG	1.8839	ND RE	1.7079	MTCI	1.7009
07_06	NG	1.5648	GNDVI	1.3534	ND RE	1.3451
07_15	NGRDI	1.0833	NG	0.94931	ND RE	0.86454
07_27	NG	0.63373	ENDVI	0.44153	NGRDI	0.4392

Top three performing soil-removed VIs by date. The values are the separability values, calculated by the f-Distance, between healthy vegetation and vegetation containing all levels of iron chlorosis.

Best Performing Soil-Removed VIs						
Date	**1st**		**2nd**		**3rd**	
05_05	GOSAVI	0.59733	GNDVI	0.58726	GNDVI RE	0.53835
05_12	ND RE	1.1068	MTCI	0.93357	NG	0.74687
05_17	ND RE	1.57	MTCI	1.4847	NG	1.3482
05_23	MTCI	1.8791	NG	1.8606	GNDVI	1.7137
05_31	MTCI	1.9348	ND RE	1.8204	NG	1.7521
06_08	MTCI	2.2265	NG	2.0573	ND RE	2.0459
06_13	MTCI	2.5577	ND RE	2.4787	NG	2.1207
06_22	MTCI	2.2492	NG	2.1661	NDRE	2.1064
06_28	NG	1.9873	GNDVI	1.8227	MTCI	1.7575
07_06	NG	1.6886	GNDVI	1.4862	ND RE	1.4474
07_15	NG	1.2651	GNDVI	1.0702	NGRDI	1.0661
07_27	NG	0.76203	NGRDI	0.53008	DVI RE	0.49216

The worst three performing VIs by date. The values are the separability values, calculated by the f-Distance, between healthy vegetation and vegetation containing all levels of iron chlorosis.

Worst Performing Soil-Included VIs						
Date	**1st**		**2nd**		**3rd**	
05_05	NGRDI	0.1454	GNDVI RE	0.3556	NDRE	0.3586
05_12	NGRDI	0.4243	GDVI RE	0.4362	DVI RE	0.4846
05_17	NGRDI	0.5358	DVI RE	0.5434	SAVI RE	0.5655
05_23	DVI RE	0.2721	GNDVI RE	0.3450	GDVI RE	0.3450
05_31	DVI RE	0.0932	NGRDI	0.0965	EVI2 RE	0.2536
06_08	GDVI RE	0.0054	EVI2 RE	0.0250	SAVI RE	0.0744
06_13	NGRDI	0.0023	DVI	0.2417	GDVI RE	0.2787
06_22	NGRDI	0.0324	DVI	0.0747	OSAVI RE	0.1378
06_28	DVI	0.0073	EVI2	0.1627	OSAVI RE	0.1996
07_06	TVI RE	0.0036	NDVI RE	0.0036	EVI2	0.0198
07_15	NDVI	0.0805	TVI	0.0806	SR	0.0817
07_27	GOSAVI	0.0355	MTCI	0.0991	GDVI	0.1427

The worst three performing soil-removed VIs by date. The values are the separability values, calculated by the f-Distance, between healthy vegetation and vegetation containing all levels of iron chlorosis.

Worst Performing Soil-Removed VIs						
Date	**1st**		**2nd**		**3rd**	
05_05	NGRDI	0.1477	ENDVI RE	0.3547	DVI RE	0.3601
05_12	GDVI RE	0.0737	DVI RE	0.1160	SAVI RE	0.1834
05_17	NGRDI	0.0936	DVI RE	0.1115	SAVI RE	0.1455
05_23	GDVI RE	0.0450	NGRDI	0.0540	DVI RE	0.0704
05_31	EVI2 RE	0.0287	SAVI RE	0.0579	NGRDI	0.0862
06_08	NGRDI	0.0686	GDVI RE	0.1069	EVI2 RE	0.1497
06_13	NGRDI	0.0550	DVI	0.1645	SAVI	0.2543
06_22	DVI	0.0608	GDVI	0.1863	NGRDI	0.1968
06_28	DVI	0.0386	EVI2	0.1637	GDVI	0.2021
07_06	NDVI RE	0.0294	TVI RE	0.0294	EVI2	0.0324
07_15	NR	0.0097	ENDVI	0.0097	NDVI	0.1227
07_27	GOSAVI	0.0870	MTCI	0.1180	GNDVI RE	0.1424

Appendix E: Top and Bottom three separable VIs for each level of chlorosis.

Top three performing soil-included VIs for mild levels of chlorosis by date. The values are the separability values, calculated by the f-Distance, between healthy vegetation and vegetation containing mild levels of iron chlorosis.

Top Performing Soil-Included VIs (Mild)						
Date	**1st**		**2nd**		**3rd**	
05_05	NDRE	0.7631	NG	0.6782	GDVI	0.6767
05_12	NDRE	0.9293	MTCI	0.7331	NG	0.5692
05_17	NDRE	1.1922	MTCI	1.1841	NG	0.7195
05_23	MTCI	0.9813	NG	0.9252	GNDVI	0.8814
05_31	MTCI	0.9112	NDRE	0.9100	NG	0.8126
06_08	NG	0.7769	GNDVI	0.7689	NDRE	0.6933
06_13	MTCI	1.0748	NDRE	1.0652	GNDVI	1.0413
06_22	NDRE	1.2022	MTCI	1.1295	NG	0.8028
06_28	NG	1.0797	NDRE	1.0596	MTCI	0.9817
07_06	NDRE	1.2472	MTCI	1.1572	NG	0.9180
07_15	NDRE	1.2546	MTCI	1.1484	NG	1.0319
07_27	NDRE	0.6666	MTCI	0.6286	NG	0.6259

Top three performing soil-removed VIs for mild levels of chlorosis by date. The values are the separability values, calculated by the f-Distance, between healthy vegetation and vegetation containing mild levels of iron chlorosis.

Top Performing Soil-Removed VIs (Mild)						
Date	**1st**		**2nd**		**3rd**	
05_05	NDRE	0.9832	MTCI	0.9818	NG	0.9394
05_12	NDRE	1.2143	MTCI	0.9488	NG	0.8105
05_17	NDRE	1.3254	MTCI	1.2485	NG	0.8965
05_23	NG	1.1630	GNDVI	1.0640	MTCI	0.9582
05_31	MTCI	1.0300	NDRE	0.9651	NG	0.8387
06_08	MTCI	0.8051	NDRE	0.7988	NG	0.7728
06_13	NDRE	1.1129	MTCI	1.1067	NG	0.9795
06_22	MTCI	1.2478	NDRE	1.2474	NG	0.8223
06_28	NG	1.1539	NDRE	1.1060	GNDVI	1.0523
07_06	NDRE	1.3173	MTCI	1.2076	GNDVI	1.0021
07_15	NG	1.4297	GNDVI	1.3539	NDRE	1.2915
07_27	NDRE	0.6890	MTCI	0.6330	NG	0.6278

Top three performing soil-included VIs for moderate levels of chlorosis by date. The values are the separability values, calculated by the f-Distance, between healthy vegetation and vegetation containing moderate levels of iron chlorosis.

Top Performing Soil-Included VIs (Moderate)						
Date	**1st**		**2nd**		**3rd**	
05_05	NDRE	0.2146	GNDVI RE	0.1729	GDVI RE	0.1203
05_12	NDRE	0.6935	MTCI	0.5967	NG	0.4096
05_17	NDRE	1.2192	MTCI	0.9653	NG	0.8369
05_23	NDRE	1.7016	MTCI	1.6134	NG	1.5841
05_31	NG	1.7439	GNDVI	1.6562	GNDVI RE	1.6222
06_08	NG	2.0994	GNDVI	1.9357	MTCI	1.9240
06_13	MTCI	2.5199	NDRE	2.4153	NG	2.2459
06_22	NG	2.1091	MTCI	2.0553	NDRE	2.0129
06_28	NG	1.4268	GNDVI	1.2488	NDRE	1.1811
07_06	NGRDI	1.3053	NG	1.1964	DVI RE	1.0483
07_15	NGRDI	1.6989	ENDVI RE	1.1034	OSAVI RE	1.0797
07_27	OSAVI	0.7503	ENDVI	0.7222	SAVI	0.7173

Top three performing soil-removed VIs for moderate levels of chlorosis by date. The values are the separability values, calculated by the f-Distance, between healthy vegetation and vegetation containing moderate levels of iron chlorosis.

Top Performing Soil-Removed VIs (Moderate)						
Date	**1st**		**2nd**		**3rd**	
05_05	GNDVI RE	0.4075	GNDVI	0.3315	SR	0.3213
05_12	NDRE	0.6747	GDVI RE	0.4109	MTCI	0.4083
05_17	NDRE	1.4211	NG	1.3001	MTCI	1.1825
05_23	NDRE	2.0977	MTCI	1.9771	NG	1.8891
05_31	NG	1.8868	GNDVI RE	1.8598	GNDVI	1.8291
06_08	NG	2.2731	GNDVI	2.1103	MTCI	2.0417
06_13	MTCI	2.6288	NDRE	2.5901	NG	2.2562
06_22	NG	2.1736	MTCI	2.1236	NDRE	2.0440
06_28	NG	1.4921	GNDVI	1.3113	NDRE	1.1630
07_06	NG	1.3494	NGRDI	1.3295	GNDVI	1.1156
07_15	NGRDI	1.5676	ENDVI RE	0.9980	OSAVI RE	0.9632
07_27	DVI	0.7089	NGRDI	0.6869	EVI2	0.6717

Top three performing soil-included VIs for severe levels of chlorosis by date. The values are the separability values, calculated by the f-Distance, between healthy vegetation and vegetation containing severe levels of iron chlorosis.

Top Performing Soil- Included VIs (Severe)						
Date	**1st**		**2nd**		**3rd**	
05_05	GDVI	1.0885	MTCI	1.0869	DVI	0.9913
05_12	NDRE	1.6303	NG	1.5692	MTCI	1.5341
05_17	MTCI	2.1196	NG	2.0133	NDRE	1.9293
05_23	NG	3.2083	MTCI	2.6780	GNDVI	2.5549
05_31	NG	3.5034	GNDVI	3.2507	GNDVI_RE	2.9148
06_08	NG	4.9873	GNDVI	3.8094	MTCI	3.5365
06_13	NG	3.9025	GNDVI	3.4058	MTCI	3.4035
06_22	NG	4.1919	GNDVI	3.6068	MTCI	3.3641
06_28	NG	2.7204	NDRE	2.7113	MTCI	2.5625
07_06	NG	2.4361	NDRE	2.2304	GNDVI	2.1376
07_15	NG	1.4451	GNDVI	1.1972	NDRE	1.0758
07_27	NG	0.7097	GNDVI	0.3481	NDRE	0.2373

Top three performing soil-removed VIs for severe levels of chlorosis by date. The values are the separability values, calculated by the f-Distance, between healthy vegetation and vegetation containing severe levels of iron chlorosis.

Top Performing Soil-Removed VIs (Severe)						
Date	**1st**		**2nd**		**3rd**	
05_05	MTCI	1.4382	NDRE	1.3543	GDVI	1.1095
05_12	NDRE	2.2108	MTCI	1.8705	NG	1.8227
05_17	NG	2.4279	MTCI	2.2868	GNDVI	2.2853
05_23	NG	3.0368	GNDVI	2.7335	MTCI	2.5322
05_31	NG	3.2859	GNDVI	2.9725	MTCI	2.9096
06_08	NG	4.6633	GNDVI	3.8929	MTCI	3.7825
06_13	NG	4.1291	GNDVI	3.6275	MTCI	3.5564
06_22	NG	4.2020	GNDVI	3.7813	MTCI	3.6157
06_28	NG	3.0446	NDRE	2.8482	GNDVI	2.8198
07_06	NG	2.7612	GNDVI	2.4001	NDRE	2.3942
07_15	NG	1.8697	GNDVI	1.6077	NDRE	1.2111
07_27	NG	0.8318	GNDVI	0.4170	DVI_RE	0.3439

Worst three performing soil-included VIs for mild levels of chlorosis by date. The values are the separability values, calculated by the f-Distance, between healthy vegetation and vegetation containing mild levels of iron chlorosis.

Worst Performing Soil-Included VIs (Mild)						
Date	**1st**		**2nd**		**3rd**	
05_05	NGRDI	0.0710	ENDVI RE	0.0814	TVI RE	0.1586
05_12	NGRDI	0.1699	DVI RE	0.1898	TVI RE	0.1901
05_17	DVI RE	0.1957	SAVI RE	0.2037	EVI2 RE	0.2052
05_23	DVI RE	0.1459	GNDVI RE	0.1750	GDVI RE	0.1750
05_31	DVI RE	0.0004	NGRDI	0.0195	EVI2 RE	0.0503
06_08	SAVI RE	0.0086	DVI RE	0.0137	EVI2 RE	0.0471
06_13	NGRDI	0.0919	GDVI RE	0.0930	OSAVI RE	0.1080
06_22	ENDVI RE	0.0163	NDVI RE	0.0277	NGRDI	0.0377
06_28	SAVI RE	0.0010	GDVI RE	0.0124	OSAVI RE	0.0335
07_06	EVI2 RE	0.0283	DVI RE	0.0373	GDVI RE	0.0556
07_15	DVI RE	0.0371	EVI2 RE	0.0458	SAVI RE	0.0474
07_27	GDVI RE	0.0397	DVI RE	0.0789	EVI2 RE	0.1258

Worst three performing soil-removed VIs for mild levels of chlorosis by date. The values are the separability values, calculated by the f-Distance, between healthy vegetation and vegetation containing mild levels of iron chlorosis.

Worst Performing Soil-Removed VIs (Mild)						
Date	**1st**		**2nd**		**3rd**	
05_05	NGRDI	0.0231	ENDVI RE	0.2854	TVI RE	0.3516
05_12	NGRDI	0.1995	DVI RE	0.2117	GDVI RE	0.2389
05_17	OSAVI RE	0.0207	GDVI RE	0.0225	EVI2 RE	0.0272
05_23	DVI RE	0.2001	GDVI RE	0.2345	EVI2 RE	0.2554
05_31	OSAVI RE	0.0419	SAVI RE	0.0627	EVI2 RE	0.0681
06_08	GDVI RE	0.0054	OSAVI RE	0.0544	EVI2 RE	0.0755
06_13	ENDVI RE	0.1298	GDVI RE	0.1435	NGRDI	0.1549
06_22	DVI	0.0409	NDVI RE	0.0885	TVI RE	0.0889
06_28	ENDVI RE	0.0042	NDVI RE	0.0965	TVI RE	0.0968
07_06	OSAVI RE	0.0085	SAVI RE	0.0369	EVI2 RE	0.0891
07_15	DVI RE	0.0723	EVI2 RE	0.0869	SAVI RE	0.0917
07_27	DVI RE	0.0160	EVI2 RE	0.0249	SAVI RE	0.0282

Worst three performing soil-included VIs for moderate levels of chlorosis by date. The values are the separability values, calculated by the f-Distance, between healthy vegetation and

Worst Performing Soil-Included VIs (Moderate)						
Date	**1st**		**2nd**		**3rd**	
05_05	DVI	0.0112	ENDVI RE	0.0193	SAVI	0.0236
05_12	GDVI RE	0.0032	DVI RE	0.0408	SAVI RE	0.0983
05_17	NGRDI	0.1341	GNDVI	0.1953	DVI RE	0.2478
05_23	GNDVI RE	0.0020	GDVI RE	0.0020	EVI2 RE	0.0279
05_31	SAVI RE	0.1026	GDVI RE	0.1083	EVI2 RE	0.1185
06_08	DVI	0.0014	SAVI	0.1894	OSAVI RE	0.2202
06_13	GDVI	0.0071	OSAVI	0.1166	EVI2	0.1197
06_22	EVI2	0.0127	GDVI	0.0963	ENDVI RE	0.2423
06_28	GDVI	0.0097	OSAVI	0.0317	SAVI	0.0727
07_06	SR	0.0805	NDVI	0.0820	TVI	0.0823
07_15	GNDVI RE	0.0488	GNDVI	0.2638	MTCI	0.2758
07_27	GNDVI	0.0225	NDRE	0.0479	GNDVI RE	0.0500

vegetation containing moderate levels of iron chlorosis.

Worst three performing soil-removed VIs for moderate levels of chlorosis by date. The values are the separability values, calculated by the f-Distance, between healthy vegetation and vegetation containing moderate levels of iron chlorosis.

Worst Performing Soil-Included VIs (Severe)						
Date	**1st**		**2nd**		**3rd**	
05_05	NGRDI	0.3896	GNDVI RE	0.5306	GDVI RE	0.6555
05_12	NGRDI	0.7263	GDVI RE	0.9418	DVI RE	0.9840
05_17	DVI RE	0.9143	SAVI RE	0.9554	EVI2 RE	0.9605
05_23	DVI RE	0.6374	GNDVI RE	0.6952	GDVI RE	0.6952
05_31	NGRDI	0.3012	DVI RE	0.3649	EVI2 RE	0.6186
06_08	DVI RE	0.0157	SAVI RE	0.2512	GDVI RE	0.3149
06_13	OSAVI RE	0.0404	GDVI RE	0.0625	EVI2 RE	0.2444
06_22	SAVI RE	0.0742	TVI RE	0.0746	OSAVI RE	0.1376
06_28	SAVI RE	0.0879	OSAVI RE	0.1100	DVI	0.1144
07_06	DVI	0.0725	OSAVI RE	0.1033	SAVI RE	0.2152
07_15	ENDVI	0.0830	NR	0.0832	NDVI RE	0.0885
07_27	GDVI	0.0060	TVI RE	0.1037	NDVI RE	0.1043

Worst three performing soil-included VIs for severe levels of chlorosis by date. The values are the separability values, calculated by the f-Distance, between healthy vegetation and vegetation containing severe levels of iron chlorosis.

Worst Performing Soil-Removed VIs (Moderate)						
Date	**1st**		**2nd**		**3rd**	
05_05	MTCI	0.0308	GDVI	0.0509	NDRE	0.0603
05_12	OSAVI RE	0.0022	EVI2	0.0241	SAVI	0.0462
05_17	OSAVI RE	0.0429	GDVI RE	0.0613	ENDVI RE	0.1069
05_23	ENDVI RE	0.0868	OSAVI RE	0.1354	NDVI RE	0.1906
05_31	OSAVI RE	0.0470	DVI	0.2115	NGRDI	0.2940
06_08	DVI	0.0774	OSAVI RE	0.1832	NGRDI	0.2179
06_13	GDVI	0.0462	GOSAVI	0.0466	EVI2	0.1054
06_22	EVI2	0.0013	GDVI	0.1172	ENDVI RE	0.2955
06_28	GDVI	0.0201	OSAVI	0.0274	SAVI	0.0919
07_06	SR	0.0265	NDVI	0.0266	TVI	0.0266
07_15	GNDVI RE	0.2016	GOSAVI	0.3571	NDVI	0.4090
07_27	NDRE	0.0103	GNDVI	0.0757	MTCI	0.1259

Worst three performing soil-removed VIs for severe levels of chlorosis by date. The values are the separability values, calculated by the f-Distance, between healthy vegetation and vegetation containing severe levels of iron chlorosis.

Worst Performing Soil-Removed VIs (Severe)						
Date	**1st**		**2nd**		**3rd**	
05_05	NGRDI	0.2866	ENDVI RE	0.5827	EVI2 RE	0.6311
05_12	NGRDI	0.4007	DVI RE	0.5727	GDVI RE	0.6064
05_17	DVI RE	0.5394	SAVI RE	0.5928	NGRDI	0.5929
05_23	DVI RE	0.2368	GDVI RE	0.3867	EVI2 RE	0.5246
05_31	NGRDI	0.0429	DVI RE	0.1250	EVI2 RE	0.4467
06_08	SAVI RE	0.1182	EVI2 RE	0.2056	GDVI RE	0.2073
06_13	OSAVI RE	0.2332	GDVI RE	0.2407	NGRDI	0.2491
06_22	OSAVI RE	0.0284	DVI	0.1114	NGRDI	0.1849
06_28	DVI	0.0091	OSAVI RE	0.0385	SAVI RE	0.1724
07_06	DVI	0.0666	OSAVI RE	0.1164	NGRDI	0.2187
07_15	NDVI RE	0.0661	TVI RE	0.0662	ENDVI RE	0.1224
07_27	GOSAVI	0.0640	GNDVI RE	0.1363	GDVI	0.1651

Appendix F: Separability results, for the entire dataset, between healthy vegetation and iron chlorosis as a whole

Separability of Soil-Included VIs												
	05_05	**05_12**	**05_17**	**05_23**	**05_31**	**06_08**	**06_13**	**06_22**	**06_28**	**07_06**	**07_15**	**07_27**
DVI	0.5125	0.6767	0.7840	0.6917	0.5948	0.4677	0.2417	0.0747	0.0073	0.1044	0.5190	0.3265
DVI_RE	0.3880	0.4846	0.5434	0.2721	0.0932	0.2487	0.5060	0.7316	0.7666	0.6049	0.7562	0.3890
ENDVI	0.4593	0.7823	0.9476	0.9339	1.2720	1.3644	1.4010	1.2025	0.7666	0.3444	0.1947	0.4415
ENDVI_RE	0.3858	0.5810	0.7331	0.6986	0.9322	0.9437	0.7904	0.5726	0.2293	0.1317	0.5127	0.3958
EVI2	0.5188	0.6992	0.8047	0.7812	0.7729	0.7198	0.3317	0.3597	0.1627	0.0198	0.5121	0.3642
EVI2_RE	0.3922	0.5279	0.5728	0.4085	0.2536	0.0250	0.4415	0.5339	0.4705	0.5122	0.7602	0.3751
GDVI	0.5523	0.6978	0.8948	0.8034	0.7931	0.7148	0.4490	0.2715	0.2083	0.1154	0.3424	0.1427
GDVI_RE	0.3723	0.4362	0.6862	0.3450	0.3235	0.0054	0.2787	0.6337	0.3236	0.3643	0.5186	0.2217
GNDVI	0.4925	0.8821	0.6843	1.4901	1.6336	1.8009	2.0127	2.0137	1.6975	1.3534	0.7831	0.2118
GNDVI_RE	0.3556	0.6668	1.0135	0.3450	1.5258	1.7120	1.5276	1.2279	1.0677	0.7665	0.3696	0.1471
GOSAVI	0.5279	0.8131	1.0085	1.2277	1.4498	1.5480	1.0371	1.3767	1.0295	0.9017	0.2360	0.0355
MTCI	0.5280	1.1568	1.4707	1.7439	1.8286	2.1011	2.4312	2.2184	1.7009	1.2384	0.6975	0.0991
NDRE	0.3586	1.1306	1.4994	1.7166	1.7300	1.9462	2.3358	2.0848	1.7079	1.3451	0.8645	0.1761
NDVI	0.5227	0.7457	0.9764	0.9754	1.2888	1.3717	1.4451	1.2681	0.8744	0.4752	0.0805	0.3853
NDVI_RE	0.4005	0.5892	0.7998	0.7598	1.0369	1.0607	0.9025	0.6717	0.3599	0.0036	0.3627	0.3252
NG	0.4670	0.9169	1.3394	1.6539	1.7654	1.9437	2.1075	2.2345	1.8839	1.5648	0.9493	0.6337
NGRDI	0.1454	0.4243	0.5358	0.3466	0.0965	0.0919	0.0023	0.0324	0.2820	0.5666	1.0833	0.4392
NR	0.4579	0.7224	0.9308	0.9226	1.2546	1.3452	1.3825	1.1885	0.7652	0.3451	0.1946	0.4391
OSAVI	0.5272	0.7124	0.8428	0.8504	1.0072	1.0574	0.5527	0.7647	0.4131	0.2028	0.5092	0.3926
OSAVI_RE	0.3891	0.5540	0.6178	0.5568	0.5033	0.3354	0.2954	0.1378	0.1996	0.3441	0.7440	0.3648
SAVI	0.5169	0.7019	0.8022	0.7847	0.7836	0.6721	0.3151	0.6170	0.3075	0.1389	0.5126	0.3700
SAVI_RE	0.3917	0.5219	0.5655	0.4171	0.2760	0.0744	0.4612	0.3073	0.3130	0.4089	0.7610	0.3765
SR	0.5289	0.7452	1.0087	1.0565	1.4709	1.6666	1.6898	1.4333	0.9154	0.4764	0.0817	0.3994
TVI	0.5205	0.7472	0.9604	0.9644	1.2762	1.3588	1.4355	0.6161	0.8733	0.4766	0.0806	0.3838
TVI_RE	0.3997	0.5873	0.7862	0.7522	1.0322	1.0504	0.8970	0.3086	0.3607	0.0036	0.3623	0.3240

Separability of Soil-Removed VIs												
	05_05	**05_12**	**05_17**	**05_23**	**05_31**	**06_08**	**06_13**	**06_22**	**06_28**	**07_06**	**07_15**	**07_27**
DVI	0.4937	0.3629	0.4929	0.5406	0.5675	0.5151	0.1645	0.0608	0.0386	0.1345	0.5435	0.4555
DVI_RE	0.3601	0.1160	0.1115	0.0704	0.1874	0.4312	0.6761	1.0767	0.7430	0.7120	0.7952	0.4922
ENDVI	0.4346	0.4496	0.6991	0.9613	1.3937	1.3770	1.4764	1.2885	0.8322	0.4016	0.0097	0.4334
ENDVI_RE	0.3547	0.3338	0.4664	0.5932	0.9970	0.9908	0.8028	0.6012	0.2411	0.1322	0.4440	0.4321
EVI2	0.5014	0.4375	0.5312	0.6892	0.7949	0.8255	0.2793	0.3242	0.1637	0.0324	0.5323	0.4396
EVI2_RE	0.3858	0.1981	0.1552	0.0871	0.0287	0.1497	0.6103	0.7984	0.5889	0.5951	0.7827	0.4848
GDVI	0.5267	0.4533	0.6649	0.7242	0.8124	0.8043	0.4183	0.1863	0.2021	0.1134	0.3433	0.2598
GDVI_RE	0.4338	0.0737	0.3461	0.0450	0.1242	0.1069	0.4163	0.9117	0.4289	0.4484	0.5038	0.3062
GNDVI	0.5873	0.6843	1.2033	1.7137	1.6866	1.9287	2.0155	1.9995	1.8227	1.4862	1.0702	0.2680
GNDVI_RE	0.5384	0.5065	0.9286	1.2536	1.6388	1.8813	1.5940	1.2512	1.2086	0.8875	0.6203	0.1424
GOSAVI	0.5973	0.6342	0.8626	1.3261	1.4747	1.6303	0.4168	1.4817	1.1782	0.9954	0.1654	0.0870
MTCI	0.4856	0.9336	1.4847	1.8791	1.9348	2.2265	2.5577	2.2492	1.7575	1.3152	0.8539	0.1180
NDRE	0.4053	1.1068	1.5700	1.8500	1.8204	2.0459	2.4787	2.1064	1.7382	1.4474	0.9432	0.2268
NDVI	0.5114	0.5023	0.7409	1.0323	1.4013	1.3855	1.4992	1.3362	0.9483	0.5313	0.1227	0.3963
NDVI_RE	0.3980	0.3454	0.5301	0.6749	1.1266	1.1076	0.9099	0.6982	0.3925	0.0294	0.2767	0.3693
NG	0.4794	0.7469	1.3482	1.8606	1.7521	2.0573	2.1207	2.1661	1.9873	1.6886	1.2651	0.7620
NGRDI	0.1477	0.1978	0.0936	0.0540	0.0862	0.0686	0.0550	0.1968	0.3493	0.6263	1.0661	0.5301
NR	0.4333	0.4462	0.6932	0.9563	1.3756	1.3526	1.4585	1.2706	0.8277	0.4013	0.0097	0.4305
OSAVI	0.4955	0.4601	0.5942	0.8591	1.1005	1.1197	0.5396	0.8014	0.4751	0.2413	0.5046	0.4264
OSAVI_RE	0.4066	0.2701	0.2598	0.3412	0.4033	0.3244	0.4380	0.2988	0.2610	0.4016	0.7687	0.4339
SAVI	0.4968	0.4245	0.5225	0.7033	0.8352	0.7603	0.2543	0.6228	0.3492	0.1702	0.5312	0.4280
SAVI_RE	0.3801	0.1834	0.1455	0.1129	0.0579	0.2000	0.6257	0.5039	0.3837	0.4770	0.7804	0.4787
SR	0.5233	0.5209	0.7814	1.0806	1.5854	1.7366	1.7647	1.5149	1.0099	0.5460	0.1244	0.4116
TVI	0.5083	0.4992	0.7397	1.0322	1.3918	1.3662	1.4897	1.3226	0.9462	0.5318	0.1227	0.3925
TVI_RE	0.3953	0.3440	0.5311	0.6746	1.1199	1.1000	0.9048	0.6978	0.3924	0.0294	0.2767	0.3684

Appendix G: Separability results, for the entire dataset, between healthy vegetation and mild, moderate, and severe levels of iron chlorosis

Separability of Mild Chlorosis in soil-included VIs												
	05_05	**05_12**	**05_17**	**05_23**	**05_31**	**06_08**	**06_13**	**06_22**	**06_28**	**07_06**	**07_15**	**07_27**
DVI	0.3957	0.4288	0.3797	0.3453	0.3077	0.2105	0.4769	0.1430	0.3150	0.4042	0.5553	0.2834
DVI_RE	0.1885	0.1898	0.1957	0.1459	0.0004	0.0137	0.1573	0.2441	10.4740	0.0373	0.0371	0.0789
ENDVI	0.1995	0.4336	0.5585	0.5992	0.5707	0.5846	0.7052	0.3423	0.3915	0.6090	0.5397	0.4190
ENDVI_RE	0.0814	0.2037	0.3711	0.4780	0.2943	0.3672	0.1678	0.0163	0.1128	0.3008	0.3216	0.2623
EVI2	0.3463	0.4228	0.3987	0.4044	0.3625	0.3103	0.4924	0.1968	0.3279	0.4413	0.5625	0.3380
EVI2_RE	0.1740	0.2115	0.2052	0.2561	0.0503	0.0471	0.1467	0.1540	0.0559	0.0283	0.0458	0.1258
GDVI	0.6767	0.4789	0.4314	0.3987	0.3732	0.3211	0.5614	0.2429	0.4123	0.4427	0.6738	0.3023
GDVI_RE	0.4447	0.1909	0.2338	0.1750	0.0567	0.1206	0.0930	0.1669	0.0124	0.0556	0.0863	0.0397
GNDVI	0.4489	0.5186	0.6950	0.8814	0.7953	0.7689	1.0413	0.7601	0.9761	0.8638	0.9256	0.5273
GNDVI_RE	0.3322	0.3004	0.3997	0.1750	0.4921	0.5875	0.4081	0.3097	0.4875	0.2288	0.4644	0.1355
GOSAVI	0.5447	0.4875	0.5030	0.6581	0.6603	0.6683	0.7313	0.5610	0.6791	0.6873	0.7482	0.4023
MTCI	0.6663	0.7331	1.1841	0.9813	0.9112	0.6849	1.0748	1.1295	0.9817	1.1572	1.1484	0.6286
NDRE	0.7631	0.9293	1.1922	0.8531	0.9100	0.6933	1.0652	1.2022	1.0596	1.2472	1.2546	0.6666
NDVI	0.2745	0.3960	0.5833	0.6390	0.6260	0.6447	0.7385	0.4075	0.4617	0.6386	0.5919	0.4254
NDVI_RE	0.1597	0.1913	0.3962	0.5186	0.3191	0.4241	0.2119	0.0277	0.1789	0.3102	0.3520	0.1922
NG	0.6782	0.5692	0.7195	0.9252	0.8126	0.7769	1.0372	0.8028	1.0797	0.9180	1.0319	0.6259
NGRDI	0.0710	0.1699	0.3265	0.2947	0.0195	0.1206	0.0919	0.0377	0.0792	0.3059	0.1304	0.4240
NR	0.1984	0.3880	0.5596	0.6015	0.5728	0.5814	0.7053	0.3444	0.3902	0.6117	0.5432	0.4180
OSAVI	0.3069	0.4133	0.4347	0.4971	0.4561	0.4423	0.5504	0.2793	0.3654	0.5175	0.5796	0.3600
OSAVI_RE	0.1627	0.1915	0.2378	0.3574	0.1371	0.1565	0.1080	0.0713	0.0335	0.1380	0.0671	0.1379
SAVI	0.3573	0.4330	0.3948	0.4104	0.3713	0.2850	0.4924	0.2477	0.3366	0.4837	0.5666	0.3402
SAVI_RE	0.1784	0.2055	0.2037	0.2599	0.0629	0.0086	0.1510	0.1166	0.0010	0.0892	0.0474	0.1263
SR	0.2814	0.4086	0.5921	0.6153	0.6061	0.6887	0.8083	0.3927	0.4622	0.6214	0.5678	0.4375
TVI	0.2731	0.3949	0.5833	0.6394	0.6280	0.6443	0.7381	0.2489	0.4627	0.6409	0.5934	0.4228
TVI_RE	0.1586	0.1901	0.3958	0.5188	0.3205	0.4253	0.2125	0.1166	0.1797	0.3107	0.3542	0.1897

Separability of Mild Chlorosis in Soil-Removed VIs												
	05_05	**05_12**	**05_17**	**05_23**	**05_31**	**06_08**	**06_13**	**06_22**	**06_28**	**07_06**	**07_15**	**07_27**
DVI	0.6881	0.5268	0.2529	0.3958	0.3322	0.1593	0.4627	0.0409	0.2174	0.3313	0.6992	0.2483
DVI_RE	0.3908	0.2117	0.0476	0.2001	0.1492	0.1459	0.2102	0.3780	0.2882	0.1624	0.0723	0.0160
ENDVI	0.4388	0.4317	0.4662	0.7508	0.5812	0.5292	0.6070	0.2991	0.4153	0.6624	0.8054	0.3687
ENDVI_RE	0.2854	0.2825	0.2275	0.5567	0.2428	0.2894	0.1298	0.1096	0.0042	0.3244	0.4702	0.2203
EVI2	0.6325	0.5265	0.2729	0.5267	0.4050	0.2719	0.4695	0.1569	0.2611	0.3871	0.7181	0.3078
EVI2_RE	0.3712	0.2653	0.0272	0.2554	0.0681	0.0755	0.2063	0.3127	0.2206	0.0891	0.0869	0.0249
GDVI	0.9147	0.6398	0.3391	0.4451	0.4067	0.3145	0.5426	0.1524	0.3383	0.4313	0.8099	0.2729
GDVI_RE	0.5481	0.2389	0.0225	0.2345	0.0784	0.0054	0.1435	0.2890	0.1323	0.1683	0.1478	0.1493
GNDVI	0.8199	0.6950	0.7806	1.0640	0.7977	0.7641	0.9599	0.7893	1.0523	1.0021	1.3539	0.5196
GNDVI_RE	0.6222	0.4426	0.3183	0.7878	0.5701	0.6467	0.3411	0.2170	0.5043	0.2011	0.6671	0.0804
GOSAVI	0.8847	0.7002	0.4439	0.7946	0.6493	0.6121	0.5359	0.5626	0.7341	0.7191	0.9100	0.3883
MTCI	0.9818	0.9488	1.2485	0.9582	1.0300	0.8051	1.1067	1.2478	1.0249	1.2076	1.2478	0.6330
NDRE	0.9832	1.2143	1.3254	0.8307	0.9651	0.7988	1.1129	1.2474	1.1060	1.3173	1.2915	0.6890
NDVI	0.5295	0.4824	0.4794	0.7976	0.6185	0.5674	0.6420	0.3420	0.4798	0.6978	0.8786	0.3331
NDVI_RE	0.3538	0.2987	0.2302	0.5951	0.2874	0.3861	0.1629	0.0885	0.0965	0.2948	0.4979	0.1489
NG	0.9394	0.8105	0.8965	1.1630	0.8387	0.7728	0.9795	0.8223	1.1539	0.9823	1.4297	0.6278
NGRDI	0.0231	0.1995	0.0853	0.2783	0.0756	0.3623	0.1549	0.2096	0.2369	0.2933	0.1881	0.3827
NR	0.4382	0.4298	0.4675	0.7523	0.5811	0.5273	0.6030	0.3001	0.4159	0.6635	0.8072	0.3674
OSAVI	0.5861	0.5045	0.3157	0.6493	0.4743	0.4392	0.5138	0.2138	0.3293	0.5209	0.7474	0.3087
OSAVI_RE	0.3709	0.2884	0.0207	0.3895	0.0419	0.0544	0.1812	0.2446	0.1324	0.0085	0.1438	0.0694
SAVI	0.6342	0.5186	0.2685	0.5469	0.4214	0.2528	0.4687	0.2082	0.3118	0.4700	0.7235	0.3079
SAVI_RE	0.3688	0.2487	0.0303	0.2710	0.0627	0.0853	0.2044	0.2618	0.1631	0.0369	0.0917	0.0282
SR	0.5364	0.4943	0.4872	0.7713	0.6148	0.6186	0.6989	0.3304	0.4708	0.6839	0.8456	0.3460
TVI	0.5281	0.4806	0.4781	0.7999	0.6196	0.5659	0.6422	0.3427	0.4793	0.6995	0.8809	0.3302
TVI_RE	0.3516	0.2994	0.2311	0.5960	0.2883	0.3859	0.1628	0.0889	0.0968	0.2951	0.5000	0.1483

Separability of Moderate Chlorosis in Soil-Included VIs												
	05_05	**05_12**	**05_17**	**05_23**	**05_31**	**06_08**	**06_13**	**06_22**	**06_28**	**07_06**	**07_15**	**07_27**
DVI	0.0112	0.1551	0.4446	0.3827	0.2770	0.0014	0.2245	0.3541	0.2105	0.5367	0.8685	0.7029
DVI_RE	0.0493	0.0408	0.2478	0.0751	0.2481	0.8538	1.0643	1.3050	9.6558	1.0483	1.0555	0.6872
ENDVI	0.0334	0.2869	0.4585	0.6099	1.2070	1.0501	1.1870	0.9502	0.1913	0.2357	0.7352	0.7222
ENDVI_RE	0.0193	0.1972	0.3963	0.3042	0.7508	0.5045	0.4359	0.2423	0.3206	0.7141	1.1034	0.6689
EVI2	0.0273	0.1819	0.4461	0.4573	0.4660	0.2276	0.1197	0.0127	0.1544	0.4514	0.8768	0.7155
EVI2_RE	0.0412	0.1093	0.2731	0.0279	0.1185	0.6770	0.9867	1.0826	0.7923	1.0052	1.0647	0.6879
GDVI	0.0501	0.1921	0.5495	0.5168	0.4403	0.2301	0.0071	0.0963	0.0097	0.2782	0.6588	0.5018
GDVI_RE	0.1203	0.0032	0.3841	0.0020	0.1083	0.6020	0.7393	1.1144	0.4935	0.6537	0.7459	0.4279
GNDVI	0.0924	0.3275	0.1953	1.3557	1.6562	1.9357	2.1122	1.8994	1.2488	0.9723	0.2638	0.0225
GNDVI_RE	0.1729	0.2088	0.6851	0.0020	1.6222	1.5987	1.2514	0.9414	0.8211	0.5581	0.0488	0.0500
GOSAVI	0.0409	0.2786	0.5937	0.9679	1.1682	1.2339	0.6288	1.1001	0.6659	0.4883	0.5511	0.3488
MTCI	0.0791	0.5967	0.9653	1.6134	1.5979	1.9240	2.5199	2.0553	1.1129	0.7202	0.2758	0.1766
NDRE	0.2146	0.6935	1.2192	1.7016	1.5468	1.8676	2.4153	2.0129	1.1811	0.8938	0.5102	0.0479
NDVI	0.0742	0.2885	0.4854	0.6885	1.2535	1.1317	1.2574	1.0540	0.3450	0.0820	0.6012	0.6622
NDVI_RE	0.0568	0.1881	0.4487	0.3648	0.9033	0.6440	0.5684	0.3570	0.1412	0.5253	0.9057	0.5911
NG	0.0347	0.4096	0.8369	1.5841	1.7439	2.0994	2.2459	2.1091	1.4268	1.1964	0.4606	0.4859
NGRDI	0.0866	0.1017	0.1341	0.0934	0.1231	0.2801	0.3609	0.4101	0.9593	1.3053	1.6989	0.7038
NR	0.0332	0.2906	0.4593	0.6136	1.2005	1.0427	1.1796	0.9481	0.1914	0.2367	0.7337	0.7143
OSAVI	0.0569	0.2296	0.4552	0.5427	0.7640	0.5651	0.1166	0.4336	0.0317	0.3060	0.8948	0.7503
OSAVI_RE	0.0325	0.1378	0.3156	0.1441	0.1468	0.2202	0.8018	0.6006	0.5969	0.8826	1.0797	0.6693
SAVI	0.0236	0.1762	0.4459	0.4590	0.4932	0.1894	0.1432	0.2862	0.0727	0.3712	0.8764	0.7173
SAVI_RE	0.0403	0.0983	0.2666	0.0411	0.1026	0.7370	1.0081	0.8073	0.7021	0.9469	1.0675	0.6846
SR	0.0771	0.3114	0.5146	0.6669	1.2937	1.2347	1.4073	1.1026	0.3487	0.0805	0.6138	0.7063
TVI	0.0733	0.2852	0.4876	0.6898	1.2481	1.1247	1.2497	0.2870	0.3447	0.0823	0.6010	0.6555
TVI_RE	0.0564	0.1853	0.4467	0.3660	0.9021	0.6426	0.5687	0.8060	0.1418	0.5264	0.9024	0.5852

Separability of Moderate Chlorosis in Soil-Removed VIs												
	05_05	**05_12**	**05_17**	**05_23**	**05_31**	**06_08**	**06_13**	**06_22**	**06_28**	**07_06**	**07_15**	**07_27**
DVI	0.0900	0.1176	0.1122	0.1993	0.2115	0.0774	0.2099	0.3985	0.2348	0.5504	0.7704	0.7089
DVI_RE	0.1924	0.1998	0.1606	0.4513	0.6340	0.9801	1.1788	1.5139	0.9189	1.1062	0.9444	0.6693
ENDVI	0.2670	0.1513	0.3104	0.5776	1.4033	1.1504	1.2228	1.0293	0.1455	0.1774	0.5548	0.5775
ENDVI_RE	0.2602	0.0869	0.1069	0.0868	0.9225	0.6085	0.4765	0.2955	0.3859	0.6857	0.9980	0.5497
EVI2	0.1753	0.0241	0.1350	0.3077	0.4678	0.3311	0.1054	0.0013	0.1589	0.4254	0.7717	0.6717
EVI2_RE	0.2223	0.0649	0.1180	0.3162	0.3963	0.7348	1.0876	1.2541	0.8544	1.0531	0.9400	0.6392
GDVI	0.0509	0.1707	0.2656	0.3655	0.4310	0.3170	0.0462	0.1172	0.0201	0.2444	0.5144	0.4830
GDVI_RE	0.2638	0.4109	0.0613	0.3387	0.3845	0.6284	0.7926	1.3055	0.5332	0.7010	0.6129	0.4090
GNDVI	0.3315	0.1953	1.0689	1.6540	1.8291	2.1103	2.1147	1.9841	1.3113	1.1156	0.5242	0.0757
GNDVI_RE	0.4075	0.0819	0.7153	0.8951	1.8598	1.9281	1.3453	1.0866	0.9818	0.7157	0.2016	0.1548
GOSAVI	0.2474	0.0813	0.4852	1.0632	1.4161	1.4546	0.0466	1.2302	0.7383	0.5714	0.3571	0.3104
MTCI	0.0308	0.4083	1.1825	1.9771	1.7848	2.0417	2.6288	2.1236	1.0799	0.8046	0.4355	0.1259
NDRE	0.0603	0.6747	1.4211	2.0977	1.6764	1.9495	2.5901	2.0440	1.1630	0.9859	0.5926	0.0103
NDVI	0.3073	0.1643	0.3870	0.6827	1.4553	1.2339	1.2933	1.1218	0.2639	0.0266	0.4090	0.5508
NDVI_RE	0.3041	0.0700	0.1892	0.1906	1.0858	0.7611	0.6045	0.4197	0.1819	0.4967	0.7988	0.4778
NG	0.1945	0.2488	1.3001	1.8891	1.8868	2.2731	2.2562	2.1736	1.4921	1.3494	0.7216	0.6573
NGRDI	0.1316	0.0506	0.2888	0.4596	0.2940	0.2179	0.3702	0.5203	1.0276	1.3295	1.5676	0.6869
NR	0.2654	0.1502	0.3109	0.5806	1.3922	1.1476	1.2166	1.0230	0.1458	0.1777	0.5529	0.5714
OSAVI	0.2522	0.0853	0.1806	0.4465	0.8228	0.7100	0.1558	0.4732	0.0274	0.2733	0.7686	0.6349
OSAVI_RE	0.2670	0.0022	0.0429	0.1354	0.0470	0.1832	0.8689	0.6825	0.6491	0.9142	0.9632	0.5767
SAVI	0.1628	0.0462	0.1327	0.3179	0.4938	0.2876	0.1280	0.3129	0.0919	0.3231	0.7763	0.6544
SAVI_RE	0.2184	0.0877	0.1286	0.2958	0.3728	0.7854	1.1018	0.9091	0.7216	0.9788	0.9439	0.6321
SR	0.3213	0.1725	0.3744	0.6544	1.5373	1.3999	1.4732	1.2054	0.2706	0.0265	0.4153	0.5818
TVI	0.3059	0.1632	0.3886	0.6824	1.4399	1.2258	1.2861	1.1165	0.2637	0.0266	0.4095	0.5440
TVI_RE	0.3009	0.0698	0.1899	0.1919	1.0862	0.7579	0.6043	0.4208	0.1825	0.4974	0.8007	0.4740

Separability of Severe Chlorosis in Soil-Included VIs												
	05_05	**05_12**	**05_17**	**05_23**	**05_31**	**06_08**	**06_13**	**06_22**	**06_28**	**07_06**	**07_15**	**07_27**
DVI	0.9913	1.2004	1.1867	1.1593	1.0382	0.9175	0.4981	0.3282	0.1144	0.0725	0.6951	0.1246
DVI_RE	0.6923	0.9840	0.9143	0.6374	0.3649	0.0157	0.3265	0.6781	8.9406	0.6073	0.8727	0.1798
ENDVI	0.9115	1.3362	1.6507	1.7089	1.8324	2.1694	2.1188	2.0335	1.4311	0.9081	0.0830	0.1891
ENDVI_RE	0.7861	1.0243	1.3215	1.3711	1.3918	1.5024	1.3875	1.1023	0.7740	0.3006	0.2564	0.1354
EVI2	0.9648	1.2241	1.2193	1.3731	1.2374	1.2853	0.6091	0.7590	0.4305	0.3046	0.6657	0.1324
EVI2_RE	0.6850	1.0200	0.9605	0.8609	0.6186	0.3218	0.2444	0.3807	0.3457	0.4196	0.8599	0.1706
GDVI	1.0885	1.2049	1.2848	1.3099	1.3012	1.2874	0.7572	0.5421	0.3231	0.3212	0.5176	0.0060
GDVI_RE	0.6555	0.9418	1.0456	0.6952	0.7883	0.3149	0.0625	0.6313	0.3658	0.3472	0.6290	0.1169
GNDVI	0.7844	1.4698	1.5586	2.5549	3.2507	3.8094	3.4058	3.6068	2.5232	2.1376	1.1972	0.3481
GNDVI_RE	0.5306	1.2517	1.5744	0.6952	2.9148	2.9694	2.6739	1.9945	1.4753	1.1306	0.7168	0.2198
GOSAVI	0.9056	1.3761	1.5205	2.0711	2.5297	2.9832	1.4707	2.1600	1.4991	1.3821	0.3123	0.1255
MTCI	1.0869	1.5341	2.1196	2.6780	2.6876	3.5365	3.4035	3.3641	2.5625	2.0735	0.9445	0.2312
NDRE	0.9109	1.6303	1.9293	2.4436	2.5311	3.2603	3.1792	3.2008	2.7113	2.2304	1.0758	0.2373
NDVI	0.9107	1.3115	1.7227	1.7280	1.8604	2.1544	2.1326	2.1282	1.5463	1.0480	0.2213	0.1507
NDVI_RE	0.6783	1.0514	1.4092	1.3992	1.5868	1.6567	1.5418	1.2251	0.8914	0.4158	0.0885	0.1043
NG	0.7302	1.5692	2.0133	3.2083	3.5034	4.9873	3.9025	4.1919	2.7204	2.4361	1.4451	0.7097
NGRDI	0.3896	0.7263	1.0467	0.8857	0.3012	0.3912	0.3331	0.3454	0.2184	0.2178	1.0020	0.1575
NR	0.9170	1.2563	1.6479	1.6564	1.7481	2.0783	2.0683	1.9897	1.4216	0.9080	0.0832	0.1884
OSAVI	0.9582	1.2648	1.3878	1.5358	1.4881	1.7214	0.8705	1.3106	0.8527	0.6372	0.6131	0.1662
OSAVI_RE	0.6773	1.0459	1.0576	1.0941	0.9688	0.8223	0.0404	0.1376	0.1100	0.1033	0.8156	0.1578
SAVI	0.9645	1.2323	1.2431	1.3677	1.2569	1.2087	0.5885	1.0944	0.6861	0.5154	0.6588	0.1371
SAVI_RE	0.6867	1.0188	0.9554	0.8686	0.6452	0.2512	0.2647	0.0742	0.0879	0.2152	0.8603	0.1681
SR	0.8914	1.1389	1.4195	1.7321	2.2808	2.7407	2.6289	2.3044	1.5784	1.0604	0.2175	0.1555
TVI	0.9142	1.3377	1.6920	1.6817	1.8159	2.0977	2.1039	1.0858	1.5345	1.0452	0.2218	0.1500
TVI_RE	0.6792	1.0645	1.4005	1.3719	1.5522	1.6133	1.5218	0.0746	0.8887	0.4170	0.0886	0.1037

Separability of Moderate Chlorosis in Soil-Removed VIs												
	05_05	**05_12**	**05_17**	**05_23**	**05_31**	**06_08**	**06_13**	**06_22**	**06_28**	**07_06**	**07_15**	**07_27**
DVI	1.0523	0.9183	1.0755	1.0003	0.9981	0.9556	0.3665	0.1114	0.0091	0.0666	0.8082	0.3068
DVI_RE	0.6316	0.5727	0.5394	0.2368	0.1250	0.2406	0.5734	1.1763	0.8733	0.7020	1.0240	0.3439
ENDVI	0.8055	0.9758	1.5425	1.7902	1.9667	2.2672	2.0869	2.2494	1.5696	1.0206	0.3357	0.2421
ENDVI_RE	0.5827	0.7835	1.0973	1.2440	1.5280	1.6781	1.3813	1.2266	0.8331	0.3153	0.1224	0.2542
EVI2	0.9854	0.9687	1.1544	1.2709	1.3868	1.3999	0.4844	0.6411	0.3840	0.3614	0.7798	0.2387
EVI2_RE	0.6311	0.6926	0.6054	0.5246	0.4467	0.2056	0.4884	0.7422	0.5237	0.4641	1.0006	0.3085
GDVI	1.1095	1.1770	1.3286	1.2153	1.4162	1.3784	0.6548	0.3706	0.2449	0.3588	0.5944	0.1651
GDVI_RE	0.6584	0.6064	0.8382	0.3867	0.6646	0.2073	0.2407	1.0244	0.5994	0.4421	0.7019	0.2802
GNDVI	1.0425	1.5586	2.2853	2.7335	2.9725	3.8929	3.6275	3.7813	2.8198	2.4001	1.6077	0.4170
GNDVI_RE	0.7138	1.1306	1.7377	2.2721	2.7462	3.1711	2.8306	2.1934	1.6642	1.2720	1.0448	0.1363
GOSAVI	1.0818	1.4660	1.6877	2.1787	2.7165	3.1230	0.6519	2.2912	1.6862	1.6103	0.3075	0.0640
MTCI	1.4382	1.8705	2.2868	2.5322	2.9096	3.7825	3.5564	3.6157	2.7852	2.2416	1.1493	0.2628
NDRE	1.3543	2.2108	2.0611	2.3207	2.7210	3.3793	3.2078	3.3132	2.8482	2.3942	1.2111	0.3228
NDVI	0.9277	1.0656	1.6196	1.8899	1.9880	2.2639	2.1044	2.3363	1.6875	1.1752	0.4993	0.1991
NDVI_RE	0.6547	0.8323	1.1912	1.3633	1.7061	1.8168	1.5378	1.3596	0.9886	0.4797	0.0661	0.2193
NG	0.9771	1.8227	2.4279	3.0368	3.2859	4.6633	4.1291	4.2020	3.0446	2.7612	1.8697	0.8318
NGRDI	0.2866	0.4007	0.5929	0.5400	0.0429	0.3474	0.2491	0.1849	0.2004	0.2187	0.9373	0.3238
NR	0.8079	0.9799	1.5245	1.7600	1.9120	2.1873	2.0437	2.2235	1.5576	1.0189	0.3355	0.2409
OSAVI	0.9564	1.0058	1.2732	1.5523	1.7357	1.9023	0.7732	1.2885	0.9386	0.7300	0.6755	0.2127
OSAVI_RE	0.6684	0.7813	0.7467	0.8822	0.9169	0.8227	0.2332	0.0284	0.0385	0.1164	0.9447	0.2471
SAVI	0.9957	0.9509	1.1405	1.3097	1.4337	1.3111	0.4682	1.0561	0.7116	0.5918	0.7713	0.2226
SAVI_RE	0.6373	0.6740	0.5928	0.5607	0.4842	0.1182	0.5017	0.3255	0.1724	0.2535	0.9963	0.2972
SR	0.9191	1.0101	1.5963	1.8595	2.4958	3.0614	2.6721	2.5290	1.7448	1.2159	0.4921	0.2059
TVI	0.9272	1.0689	1.6061	1.8478	1.9530	2.2130	2.0796	2.2868	1.6730	1.1735	0.5009	0.1978
TVI_RE	0.6569	0.8392	1.1853	1.3434	1.6717	1.7952	1.5209	1.3551	0.9864	0.4791	0.0662	0.2195

Appendix H: An area of iron chlorosis and green vegetation mapped over the season

Note: This is a display of regular multispectral imagery. The top black box represents an area of healthy vegetation and the bottom box represents an area of severe iron chlorosis.

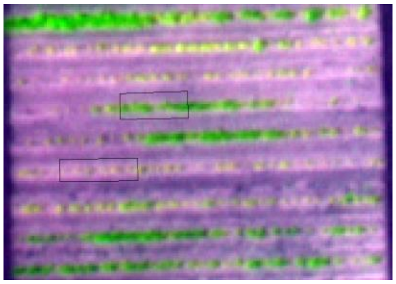
May 5, 2017

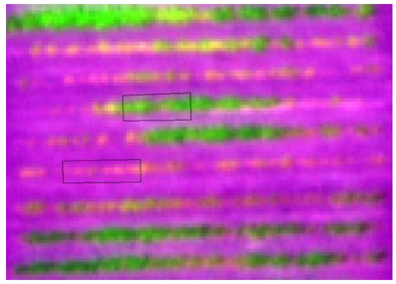
May 12, 2017

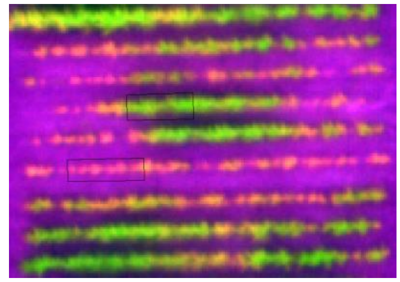
May 17, 2017

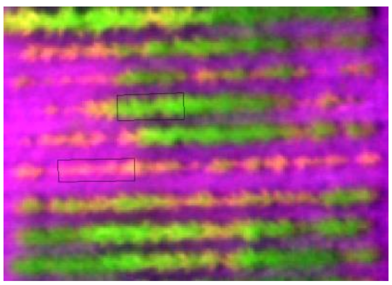
May 23, 2017

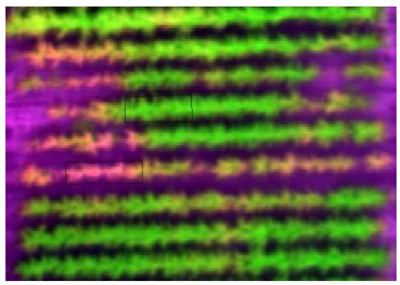
May 31, 2017

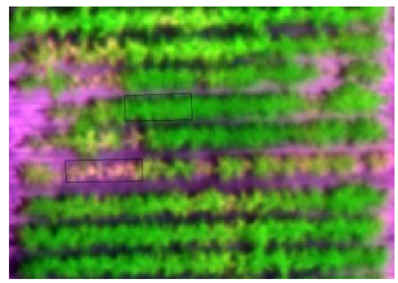
June 8, 2017

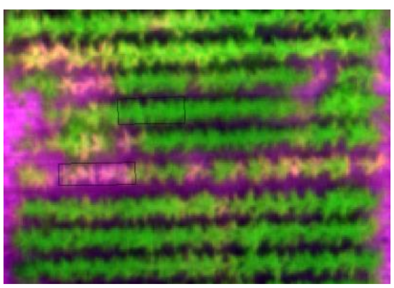
June 13, 2017

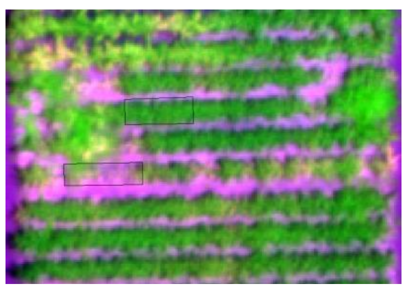
June 22, 2017

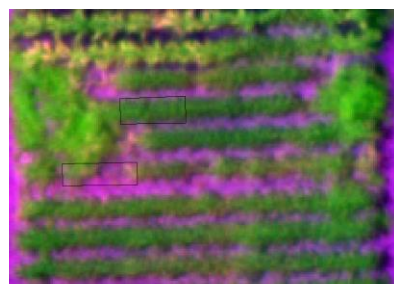
June 28, 2017

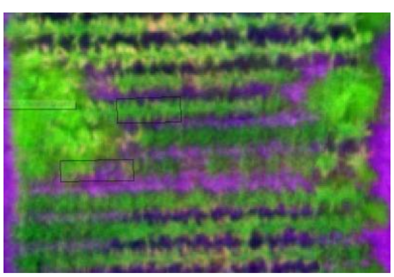
July 6, 2017

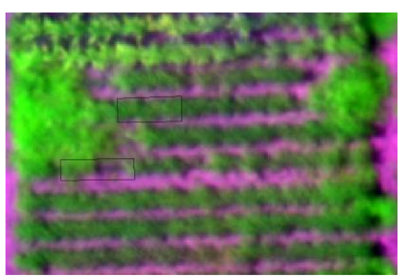
July 15, 2017

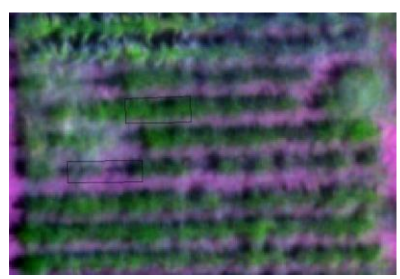
July 27, 2017

Note: This is a display of soil-removed multispectral imagery. The top black box represents an area of healthy vegetation and the bottom box represents an area of severe iron chlorosis.

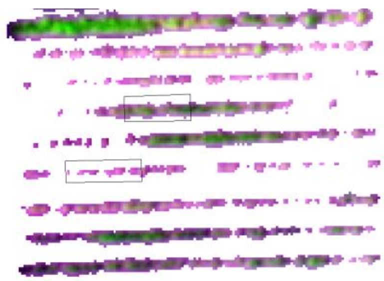

May 5, 2017

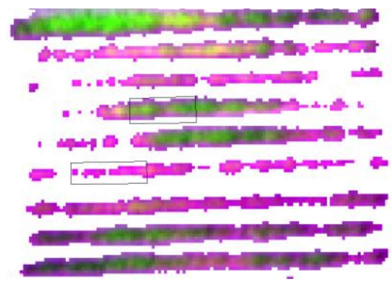

May 12, 2017

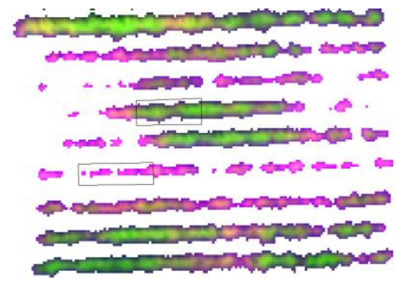

May 17, 2017

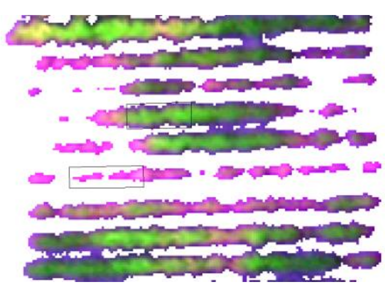

May 23, 2017

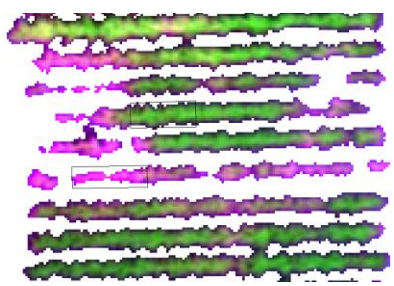

May 31, 2017

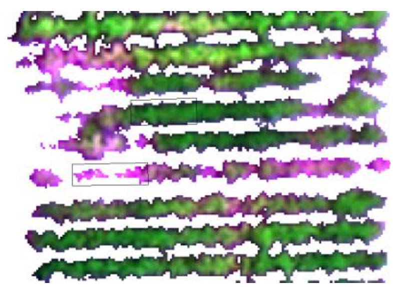

June 8, 2017

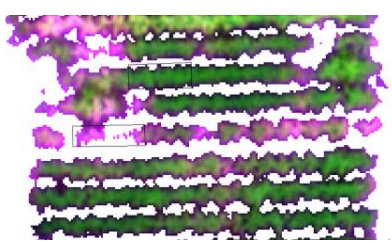

June 13, 2017

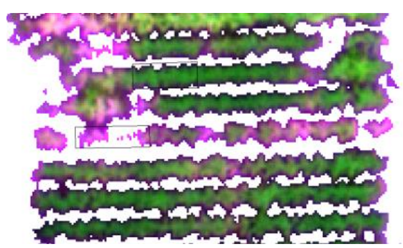

June 22, 2017

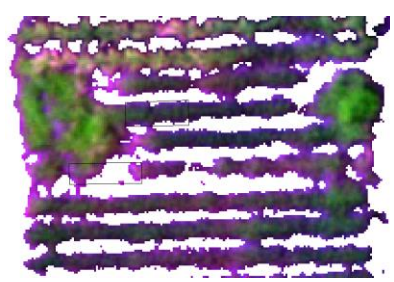

June 28, 2017

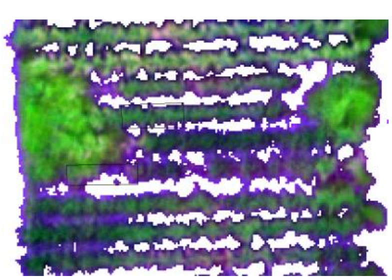

July 6, 2017

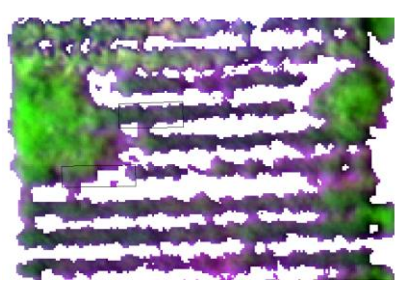

July 15, 2017

July 27, 2017

Appendix I: Yield measurements and grain estimates in comparison with values from the top three VIs, the MTCI, NG, and NDRE.

ID	Measured Weight (in grams)	Weight Estimation (in grams)	MTCI	NG	NDRE
107ag	180	189.4737	0.1900	0.1662	0.3157
107ay	no data	no data	0.1632	0.1721	0.2762
108bg	317	634.0000	0.1900	0.1593	0.2915
109ay	no data	no data	0.2097	0.1786	0.2675
109bg	no data	no data	0.2560	0.1583	0.2944
110ay	18	360.0000	0.1663	0.2034	0.2233
201ag	334	351.5790	0.1947	0.1712	0.2592
201ay	83	332.0000	0.1709	0.1772	0.2390
302ag	199	398.0000	0.2441	0.1524	0.2676
302ay	199	995.0000	0.2025	0.1537	0.2647
304ag	261	522.0000	0.2719	0.1836	0.2680
304ay	63	1260.0000	0.1989	0.1626	0.2533
305ag	no data	no data	0.2110	0.1431	0.3053
304by	98	392.0000	0.2060	0.1836	0.2245
306bg	599	360.5263	0.2343	0.1646	0.2700
307ay	15	300.0000	0.1721	0.1907	0.2409
309bg	256	393.8462	0.2234	0.1523	0.2550
309by	152	506.6667	0.1553	0.1801	0.2306
403bg	431	783.6364	0.2637	0.1611	0.2440
403by	384	426.6667	0.1956	0.1749	0.2207
405ag	266	280.0000	0.2248	0.1785	0.2373
405ay	195	205.2632	0.1900	0.1881	0.0240
406bg	175	437.5000	0.2045	0.1655	0.2730
406by	no data	no data	0.1485	0.1760	0.2424
407bg	362	381.0526	0.1744	0.1769	0.2355
407by	276	394.2857	0.2707	0.1843	0.2231
408bg	281	562.0000	0.1821	0.1626	0.2651
408ay	75	750.0000	0.1811	0.1827	0.2376